Topology of magnetism and superconductivity in non-collinear spin textures

Dissertation
zur Erlangung des Doktorgrades
an der Fakultät für Mathematik, Informatik und Naturwissenschaften
Fachbereich Physik
der Universität Hamburg

vorgelegt von

Reiner Brüning

Hamburg
31. July, 2024

Gutachter/innen der Dissertation:	Prof. Dr. Roland Wiesendanger PD Dr. Kirsten von Bergmann
Zusammensetzung der Prüfungskommission:	Prof. Dr. Daniela Pfannkuche Prof. Dr. Roland Wiesendanger PD Dr. Kirsten von Bergmann Prof. Dr. Henning Moritz Prof. Dr. Wolfgang Hansen
Vorsitzende/r der Prüfungskommission:	Prof. Dr. Daniela Pfannkuche
Datum der Disputation:	10.10.2024
Vorsitzender des Fach-Promotionsausschusses PHYSIK:	Prof. Dr. Markus Drescher
Leiter des Fachbereichs PHYSIK:	Prof. Dr. Wolfgang J. Parak
Dekan der Fakultät MIN:	Prof. Dr.-Ing. Norbert Ritter

Abstract

The concept of topology in condensed matter physics has received a lot of attention in recent decades, due to its possible utilization in several applications. In the field of unconventional computing, non-collinear spin textures such as skyrmions and merons possess a topological protection making them to promising candidates for commercial spintronic devices. An approach in the realization of quantum computing is to utilize topologically robust edge modes at the boundary of topological non-trivial bulk systems, e. g. in topological superconductors. To obtain topological superconductivity, so-called two-dimensional magnet-superconductor hybrids are promising candidate systems for the realization of topology-based quantum technologies and superconducting spintronics. Magnet-superconductor systems hosting spin textures with collinear spin alignment are already well established, however, the experimental investigation of non-collinear spin textures in the vicinity of an s-wave superconductor is still pending.

In this thesis, the first observation of nanoscale skyrmions on a square symmetric lattice in one monolayer of Mn on W(001) is presented. By using low-temperature spin-polarized scanning tunneling microscopy, an interesting mixed state is found, consisting of a spin spiral texture background with a magnetic period of $P = 2.2$ nm and several magnetic skyrmions on the square symmetric crystal lattice surface of W(001).

Further, the realization of the first two-dimensional non-collinear magnet-superconductor-hybrid system in the monolayer of Fe on Ta(110) is presented. Fe/Ta(110) exhibits a spin spiral texture with a magnetic period of approximately $P = 6$ nm. As for the system of Mn/W(001), the spin spiral state of Fe/Ta(110) is transitioning to a skyrmionic phase at high magnetic fields of a few Teslas. In contrast to Mn/W(001), the skyrmions are elongated due to the two-fold lattice symmetry and they occur in a ferromagnetic background.

In Fe/Ta(110), depending on the morphology of the monolayer, the system offers beside the spin spiral texture also an in-plane ferromagnetic state with non-collinear domain wall configurations. One domain wall orientation is characterized by a meron-antimeron texture along the propagation direction of the spin spiral.

To study the interaction between the spin spiral texture and superconductivity, the samples with a spin spiral as the magnetic ground state were measured at a temperature of $T = 1.3$ K. The spectroscopic analysis shows in-gap states modulations in the bulk area of the Fe monolayer, while at the boundaries of the Fe, chiral edge states are identified at straight edges along the $[001]$-direction. Furthermore, tight-binding calculations validate nodal-point superconductivity for the system and

identify the different signal intensities along edges with the same crystallographic orientation as an effect of the local spin orientation at the edge onto the chiral edge state dispersion.

Zusammenfassung

Das Prinzip von Topologie in der Physik der kondensierten Materie hat in den letzten Jahrzehnten aufgrund seiner möglichen Anwendungen viel Aufmerksamkeit erregt. Im Bereich der magnetischen Systeme sind nichtkollineare Spinstrukturen wie Skyrmionen und Meronen, vielversprechende Kandidaten für zukünftige Spintronik-Bauelemente. Ein Ansatz für die Realisierung von Quantencomputern ist die Nutzung des topologischen Schutzes von Randmoden an der Grenze topologisch nichttrivialer Volumensysteme, z. B. in topologischen Supraleitern. Um topologische Supraleitung zu erreichen, sind so genannte zweidimensionale Magnet-Supraleiter-Hybride vielversprechende Kandidaten für die Realisierung von Topologie-basierten Quantentechnologien und der supraleitenden Spintronik. Magnet-Supraleiter-Hybride mit einer kollinearen Spin-Ausrichtung konnten bereits in anderen Arbeiten untersucht werden, die experimentelle Untersuchung von nichtkollinearen Spin-Texturen auf einem s-Wellen-Supraleiter steht jedoch noch aus.

In dieser Arbeit wird die erste Beobachtung von Skyrmionen in der Größenordnung einiger Nanometer auf einem quadratsymmetrischen Gitter im Probensystem einer Monolage Mn auf W(001) dargelegt. Mit Hilfe der spinpolarisierten Rastertunnelmikroskopie im Sub-Kelvin Bereich zeigt die Mn-Monolage einen interessanten Mischzustand, bestehend aus einer Spinspiralphase mit einer magnetischen Periode von $P = 2,2$ nm und mehreren magnetischen Skyrmionen.

Des Weiteren wird die Realisierung des ersten zweidimensionalen nicht-kollinearen Magnet-Supraleiter-Hybridsystems in der Monolage von Fe auf Ta(110) vorgestellt. Fe/Ta(110) weist eine Spinspirale mit einer magnetischen Periode von etwa $P = 6$ nm auf. Wie beim System Mn/W(001) geht der Spinspiralzustand von Fe/Ta(110) bei hohen Magnetfeldern von einigen Tesla in eine skyrmionische Phase über. Im Gegensatz zu Mn/W(001) sind die Skyrmionen elongiert aufgrund der vorliegenden (110)-Gitterymmetrie und existieren in einem ferromagnetischen Hintergrund.

Abhängig von der Morphologie der Monolage bietet das System neben der Spinspirale auch einen in-plane ferromagnetischen Zustand mit nicht-kollinearen Domänenwandkonfigurationen. Eine Domänenwandorientierung ist durch eine Meron-Antimeron-Konfiguration entlang der Ausbreitungsrichtung der Spinspirale charakterisiert.

Um die Wechselwirkung der Spinspirale mit der Supraleitung zu untersuchen, wurden die Proben mit einer Spinspirale als magnetischem Grundzustand bei einer Temperatur von $T = 1,3$ K gemessen. Die spektroskopische Analyse zeigt Modulationen der In-Gap-Zustände im inneren Bereich der Fe-Monolage, während an den Grenzen der Fe-Monolage chirale Randzustände an geraden Kanten ent-

lang der $[001]$-Richtung identifiziert werden. Darüber hinaus zeigen Tight-Binding Berechnungen, dass die unterschiedlichen Signalintensitäten entlang der Kanten in $[001]$-Richtung auf eine Abhängigkeit der Dispersion der chiralen Randzustände von der Spinorientierung der Spinspirale an der Kante zurückzuführen sind.

Contents

Abbreviations

Abbreviation	**Meaning**
AFM	antiferromagnetic
BdG	Bogoliubov-de-Gennes
BCS	Bardeen-Cooper-Schrieffer
DFT	density functional theory
DMI	Dzyaloshinskii-Moriya-interaction
DOS	density of states
EMR	electronic magnetoresistance
FM	ferromagnetic
HTF	high temperature flash
LDOS	local density of states
LEED	low-energy electron diffraction
MSH	magnet-superconductor hybrid
NCMR	non-collinear magnetoresistance
SOC	spin-orbit coupling
SP-STM	spin-polarized scanning tunneling microscopy
STM	scanning tunneling microscopy
STS	scanning tunneling spectroscopy
TAMR	tunneling anisotropic magnetoresistance
TMR	tunneling magnetoresistance
UHV	ultra-high vacuum

Introduction

The demand for larger data storage systems and faster data processing units was essential in the last decades and will be present also in the following decades, whereby the gap between data storage supply and demand is increasing drastically [1, 2]. Since conventional computing systems are reaching more and more the limit of manageable heat dissipation due to the miniaturization of semiconductor devices, a fundamental change in the method used for computational processes is initiated and will further develop in the future. One idea to overcome this limit and improve the energy efficiency is quantum computing [3, 4], which is a promising approach due to the utilization of quantum physics, a field which offers numerous paths to new concepts of data processing in modern computers.

The realization of quantum computing requires the identification of a suitable bit, in quantum computing called a quantum bit (qubit), that fulfills two criteria: (1) the fully decoupling of the qubit from its environment to avoid the loss of quantum properties (decoherence) and (2) the ability to perform computational operations with these qubits. A property that realizes decoupling from its environment is topological protection, which gives rise to the field of topologically protected quantum computation. A search for potential qubit candidates equipped with these properties has initiated different approaches. One approach are boundary modes, which are topologically protected by the bulk properties of a system. For example, in the case of a topologically non-trivial superconductor, topological edge modes appear [5–8]. Promising candidates to initiate topological phases of superconductivity are magnetic skyrmions or merons from the field of spintronics [9–12], quasiparticles with a knot-like spin configuration that leads to magnetic topological protection, which in combination with superconductivity can lead to Majorana bound states with potential application in quantum computing.

In this thesis, sample systems which offer the opportunity to study such states are discussed, and the discovery of a sample system providing a spin configuration which combines both topological protections is presented. In Chapter 1, an introduction to the related theoretical background is given, where the general definition of topology and its application to condensed matter physics is discussed. Further, the phenomenon of magnetism is examined, where the relevant interactions and a selection of possible magnetic ground states are included. As the last of three fundamental fields of physics essential for this thesis, superconductivity is introduced, covering both conventional and unconventional superconductivity.

In Chapter 2, the experimental setup is described, and the measurement methods with the relevant contrast mechanisms are presented.

Chapter 3 focuses on the experimental realization of nanoscale skyrmions for the first time stabilized on a square symmetric lattice in one monolayer of Mn on W(001). After the investigations of non-collinear spin textures on a metal in a normal conducting state, in Chapter 4, the experimental realization of non-collinear spin textures on an elemental s-wave superconductor in one monolayer of Fe on Ta(110) is examined.

Chapter 5 is dedicated to the identification of the magnetic properties of the magnetically complex sample system of Fe/Ta(110). Depending on the morphology of the monolayer of Fe, a spin spiral state or an in-plane ferromagnet with meron-antimeron domain walls, is identified.

In Chapter 6, Fe/Ta(110) in the superconducting state is discussed. The identification of local density of states (LDOS) modulations at energies inside the superconducting gap following the period of the apparent spin spiral texture gives rise to spin-polarized in-gap states in the bulk area of the Fe monolayer. Subsequently, the properties at the boundaries of the Fe islands in the superconducting state are investigated. Supported by tight-binding calculations, chiral edge states are identified in the experiment as an increased tunneling conductance intensity at straight edges along $[001]$-direction. Further, a chiral edge state dispersion dependency on the spin spiral termination angle at the edges is discovered. The thesis concludes with an outlook of potential applications and future investigations.

1 Interplay of Topology, Magnetism and Superconductivity

The first chapter provides the theoretical foundation for the physical phenomena explored in this thesis. A brief introduction to the mathematical concept of topology and its application in condensed matter physics is presented first. Afterwards, the phenomenon of superconductivity is discussed, addressing both the conventional and unconventional cases. The physics of single magnetic atoms on surfaces and the interactions within a magnetic layer are then examined. The chapter concludes with a selection of possible spin configurations in magnetic layers and their topological charge.

1.1 Topology in condensed matter

In recent decades, there has been great interest in the study of unique phases of matter using topological classification schemes. One groundbreaking example is the quantum Hall effect, observed in a two-dimensional electron gas under a high magnetic field applied perpendicular to the surface. In such a system, the bulk behaves as an insulator, while conductive channels with quantized conductance appear at the boundary of the sample [13–16]. Another famous example is the discovery of topological insulators [17–20], systems that are insulating in their bulk but conductive on their surfaces. In these materials, the topological properties can be observed without applying an external magnetic field.

More recent examples of topology in condensed matter are Weyl semimetals [21], topologically non-trivial magnetic textures like skyrmions [22], and topological superconductors [5, 6, 23–25]. The latter two cases will be addressed in this thesis.

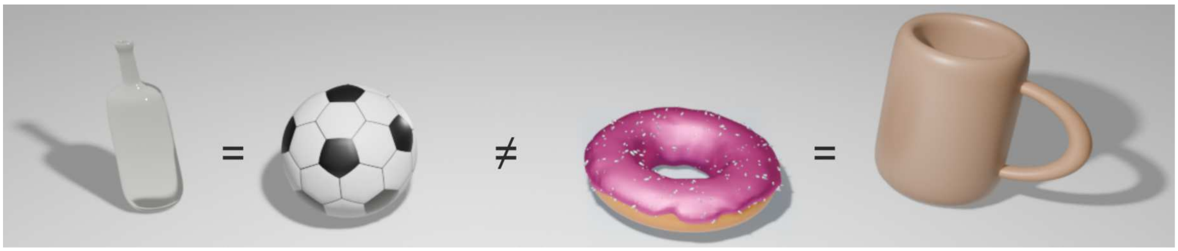

Figure 1.1: Topology in daily objects. A sketch of different objects classified in topologically trivial and non-trivial geometric objects.[1]

---

[1] geometric objects created in Blender

Since topology stems from a general mathematical classification of geometric objects, it can also be used to classify daily objects, as shown in Fig. 1.1, where an unequal sign separates objects with different topology, in this case the objects on the right side contain a hole in contrast to the bottle and football on the left side of Fig. 1.1. The topological classification means that objects with different topology cannot be continuously deformed into each other without closing or opening holes. Consequently, the classification of daily objects can simply be done by counting the holes of an object, leading to the definition of topologically equal objects when they provide the same number of holes.

This concept can be extended to the field of solid-state physics. The Hamiltonian serves as a starting point for topological classification. After setting up a sufficient Hamiltonian for a system, the identification of the present symmetries can be done. Typically in solid state physics the time-reversal symmetry ($\mathcal{T}$), particle-hole symmetry ($\mathcal{P}$) and chiral symmetry ($\mathcal{C}$) are used. Depending on which symmetries are present, a symmetry class for the system can be identified, which also defines the appropriate topological invariant, an integer that characterizes the topological phase of the system. In solid-state physics, the Chern number [26] is commonly used for the topological classification of energy bands, whereas in the topological description of daily objects the number of holes was sufficient.

$$C = \frac{1}{2\pi} \int_{BZ} B \, dk_x \, dk_y. \tag{1.1}$$

In solid state physics, the Chern number is defined as the integral of the Berry curvature over the entire Brillouin zone (see Eq. 1.1). A non-zero Chern number implies a topologically non-trivial state, while a Chern number of zero leads to a topologically trivial state. Consequently, when two systems with different topological invariants, such as Chern numbers, are connected, the energy gap at the interface must close, resulting in protected boundary modes at energies inside the bulk gap of the system. This concept, known as bulk-boundary correspondence [27], means that the properties of the bulk Hamiltonians give rise to boundary states at the interfaces. These boundary states exist as long as the topological invariants of the system remain constant.

This principle can be applied to either one-, two-, or three-dimensional systems, resulting in boundary states arising as states in zero dimensions, at the ends of a one-dimensional wire [28], in one dimension, at the boundary of a two-dimensional island [29], and enclosing the entire bulk area of a system, as in the case of a three-dimensional topological insulator [17], respectively. The topological protection of the states can be utilized for applications in the growing field of quantum computing and can potentially improve the data processing.

1.2 Conventional Superconductivity

This section is dedicated to the phenomenon of superconductivity [30], a fascinating state of condensed matter in which the resistance of a given sample drops to zero below a critical temperature T_C. In 1911, the first experimental observation of this state was measured in mercury by H. K. Onnes $et\ al.$. He was awarded with the Nobel prize of physics in 1913 [31]. An additional property of materials in the superconducting state is that the superconductor expels magnetic flux, as long as the applied magnetic field does not exceed a certain field strength. This effect is known as Meissner-Ochsenfeld effect and was discovered in 1933 [32]. These results led to a phenomenological approach, but for decades, there was a lack of a suitable model describing these observations microscopically.

As a starting point for the microscopic description of superconductivity, F. and H. London introduced the first phenomenological model to describe the superconducting state in 1935. Their two semi-classical equations describe the electrodynamics of a superconductor as the following:

$$\frac{\partial \mathbf{j}}{\partial t} = \frac{e^2 n}{m}\mathbf{E} \tag{1.2}$$

$$\nabla \times \mathbf{j} = -\frac{e^2 n}{mc}\mathbf{B}. \tag{1.3}$$

Here, $\mathbf{j}$ represents the current density, $\mathbf{E}$ and $\mathbf{B}$ are the electric and magnetic fields, c stands for the speed of light, and n is the charge carrier density. Considering the absence of electric fields, the first equation suggests that currents in this ideal conductor remain stationary. Implementing Ampère's circuital law and the second London equation leads to:

$$\nabla^2 \mathbf{B} = \frac{\mathbf{B}}{\lambda_L^2}, \tag{1.4}$$

where λ_L is the London penetration depth. The solution to this equation offers an exponentially decay of the magnetic field within a superconductor on the scale of λ_L, and implies important properties of a superconducting material.

Another crucial parameter for the characterization of superconductors is the coherence length ξ_0, which can be semi-classically interpreted as the extension of a Cooper pair. Within the Ginzburg-Landau theory, ξ_0 characterizes the variation length scale of the superconducting order parameter of the Cooper pair condensate by energy costs lower than the pair-breaking energy. The energy to break a Cooper pair leads to a gap of quasiparticle excitations with a width of 2Δ around the Fermi level. The superconducting gap is a characteristic feature in the spectroscopic measurements which will be used in this thesis to obtain more information about the superconducting properties of the samples. Both λ_{L} and ξ_0 typically comprise several tens of nanometers. The ratio of both length scales, known as the Ginzburg-Landau parameter κ, is defined as:

$$\kappa = \frac{\lambda_{\mathrm{L}}}{\xi_0} \tag{1.5}$$

and remains approximately temperature-independent unlike λ_{L} and ξ_0. For Ta this parameter is $\kappa_{\mathrm{Ta}} \approx 0.35$ [33]. In 1957, A. A. Abrikosov classified superconductors into type-I and type-II based on κ. In the regime $\kappa \ll 1$, magnetic fields decay rapidly within the superconductor, while the condensate wavefunction varies slowly, leading to a wide region where the condensate expels magnetic fields with positive surface energy. Conversely, for $\kappa \gg 1$, the surface energy can become negative, favoring the formation of interfaces between normal and superconducting regions.

The critical Ginzburg-Landau parameter, $\kappa = \frac{1}{\sqrt{2}}$, separates type-I superconductors ($\kappa < \frac{1}{\sqrt{2}}$) with a critical field B_c, beyond which superconductivity breaks down, and type-II superconductors with two critical fields, B_{c1} and B_{c2}. In the range of $B_{\mathrm{c1}} < B < B_{\mathrm{c2}}$, vortex tubes appear within the superconductor, allowing magnetic flux penetration through the superconductor. Inside these vortex cores, the order parameter vanishes, and a supercurrent, a dissipationless flow of current in a superconductor, circulates around the center of the vortex. Above B_{c2}, superconductivity is quenched similarly to type-I superconductors. The previously mentioned value of $\kappa_{Ta} \approx 0.35$ indicates that Ta, the material investigated in the superconducting phase in this thesis, is a type-I superconductor. Despite the Ginzburg-Landau theory improved the understanding of the phenomenon of superconductivity, a more detailed description of superconductivity is introduced in the following.

The microscopic explanation of the effect by J. Bardeen, L. N. Cooper, and J. R. Schrieffer (BCS theory), and the contributions by A. A. Abrikosov, V. L. Ginzburg, and A. J. Leggett were again awarded with two Nobel Prizes in 1972 and 2003, respectively. The main idea behind this model relies on the formation of bound pairs of electrons, the so-called Cooper pairs, which are assumed to be bosons instead of fermions in the case of unpaired electrons. This bosonic nature allows to describe the new state as a collective quantum mechanical ground state with perfect conductance. This formation leads to a gap of 2Δ in the electronic density of states (DOS), representing the minimal energy required to break a Cooper pair. The BCS Hamiltonian comprises two primary components:

$$H_{BCS} = \int \epsilon_{\mathbf{k}} c^{\dagger}_{\mathbf{k},\sigma} c_{\mathbf{k},\sigma} \, d\mathbf{k} + \int V_{\mathbf{k}\mathbf{k}'} c^{\dagger}_{\mathbf{k}\uparrow} c^{\dagger}_{-\mathbf{k}\downarrow} c_{-\mathbf{k}'\downarrow} c_{\mathbf{k}'\uparrow} \, d\mathbf{k} \, d\mathbf{k}'. \tag{1.6}$$

Here, $c^{\dagger}_{\mathbf{k},\sigma}$ and $c_{\mathbf{k},\sigma}$ denote the creation and annihilation operators for a fermion with momentum $\mathbf{k}$ and spin σ. $\epsilon_{\mathbf{k}}$ represents the band energy, while $V_{\mathbf{kk}'}$ is the pairing potential. In conventional superconductors, the attractive interaction originates from electron-phonon interactions, thereby the second term can be interpreted as electrons creating pairs via a virtual phonon.

The mean-field approximation simplifies this Hamiltonian by eliminating four-term interactions and defining $\Delta_{\mathbf{k}}$:

$$\Delta_{\mathbf{k}} = -\int V_{\mathbf{kk}'} \langle c_{-\mathbf{k}'\downarrow} c_{\mathbf{k}\uparrow} \rangle \, d\mathbf{k}'. \tag{1.7}$$

This results in the following mean-field Hamiltonian:

$$H_{BCS} = \int \epsilon_{\mathbf{k}} c^{\dagger}_{\mathbf{k},\sigma} c_{\mathbf{k},\sigma} \, d\mathbf{k} + \int (\Delta_{\mathbf{k}} c^{\dagger}_{\mathbf{k}\uparrow} c^{\dagger}_{-\mathbf{k}\downarrow} + \Delta^{*}_{\mathbf{k}} c_{-\mathbf{k}\downarrow} c_{\mathbf{k}\uparrow}) \, d\mathbf{k} + \tilde{E}, \tag{1.8}$$

where $\tilde{E}$ represents an energy offset. A Bogoliubov-Valatin transformation diagonalizes this Hamiltonian, revealing Bogoliubov-de-Gennes (BdG) quasiparticles $\gamma_{\mathbf{k}\uparrow}$ and $\gamma_{-\mathbf{k}\downarrow}$ obeying fermionic anticommutation relations. The Hamiltonian, in terms of these BdG quasiparticles, becomes:

$$H_{BCS} = \int E_{\mathbf{k}} \gamma^{\dagger}_{\mathbf{k},\sigma} \gamma_{\mathbf{k},\sigma} \, d\mathbf{k} + \tilde{E} \tag{1.9}$$

with the energy dispersion for the quasiparticles given by:

$$E_{\mathbf{k}} = \sqrt{\epsilon^2_{\mathbf{k}} + |\Delta_{\mathbf{k}}|^2}. \tag{1.10}$$

The expectation values $|u_{\mathbf{k}}|^2$ and $|v_{\mathbf{k}}|^2$ are connected as follows:

$$|v_{\mathbf{k}}|^2 = 1 - |u_{\mathbf{k}}|^2 = \frac{1}{2}\left(1 - \frac{\epsilon_{\mathbf{k}}}{E_{\mathbf{k}}}\right). \tag{1.11}$$

In a simplified view, mean field theory effectively reduces the two-body problem to a one-body problem by introducing the BdG quasiparticles, which improves the calculations of such a system to be much less time-consuming.

While nearly-free electrons exhibit a dispersion $\epsilon_{\mathbf{k}} = \frac{\hbar^2 |\mathbf{k}|^2}{2m^*} + E_F$, the presence of a finite gap 2Δ in the spectrum around E_{F} leads coherence peaks at $\pm\Delta$, effectively avoiding states between $\pm\Delta$. These peaks can be attributed to quasiparticle excitations at energies where the Cooper pairs break. The DOS, which is correlated to the measured signal in the experiments, can be obtained by considering $N(E_{\mathbf{k}})\mathrm{d}E = N(\epsilon_{\mathbf{k}})\mathrm{d}\epsilon$. Since in a realistic system, the quasiparticles have a finite lifetime, a broadening parameter Γ needs to be implemented resulting in the well-known Dynes-function:

$$\frac{N(E)}{N_0} = \text{Re}\left[\frac{E - i\Gamma}{\sqrt{(E - i\Gamma)^2 - \Delta^2}}\right]. \tag{1.12}$$

This function plays a crucial role in characterizing the DOS and can be measured in tunneling experiments, such as scanning tunneling spectroscopy (STS), a measurement method used in this thesis for the investigation of the superconducting properties of the samples (see details in Sec. 2.4). The effect of the broadening parameter Γ is presented in Fig. 1.2, where the increase of Γ leads to a filling of the states at energies between $\pm\Delta$ and to a suppression of the coherence peaks.

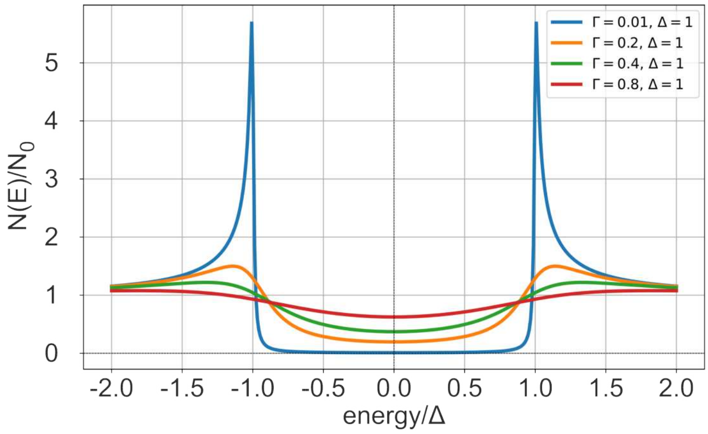

Figure 1.2: Density of states of a superconductor. The DOS is plotted using the Dynes function for $T = 0$ K in dependency on the energy for different values of the broadening parameter Γ.

Nodal-point Superconductivity

A special type of conventional superconductivity is a nodal-point superconductor [34–39], where the energy gap of 2Δ closes at certain points in k-space. This phenomenon is not exclusively observable in a few superconductors or magnet-superconductor hybrid (MSH)-systems; it also appears in materials with Dirac cones (e.g., graphene [40, 41]) leading to nodes without chirality, and Weyl semimetals [21, 42–44], exhibiting nodes with chirality. In Fig. 1.3, a visualization of energy bands of a gapped superconductor with a clear energy separation of both bands is shown in (a), while (b) depicts a gapless superconductor with four nodal points where the conduction and valence bands touch each other at zero energy. Since the previously discussed Chern number is ill-defined in the case of touching energy bands, it is not possible to calculate a meaningful Chern number for such a superconductor

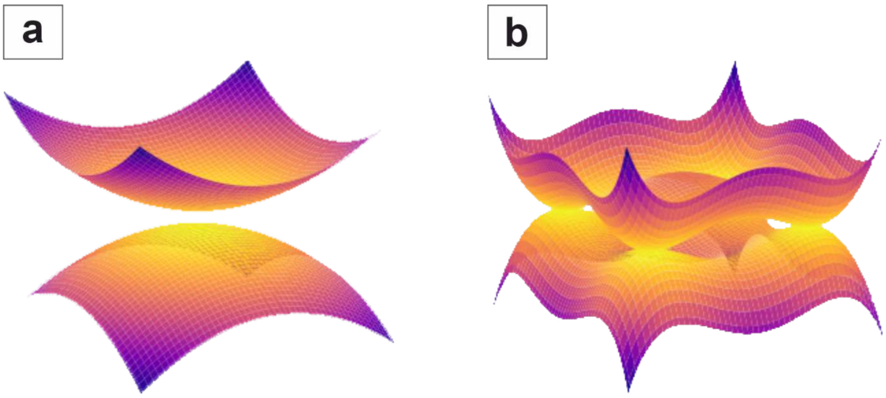

Figure 1.3: Energy bands of a gapped and gapless superconductor. A sketch of possible gapped (a) and gapless (b) energy band configuration for two different superconductors. The gapped superconductor shows an energy gap around the Fermi level. The gapless superconductor has four nodal points where the valence and conduction bands touch each other.

to identify the topology of the system. Therefore, another topological invariant, the so-called winding number [45], is used to explicitly choose a closed path around the nodal points to determine whether they contain a finite topological charge.

Unconventional Superconductivity

The previous introduction to superconductivity focused solely on conventional superconductors, where electron pairing is initiated by phonons and characterized by s-wave symmetry, the pairing mechanism with the highest symmetry. In these systems, electrons with opposite spins form Cooper pairs in a spin-singlet state with a total spin $S = 0$. Consequently, the orbital momentum of the Cooper pair is $L = 0$. The elemental superconductor Ta is well described by the introduced model. However, when other materials are deposited onto a Ta sample, as examined in this thesis, the situation becomes more complex to describe the superconductivity in the proximitized material. When a normal metal is in the vicinity of a superconductor, the proximity effect [46] leads to the adoption of superconducting properties by the normal metal. In more detail, the formed Cooper pairs in the superconductor are able to penetrate into the normal metal and induce superconducting correlations over a certain distance. In this intermediate scenario of a fractionally proximitized normal metal, the pairing mechanism differs from that of the bulk superconductor.

Therefore, it is important to note that other, more exotic pairing mechanisms may exist. For example, not just phonons but also spin-fluctuations can contribute to the pairing mechanism leading to drastically higher transition temperatures, e.g.

cuprates and Fe-based pnictides [47]. Moreover, some materials exhibit Cooper pairs in a spin-triplet state with total spin $S = 1$ or with angular momentum $L \neq 0$. States where the angular momentum is non-zero can be classified in p-wave, d-wave, etc., in analogy to atomic orbitals with higher angular momenta. The discovery of more complex mechanisms for creating Cooper pairs, led to critical temperatures which were higher than the temperatures observed for conventional superconductors. However, in the race to find a superconductor with a transition temperature as close as possible to room temperature, hydrogen-based superconductors under high pressure, which can be described by the BCS theory, emerge as the most promising candidates, as recent developments indicate [48, 49].

In this thesis, the focus will be on the topologically non-trivial phases of superconductivity. In addition to the described ways of complex pairing mechanisms of the Cooper pairs, heterostructures consisting of conventional superconductors combined with magnetic materials can exhibit unconventional properties of the superconducting state as well, e.g. a two-dimensional magnetic layer, offering a non-collinear spin texture, in vicinity to an s-wave superconductor [50]. Since the experimental realization and investigation of such an MSH-system will be one of the main topics in this thesis, the next section will discuss established concepts of magnetic materials on metals, both in the normal and superconducting state.

1.3 Magnetic atoms on surfaces

To discuss the phenomena of two-dimensional MSH-systems, an introduction to the physics emerging from the adsorption of a single magnetic atom and an entire monolayer of a magnetic material on a metal, initially in the normal state and subsequently in the superconducting state, is presented.

Kondo Physics

Magnetic atoms interacting with a metallic crystal can lead to complex, strongly correlated states, for which a theoretical description is challenging. Jun Kondo was able in 1964 to develop a scattering model that describes such a system and solved unclear observations from the 1930s [51, 52] where metals doped with magnetic impurities exhibited an increasing resistance at low-temperatures. In this model the local spins of the impurity are interacting with the delocalized conduction electrons of the crystal via an exchange interaction J_K. This interaction leads to a resonant scattering channel and in a regime of strong coupling it leads to an effective screening of the magnetic moment, i.e. the impurity spin and the conduction electrons form a many-body singlet state (Kondo cloud) with $S = 0$ [53]. The system undergoes

a crossover from a high-temperature regime with free spins to a low-temperature regime with screened spin, the threshold between these regimes defines the Kondo temperature T_K.
Spin-flip processes of the system mainly occur for nearly degenerate ground states at low energy. Scanning tunneling spectroscopy is one possible tool to observe these excitations as a resonance around zero energy. The first experimental proof of this zero-bias anomaly was observed on Ce [54] and Co atoms [55–58] on noble-metal (111) surfaces. The tunneling path can either go through the Kondo resonance or directly into the substrate. Considering an interference of both paths the appearance of the Kondo feature in the measured $\frac{\mathrm{d}I}{\mathrm{d}V}$-signal can vary from a dip to a peak in conductance around zero. This is phenomenologically described by a Frota lineshape [59, 60]:

$$\rho_{\text{Frota}}(\omega) = A \cdot \mathrm{Re}\left[e^{i\phi} \sqrt{\frac{i\Gamma_F}{\omega - \omega_0 + i\Gamma_F}} \right] \tag{1.13}$$

with the Frota parameter Γ_F, the intensity of the resonance A, the energy of the resonance ω_0 and the phase factor ϕ.

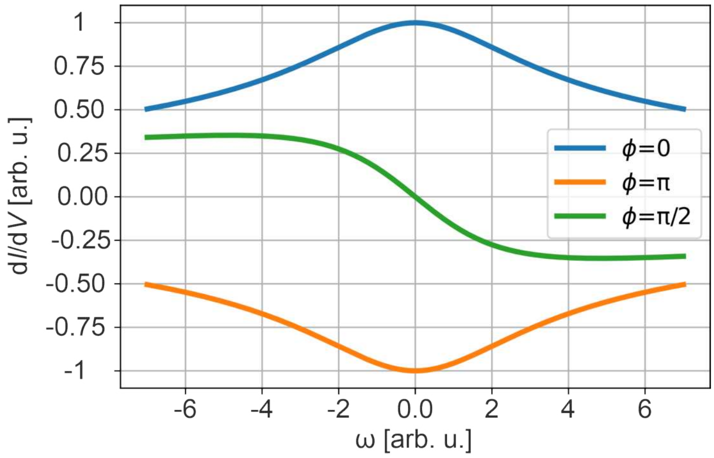

Figure 1.4: Frota resonance. Visualization of resonances using the Frota function in Eq. 1.13 for different values of the phase factor ϕ.

Yu-Shiba-Rusinov States

One can now raise the question how the physics of a magnetic impurity on a metal is changed by the superconducting state where the conduction electrons are bound to Cooper pairs?

In the 1960s, this problem was investigated by L. Yu, H. Shiba and A. Rusinov independently [61, 62]. They concluded that, under consideration of the BdG Hamiltonian incorporating scattering by magnetic and non-magnetic potentials and superconducting pairing, magnetic impurities break the Cooper pairs, resulting in the so-called Yu-Shiba-Rusinov in-gap states. Due to particle-hole symmetry, these in-gap states appear in pairs at energies $\pm E_{\text{YSR}}$ around zero energy. The Yu-Shiba-Rusinov states are exponentially localized around the magnetic impurity, with a decay length determined by the superconductor's coherence length ξ_0.

1.3.1 Interaction between magnetic atoms

The increase in the number of magnetic atoms leads to an increased number of required interactions to be considered to determine the magnetization of the atoms. There is a zoo of different possible spin textures which can be stabilized by the interplay of several magnetic atoms, as it is presented in section 1.3.2. Spin textures can be categorized into collinear, non-collinear and non-coplanar spin configurations. The collinear case includes the ferromagnetic (FM) alignment of adjacent spins as well as the antiferromagnetic (AFM) alignment. For a FM state, the angle between adjacent spins is $\theta = 0°$. If the angle is $\theta = 180°$ an AFM state is realized. An angle which is between a FM and AFM alignment results in a spin spiral, a $360°$ rotation of the spins along the propagation direction of the spin texture with either a fixed angle (homogeneous spin spiral) or a varying angle between neighboring spins (inhomogeneous spin spiral). The ratio of the following exchange interactions plays an important role in determining the magnetic ground state of a system.

First of all, the Heisenberg exchange is the strongest exchange interaction and is a quantum mechanical phenomenon that results from the overlap of electron wavefunctions. The sum over all atom pairs with spins $\mathbf{S}_i$ and $\mathbf{S}_j$ can be expressed as [63]:

$$E_{\text{ex}} = \sum_{i,j} -J_{ij}\mathbf{S}_i \cdot \mathbf{S}_j, \tag{1.14}$$

with a summation of all possible pairs of spins. For different crystal symmetries or materials, the distance between the neighboring spins varies. In Fig. 1.5 the nearest neighbors in both crystal symmetries discussed in this thesis, namely the bcc(001) and bcc(110) surface, are presented. The exchange constant J_{ij} becomes very small for distances larger than a few atomic constants. For most magnetic systems, only the nearest neighbors play a role and determine which ground state is stabilized. In the case of a FM system the exchange constant is positive ($J_1 > 0$) and in the AFM case the exchange constant changes to a negative value ($J_1 < 0$). If J_1 and J_2 have a different sign in the case of a bcc(110) surface, the spin

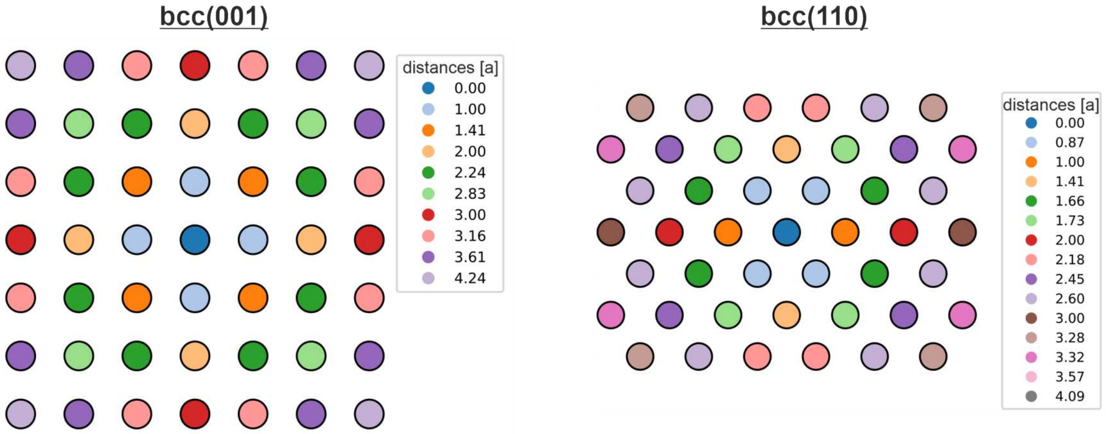

Figure 1.5: Nearest neighbor distances of two body center cubic planes. Visualization of the nearest neighbor distances for the bcc(001) and bcc(110) surface. The listed distances are in units of the lattice constant a.

system becomes frustrated and may accommodate non-collinear magnetic states. Fig. 1.6 (a) shows a simulation of the Heisenberg model in one dimension with a positive exchange constant between the nearest neighbors resulting in a FM state.

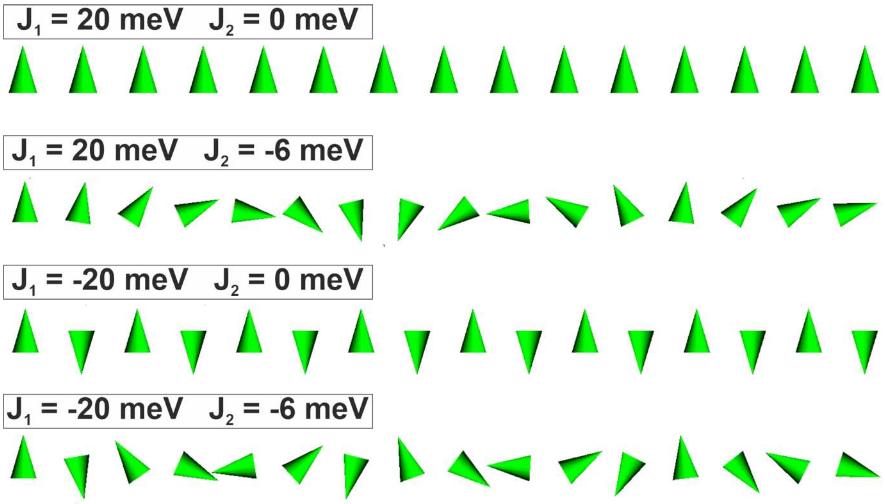

Figure 1.6: The one-dimensional solution of the Heisenberg model. Simulation of the Heisenberg model with exchange energies between nearest neighbors J_1 and next nearest neighbors J_2 simulated with the Monte Crystal Software [64] which was created by J. Hagemeister. (a) FM case with $J_1 = 20\ \mathrm{meV}, J_2 = 0\ \mathrm{meV}$, (b) spin spiral case with $J_1 = 20\ \mathrm{meV}, J_2 = -6\ \mathrm{meV}$, (c) AFM case with $J_1 = -20\ \mathrm{meV}, J_2 = 0\ \mathrm{meV}$ and in (d) spin spiral with $J_1 = -20\ \mathrm{meV}, J_2 = -6\ \mathrm{meV}$. All energies are in units of energy per bond.

In Fig. 1.6 (b), the next nearest neighbor term, which prefers an AFM alignment, creates a spin spiral. If J_1 is negative and J_2 is not considered, it leads to the AFM case as it is visible in Fig. 1.6 (c). If both values are negative, again a spin spiral arises with the same angle between adjacent spins with respect to the quantization axis but this time an AFM spin spiral is apparent (see Fig. 1.6 (d)).

Another important energy to describe the magnetic interactions is the spin-orbit coupling (SOC), which is responsible for additional magnetic energies. The SOC describes the interaction between the spin of the electron and the movement around the nucleus. This movement leads, in the rest frame of the electron, to a moving nucleus which produces a magnetic field the electron spin can couple to. This magnetic field depends on $\mathbf{L}$, the spin $\mathbf{S}$ of the electron, the radius of the orbit r and the potential of the nucleus V. The resulting magnetic term can be expressed by:

$$H_{\mathrm{SOC}} = \frac{1}{r}\frac{\delta V(r)}{\delta r}\mathbf{L}\cdot\mathbf{S}. \tag{1.15}$$

The potential V varies between different crystallographic directions so that the spins prefer different orientations. Consequently, there are easy (hard) axes where the H_{SOC} is minimized (maximized). At surfaces, a term like [65]:

$$E_{\mathrm{ani}} = \sum_i K \sin^2 \phi_i \tag{1.16}$$

describes the first order uniaxial anisotropy energy and is usually sufficient for isotropic, ultrathin films on single crystals. It includes the anisotropy constant K and the angle ϕ_i between the spin S_i on site i and the anisotropy axis. For $K > 0$ $(K < 0)$ the axis is an easy (hard) axis and the spins will prefer to orient collinearly (perpendicularly) to it in order to reduce the anisotropy energy. Another consequence of the SOC is the Dzyaloshinskii-Moriya-Interaction (DMI) [66, 67]:

$$E_{\mathrm{DMI}} = \sum_{i,j} \mathbf{D}_{i,j}\cdot(\mathbf{S}_i \times \mathbf{S}_j), \tag{1.17}$$

where $\mathbf{D}$ is the Dzyaloshinskii vector, which is constrained by the symmetry of the system. In contrast to the Heisenberg exchange, DMI contains the cross product of two spins $\mathbf{S}_i, \mathbf{S}_j$ which means that a canting of $\frac{\pi}{2}$ between two magnetic moments is energetically favorable. If the system is centrosymmetric, the DMI vanishes, since the Hamiltonian is invariant under all symmetry operations of the system. Both effects related to SOC are strongly correlated with the atomic number Z, since $H_{\mathrm{SOC}} \propto \frac{\delta V(r)}{\delta r} \propto Z$.

External magnetic field

The effect of an external magnetic field can be described with the Zeeman energy. This additional term represents the potential of an external magnetic field $\vec{B}$ acting on the magnetization of the sample $\mathbf{M}_{\mathrm{S}}$:

$$E_{\mathrm{Zee}} = \frac{g_{\mathrm{S}}\mu_{\mathrm{B}}}{\hbar}\mathbf{M}_{\mathrm{S}} \cdot \mathbf{B}, \tag{1.18}$$

where $g_{\mathrm{S}} \approx 2$ is the Landé factor, $\hbar$ is Planck's quantum of action and μ_{B} is the Bohr magneton. The dependence on $\mathbf{B}$ means that with high external magnetic field the magnetic moments of the sample will prefer a parallel alignment to $\mathbf{B}$.

Hamiltonian for a magnet-superconductor-hybrid-system

For the description of a MSH-system additional terms related to superconductivity need to be added to the magnetic-related terms introduced in the last section. A minimal Hamiltonian of such a MSH-system can be expressed as [68]:

$$\begin{aligned} H_{\mathbf{k}} = \sum_{\mathbf{k}\in\mathrm{BZ}} \{ &\psi_{\mathbf{k}} \left[\epsilon_{\mathbf{k}}\sigma_0\tau_z + \boldsymbol{\alpha}_{\mathbf{k}} \cdot \boldsymbol{\sigma}\tau_z + \Delta\sigma_0\tau_x\right] \psi_{\mathbf{k}} \\ &+\psi_{\mathbf{k}} \left[\mathbf{S}_{\mathbf{Q}} \cdot \boldsymbol{\sigma}\tau_0\right] \psi_{\mathbf{k}+\mathbf{Q}} + \text{ h.c. } \}, \end{aligned} \tag{1.19}$$

where

$$\epsilon_{\mathbf{k}} = 2t_0\left(\cos\left(k_1\right) + \cos\left(k_2\right)\right) + 2t_1\cos\left(k_1 - k_2\right) + 2t_2\cos\left(k_1 + k_2\right) - \mu \tag{1.20}$$

$$\begin{aligned} \alpha_{\mathbf{k}} = 2 \Big(&\alpha_0\sqrt{\tfrac{1}{3}}\left(\sin\left(k_2\right) - \sin\left(k_1\right)\right) - \alpha_1\sin\left(k_1 - k_2\right) \\ &\alpha_0\sqrt{\tfrac{2}{3}}\left(\sin\left(k_2\right) + \sin\left(k_1\right)\right) + \alpha_2\sin\left(k_1 + k_2\right), 0\Big), \end{aligned} \tag{1.21}$$

$$\mathbf{S}_{\mathbf{Q}} = \frac{1}{\sqrt{M_1M_2}}\sum_{\mathbf{r}}\mathbf{S}(\mathbf{r})e^{-\mathrm{i}\mathbf{Q}\cdot\mathbf{r}}. \tag{1.22}$$

Here, M_1 and M_2 refer to the size of the magnetic unit cell along the chosen lattice vectors $\mathbf{a}_1$ and $\mathbf{a}_2$, respectively, and $\mathbf{S}(\mathbf{r})$ at site $\mathbf{r} = (x, y)$ defines the spin texture under investigation.

In real systems, all the introduced magnetic interactions compete with each other and provide the magnetic ground state of a system. The next section will give an overview of the spin textures in magnetic layers relevant to this thesis.

1.3.2 Spin configurations and topology of magnetic textures on surfaces

For the prediction of the type of magnetic ground state that can be found in a sample system, a consideration of several interactions, as discussed in the previous section, is necessary. The magnitude of these interactions varies with different material combinations, which results in several potential magnetic ground states.

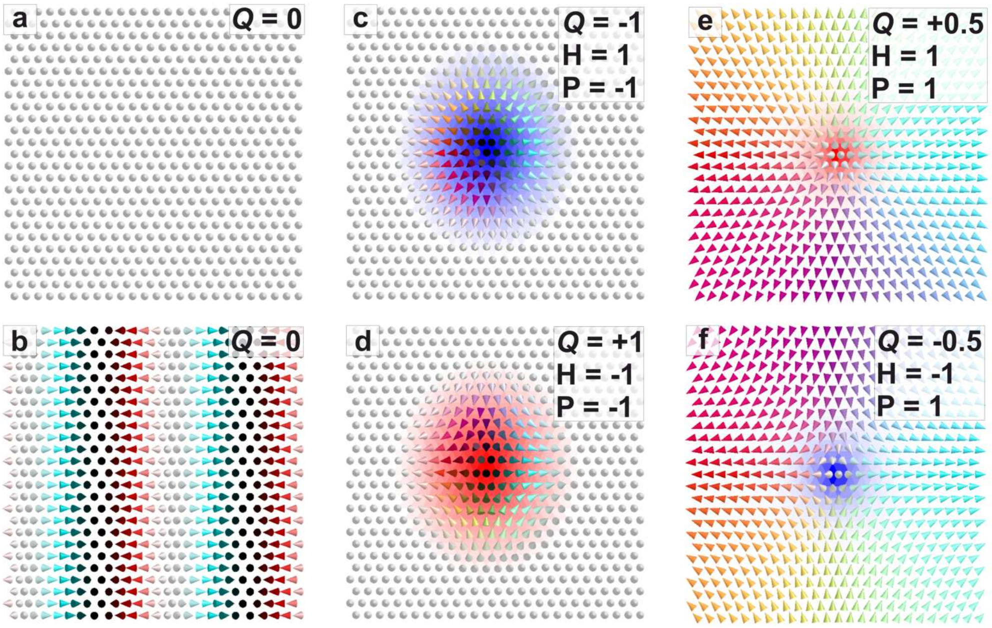

Figure 1.7: Set of possible spin configurations on sample surfaces. In all presented panels, the topological charge density is mapped [69], where blue color means negative topological charge and red means positive topological charge. For a topological charge of zero, the background remains white. (a) A FM state with spins pointing upwards in an out-of-plane direction. (b) A cycloidal spin spiral with a period of a few lattice sites and a trivial topological charge. (c) A magnetic Néel-like skyrmion with negative polarity (spin pointing downwards) and positive helicity (clockwise rotation). The topological charge is $Q = -1$. (d) A Néel-like antiskyrmion with the same polarity as in c) but changed helicity and different topological charge ($Q = +1$). A meron (e) and an antimeron (f) with the same polarity and different helicity, with $Q = +0.5$ or $Q = -0.5$, respectively, are presented.

In Fig. 1.7, a few examples of possible spin configurations inside a magnetic layer are shown, along with the corresponding calculated topological charge density [70, 71], where the local topological charge can be calculated with two triangular sublattices as presented in the following [69]:

$$q_1 = \Re\left[\frac{2}{i}\log\left(\frac{1+\mathbf{r}_1\cdot\mathbf{r}_2+\mathbf{r}_2\cdot\mathbf{r}_3+\mathbf{r}_3\cdot\mathbf{r}_1+i\mathbf{r}_1\cdot(\mathbf{r}_2\times\mathbf{r}_3)}{\sqrt{2\left(1+\mathbf{r}_1\cdot\mathbf{r}_2\right)\left(1+\mathbf{r}_2\cdot\mathbf{r}_3\right)\left(1+\mathbf{r}_3\cdot\mathbf{r}_1\right)}}\right)\right]\div(4\pi) \tag{1.23}$$

$$q_2 = \Re\left[\frac{2}{i}\log\left(\frac{1+\mathbf{r}_2\cdot\mathbf{r}_4+\mathbf{r}_4\cdot\mathbf{r}_3+\mathbf{r}_3\cdot\mathbf{r}_2+i\mathbf{r}_2\cdot(\mathbf{r}_4\times\mathbf{r}_3)}{\sqrt{2\left(1+\mathbf{r}_2\cdot\mathbf{r}_4\right)\left(1+\mathbf{r}_4\cdot\mathbf{r}_3\right)\left(1+\mathbf{r}_3\cdot\mathbf{r}_2\right)}}\right)\right]\div(4\pi). \tag{1.24}$$

The different $\mathbf{r}$ vectors refer to the spin components of the four atoms involved in the calculation of the topological charge of two triangles and the prefactor is for the normalization of the topological charge.

In Fig. 1.7(a), a collinear ferromagnet with an out-of-plane spin orientation is shown. The topological charge density is zero for the entire area as expected for a FM alignment. In Fig. 1.7(b), a spin spiral with Néel-like rotation is sketched in a two-dimensional layer. The topological charge remains zero for such a spin configuration because a rotation confined to a plane is not sufficient; a contribution from the third dimension is necessary to span a solid angle which leads to a non-zero topological charge. In Figs. 1.7(c) and (d), a skyrmion and an antiskyrmion, respectively, are shown. A skyrmion [22, 72–77] is a quasiparticle that is topologically protected, as shown by the calculated topological charge density in (c) and (d). The antiskyrmion has a different helicity (H), leading to an opposite topological charge while keeping the polarity (P) of the skyrmion constant. Another topologically nontrivial spin texture is the meron, which is a quasiparticle with a spin rotation of only $180°$ from one side to the other (see Figs. 1.7(e),(f)), crossing the meron center. In contrast to the $360°$ rotation of a skyrmionic configuration, this leads to a total topological charge of $Q = 0.5$ or $Q = -0.5$, respectively. As for the skyrmion a change in helicity while keeping the polarity the same results in opposite topological charge.

Skyrmion	$P=1$	$P=-1$
$H=1$	1	-1
$H=-1$	-1	1

Meron	$P=1$	$P=-1$
$H=1$	0.5	-0.5
$H=-1$	-0.5	0.5

Table 1: Topological charge of skyrmions and merons with different helicity and polarity.

Naturally, more combinations of different polarity and helicity than those presented in Fig. 1.7 are possible. In Table 1, all relevant combinations that are not trivially related to each other by trivial symmetry operations are considered. Concluding, different signs of helicity and polarity result in a change of topological charge compared to configurations with the same signs.

Due to their small size and topological protection, skyrmions and merons are potential candidates for promising improvements in data storage density in the field of spintronics [9–11]. Two proposals are skyrmion or domain wall racetrack memory devices [78, 79].[2]

---

[2] a few sentences in this chapter are cited from my master thesis [80]

2 Instrumentation and Measurement Techniques

Almost all measurements presented in this thesis were obtained using a multi-chamber ultra-high vacuum (UHV) system, which offers several opportunities for sample preparation and analysis. Since the second chamber system used for this thesis consists of similar components and preparation tools, the following section will focus on the primarily used UHV system (see details for the other UHV system in [81]). The two low-temperature scanning tunneling microscopes and the location of each relevant preparation facility are described in the following section. Additionally, the measurement methods used are introduced, and the relevant contrast mechanisms contributing to the signal in the scanning tunneling microscopy (STM) measurements discussed in this thesis are examined.

2.1 The Ultra-High Vacuum Chamber System

The mostly used unique UHV-system consists of seven separated chambers with a base pressure lower than 10^{-10} mbar which is maintained by ion-getter pumps[3] and titanium sublimation pumps[4]. The entire system floats on a passive air-damped table which is placed on a decoupled foundation. With transfer arms and mechanical hands samples are transferred within the chambers. A sketch of the chamber system and the relevant features of each chamber is shown in Fig 2.1. The central chamber of the system is the R2P2-chamber designed by Omicron, which allows the distribution of the sample to each side chamber. For the sample preparation, three procedures are essential to optimize the surface cleanliness of a sample surface, namely O_2-glowing (preparation chamber), argon ion sputtering (analysis chamber) and high-temperature flashes (HTF) with an e-beam heater (preparation chamber). The e-beam heater is able to heat the samples over $2000°\mathrm{C}$ which allows to remove the majority of contaminations of a single crystal. Afterwards, the sample is transferred to a Knudsen cell or e-beam evaporator in the MBE-chamber and by using a variety of high-purity elements, ultrathin layers can be deposited on top of the sample surface. Additionally to the features in Fig. 2.1, the analysis and preparation chambers also have a resistance heater to heat the sample to a couple of hundred degrees Celsius.

---

[3] accelerates ions to sputter a getter material which is an active pumping element

[4] evaporates titanium in intervals between 4 and 8 hours into the chamber to bind the residual gas molecules

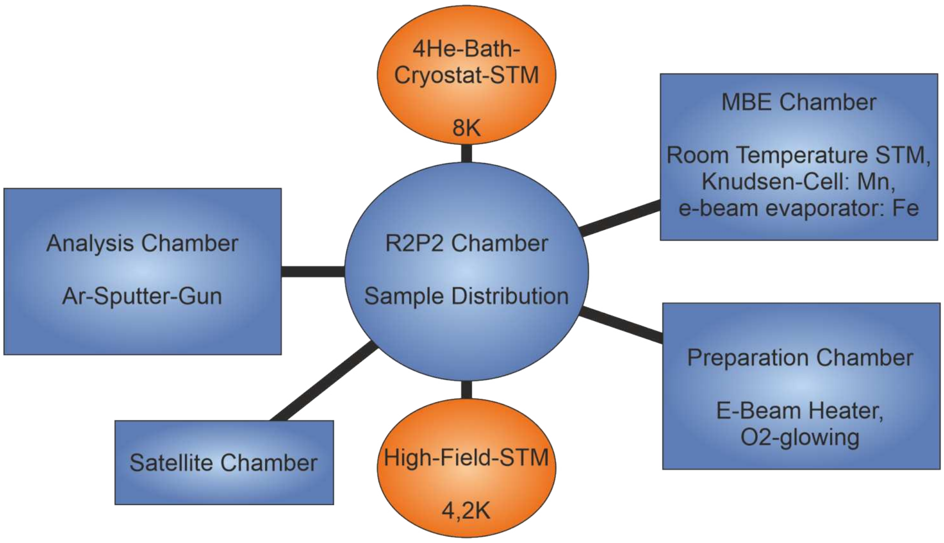

Figure 2.1: Sketch of used ultra-high vacuum chamber system. Experimental setup of the UHV-chambers with facilities which were used during sample preparation and analysis.

2.2 Low-Temperature Microscopes

The system has two low-temperature microscopes: the **4He-Bath-Cryostat-STM** [82–84] is cooled by a connected tank filled with liquid helium. A second tank encases the first one and is filled with liquid nitrogen. If both tanks are filled the microscope has a working temperature of 8 K. For sample pre-characterization, the system can be operated at temperatures of 100-150 K with a filled outer tank with liquid nitrogen or even at room temperature without any cooling. At 8 K, a magnetic field of up to 2.5 T can additionally be applied perpendicular to the surface by using a superconducting coil.

Cr and W are common materials for STM tips. W tips were prepared from a W wire, electrochemically etched in a saturated NaOH solution. W tips are appropriate for non-magnetic measurements. Another common kind of tip are chemically etched Cr tips, which have a randomly orientated magnetic moment at the tip apex and do not exert any stray fields. The choice of the tip strongly depends on the desired experiment. Cr-tips are used for experiments in which the sample magnetization should respond to the external magnetic field, while the magnetic state of the tip needs to stay fixed. Cr tips were used for all measurements in this thesis, also in the second low-temperature microscope, the **High-Field-STM**. It is cooled by coupling a liquid helium bath via helium exchange gas. The typical working temperature is 4.2 K. Utilizing the Joule-Thompson-effect [85], the microscope can reach a temperature of approximately 1.3 K. The perpendicular magnetic field of up to 9 T, produced by a superconducting coil, and the low-temperatures offer the opportunity to investigate and manipulate metallic samples under extreme conditions including the ability to switch between the normal conducting and superconducting phase of a sample system.

2.3 Scanning tunnelling microscopy

The first working scanning tunneling microscope was developed in 1981 by Gerd Binnig and Heinrich Rohrer [86]. A few years later, spin-polarized scanning tunneling microscopy (SP-STM) was introduced [87]. Since then, it has enabled the detection of magnetic properties down to the atomic scale based on the quantum mechanical tunneling effect. The theoretical concepts of STM and SP-STM will be sketched in the following. The approach of two metals up to a distance of some Å results in a tunnel current until the Fermi levels of both are equal. An additional bias voltage between both electrodes causes a shift of the two Fermi energies E_{F} that leads to a continuous and detectable current of some nA. According to the Tersoff-Hamann theory [88], the tunnel current between a metallic tip and a metallic sample in a typical limit of small bias and low-temperatures is given by:

$$I = \frac{2\pi e^2}{\hbar} V \sum_{\mu\nu} |M_{\mu\nu}|^2 \delta(E_\nu - E_F)\delta(E_\mu - E_F). \tag{2.1}$$

In Eq. 2.1, V is the bias voltage between tip and sample, E_F the Fermi-energy, E_μ,E_ν the energies of the states ψ_μ,ψ_ν and $M_{\mu\nu}$ the matrix elements describing tunneling between the tip state ψ_μ and the sample state ψ_ν. The matrix elements $M_{\mu\nu}$ can be expressed as:

$$M_{\mu\nu} = -\frac{\hbar^2}{2m} \int d\mathbf{S}(\psi_\mu^* \nabla \psi_\nu - \psi_\nu \nabla \psi_\mu^*). \tag{2.2}$$

The integrand can be interpreted as a current density operator for a current from state ψ_μ to state ψ_ν. The integration is over an area which lies entirely inside the region between the tip and the sample. The description of SP-STM needs to separate the tunnel current into two components of spin-polarized current. In general, the current between a magnetic domain of the sample and a magnetic tip at place $\mathbf{r}_{\mathrm{T}}$ can be expressed as [89–91]:

$$I_{\mathrm{tot}}(\mathbf{r}_{\mathrm{T}}, V, \theta) = I_{\mathrm{Ele}}(\mathbf{r}_{\mathrm{T}}, V) + I_{\mathrm{Mag}}(\mathbf{r}_{\mathrm{T}}, V, \theta) \tag{2.3}$$

$$I_{\mathrm{tot}}(\mathbf{r}_{\mathrm{T}}, V) \propto \eta_T \tilde{\eta}_{\mathrm{S}}(\mathbf{r}_{\mathrm{T}}, U) + \mathbf{m}_{\mathrm{T}} \tilde{\mathbf{m}}_{\mathrm{S}}(\mathbf{r}_{\mathrm{T}}, V), \tag{2.4}$$

where θ is the angle between the tip magnetization $\mathbf{m}_\mathrm{T}$ and the sample magnetization $\mathbf{m}_\mathrm{S}$, $\tilde{\eta}_\mathrm{S}$ is the integrated LDOS and $\tilde{\mathbf{m}}_\mathrm{S}$ is the vector of the integrated local magnetization DOS of the sample. In Eq. 2.4, $\eta_\mathrm{T} = \eta_\mathrm{T}^{\uparrow} + \eta_\mathrm{T}^{\downarrow}$ is the DOS of the tip and $\mathbf{m}_\mathrm{T} = (\eta_\mathrm{T}^{\uparrow} - \eta_\mathrm{T}^{\downarrow})\mathbf{e}_\mathrm{T}$ is the magnetization DOS of the tip, with $\mathbf{e}_\mathrm{T}$ being a unit vector in the direction of the tip magnetization. The spin-polarized current is a consequence of an unbalanced ratio of occupied spin-up and spin-down states, which leads to a different probability of tunneling into unoccupied spin-up and spin-down states of the sample (see Fig. 2.2 b)). With the assumptions of a constant magnetic field $\mathbf{B}$, a temperature of $T \approx 0$, and within an s-orbital approximation for the tip and sample states (details of the derivation in [89]), the spin-polarized tunnel current is given by:

$$I(\mathbf{r}_\mathrm{T}) \propto \sum_a \exp(-2\kappa|\mathbf{r}_\mathrm{T} - \mathbf{r}_a|)(1 + P_\mathrm{T}P_\mathrm{S}\cos\alpha_a), \tag{2.5}$$

where $\mathbf{r}_a$ describes the position of the surface atoms a, and α the corresponding angle of the surface spins to the magnetization axis of the tip. $P_{T,S} = (\eta_{T,S}^{\uparrow} - \eta_{T,S}^{\downarrow})/(\eta_{T,S}^{\uparrow} + \eta_{T,S}^{\downarrow})$ indicates the spin polarization of tip and sample. The dependence of the tunneling current on $\mathbf{r}_T$ and $P_\mathrm{T}P_\mathrm{S}$ in Eq. 2.5 is used to measure high-resolution images with magnetic contrast (tunneling magnetoresistance effect, TMR). The most common mode of STM is the constant-current mode. Every difference in LDOS leads to a higher/lower tunnel current. To keep the same current value, piezo elements are regulating the height of the tip. In imaging mode, the tip scans an image area line by line with constant current while the height of the tip $z(x, y)$ is measured (see Fig. 2.2). The measured Z-signal also contains, besides the topographical information, information about the polarization of the tip and sample.

2.4 Scanning tunneling spectroscopy

Another signal that can be recorded is the differential tunneling conductance (dI/dV). It is detected with a lock-in technique, where the bias is modulated by a high frequency signal in a small interval around the chosen constant bias energy. The change of the reference signal is proportional to the LDOS of the sample at the location of the tip and the energy chosen:

$$\frac{\mathrm{d}I}{\mathrm{d}V} \propto \eta_\mathrm{S}(\mathbf{r}_\mathrm{T}, E_\mathrm{F} + eV). \tag{2.6}$$

The measurement of dI/dV is referred to as STS or spin-polarized STS. For the spectroscopic measurements, the tip is positioned above a desired sample location at a bias voltage V_stab and a tunnel current I_stab. For STS measurements, a fixed tip-sample distance is required to exclusively vary one parameter (see equation 2.6).

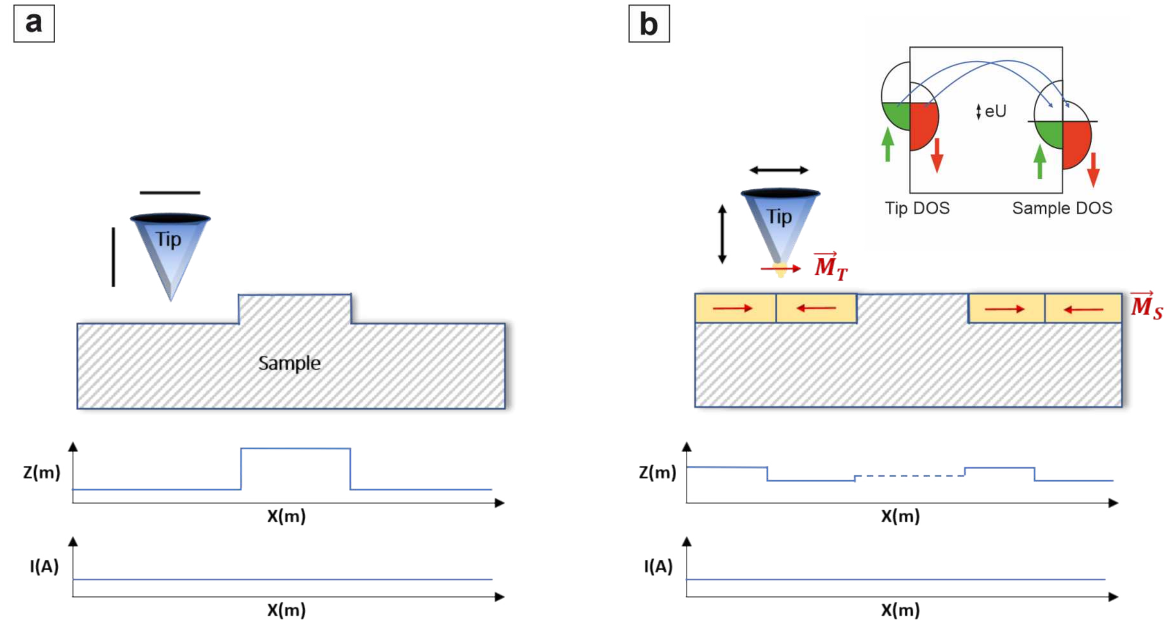

Figure 2.2: Principles of STM and SP-STM. Geometry of the experimental setup. (a) Conventional STM and (b) SP-STM with magnetic tip and sample, including a sketch of the spin-conserving tunneling process between tip and sample.

Consequently, the feedback loop needs to be opened for the entire measurement. To acquire the data, the bias voltage is swept while the dI/dV signal is measured using the lock-in technique. A small sinusoidal modulation voltage of frequency f_{mod} is added to the sample bias. For the results presented in this thesis, a frequency of $f_{\text{mod}} = 4777$ Hz was used. The measured signal is the broadened response to the swept bias voltages in the energy range $\pm V_{\text{mod}}$. The lock-in amplifier multiplies a reference signal of the same frequency with the original measured signal and integrates it over time. Given that sine waves with different frequencies are orthogonal to each other, filtering signals with the exact frequency f_{mod} using this lock-in technique is highly effective and results in an excellent signal-to-noise ratio.

Energy resolution in scanning tunneling spectroscopy

Various factors determine the energy resolution in STS experiments. The majority of broadening effects originate from the finite temperature in the STM setups. In this thesis, results with either a measurement temperature of $T = 4.2$ K or $T = 1.3$ K are presented. Based on the simplified picture of a Fermi-Dirac distribution with broadening, which reflects the full width at half maximum of the curve and describes thermally excited tunneling around the Fermi level, it is possible to estimate the thermal broadening in STS measurements. Since the modulation voltages can also contribute to the broadening of the signal, only a small modulation voltage of $V_{\text{mod}} = 50\ \mu$V was chosen for the low-temperature measurements. The consideration of both effects for the estimation of the energy resolution can be expressed as:

$$\Delta E = 3.5 k_{\text{B}} T + E_{\text{mod}}. \tag{2.7}$$

This relation leads to the energy resolutions of $\Delta E(T = 4.2\ \text{K}) = 1.32$ meV and $\Delta E(T = 1.3\ \text{K}) = 0.44$ meV. Due to the difference of almost one order of magnitude between thermal broadening and the broadening related to the lock-in technique, the thermally related effects are the dominant contribution in the estimated energy resolution. Note that unwanted instabilities in the bias voltage and capacitive effects can further decrease the energy resolution. Ultimately, a reduction of the influence of external frequencies during the measurements is realized by high frequency filters close to the microscope.

2.5 Further Techniques

This section continues with the introduction of the measurement techniques used in this thesis and presents additional tools implemented in the Nanonis software, which supported the analysis of the sample systems.

Spatial variation

Another way to acquire spectroscopic information about the sample is to measure the spatial variation of the LDOS. Therefore, line spectroscopic measurements in one dimension, e.g., above certain edge orientations, or dI/dV maps in two dimensions, e.g., measuring the bulk properties of an island, can be performed. Furthermore, the sample can also be probed in either constant-height or constant-current mode while recording the dI/dV signal at a fixed bias voltage V. To obtain a constant-height map, a certain bias voltage is chosen and the feedback loop is turned off for the entire measurement of the scan area.

Multipass mode

The multipass mode is another versatile tool for investigating sample surfaces and enables measurements at zero bias voltage. This mode operates as follows: the software first measures one line in constant-current mode (at voltage V and current I) and then replays the line with the feedback turned off, optionally at a different tip-sample distance by adding z_{offset}. Additionally, during the repetition of the first scan line, it is possible to change the sample bias (V_{meas}). Primarily, a bias voltage of $V_{\mathrm{meas}} = 0$ V was chosen for the measurements where the sample was in the superconducting phase to be as deep as possible inside the superconducting gap of the sample system. In other words, during this measurement the current and dI/dV signal, by repeating the initial Z signal at a different bias voltage, can be obtained. The current signal measured in multipass mode can be interpreted as the asymmetry of the tunnel current around the chosen bias voltage V_{meas} in the range between $\pm V_{\mathrm{mod}} = 50\ \mu$V. Repeating this procedure for the entire scan frame results in a current and dI/dV map and presents a valid alternative measurement method to the more established constant-height maps. To compare with the earlier introduced measurement techniques, focusing on one or a few bias voltages in multipass mode allows for much faster data acquisition compared to the STS grid spectroscopy. In comparison to constant-height measurements, the multipass mode includes differences in the LDOS while considering the topographic structure of the surface separately, whereas in constant-height measurements the topographic information is included in the measured signal. This can lead to differences in the measured LDOS, especially in the vicinity of edges, where in multipass mode the tip detects also a lateral current flow in contrast to constant height measurements above edges.

2.6 Contrast mechanisms in scanning tunneling microscopy

Conventional SP-STM is based on the TMR effect, in which the signal scales with the cosine of the angle enclosed by the tip and sample magnetization. This means the TMR reflects directly the magnetic components of the spin texture and is always present in the case of a spin-polarized tip (see TMR case in Fig. 2.3). Further, two additional effects called tunneling anisotropic magnetoresistance (TAMR) [92, 93] and non-collinear magnetoresistance (NCMR) [94–96] can occur by imaging non-collinear spin textures also with a non-magnetic tip. In the first case, TAMR, the local magnetization direction affects the local electronic states due to SOC. In STM measurements, a different signal for in-plane magnetized sample locations compared to sample locations with out-of-plane magnetization is obtained. In contrast to TMR, measurements obtained with a tip dominated by the TAMR effect exhibit a modified signal. In the case of a magnetic spin spiral, the measured period would be half of the actual magnetic period of the spin spiral due to the crossing of in-plane and out-of-plane magnetization twice per full rotation of the spin spiral texture (see TAMR case in Fig. 2.3).

The NCMR effect originates from the spin-mixing of majority and minority spin

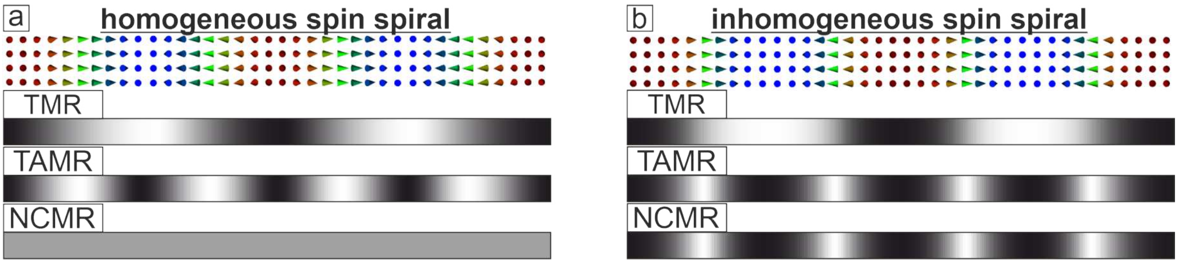

Figure 2.3: Contrast mechanisms with magnetic and non-magnetic tips. Expected signals for TMR, TAMR and NCMR effects for a homogeneous spin spiral in (a) and an inhomogeneous spin spiral in (b). Both spin spiral configurations are visualized at the top of each panel and were created in Monte Crystal [64].

channels in a non-collinear spin structure and results in different electronic states between non-collinear and collinear configurations. Taking the example of a magnetic spin spiral again, the easy axis of a system will affect the width of the in-plane and out-of-plane regions, resulting in more collinear local spin configurations through the propagation direction of the spin spiral (inhomogeneous spin spiral, see Fig. 2.3(b)). If the present anisotropy energy is large enough, this effect will again lead to half of the magnetic period of the spin spiral in the measurements (see NCMR case in Fig. 2.3(b)).

Since it is difficult to identify which effect is dominating in the experiments, the term electronic magnetoresistance (EMR) is used in later chapters, as both effects are related to changes in the local electronic states originating from the non-collinearity of the spin textures. Consequently, in SP-STM measurements, all three effects can contribute to the measured signal. Notably, the separation of TMR and EMR-related contributions to the signal is possible, as it will be shown in sec. 6.2.

3 Non-collinear spin textures on a square symmetric lattice in Mn on W(001)

After the first prediction of skyrmions in 1989 [75], skyrmion lattices were experimentally observed for the first time in 2009 using neutron scattering on the helical magnet B20 compound MnSi [97]. The first observation of individual magnetic skyrmions was reported in 2013 [22], where the bilayer of PdFe on Ir(111) was investigated. Since then, the skyrmions attracted more and more attention, due to their potential application in spintronic devices [98–100]. New sample systems were discovered, but interface-induced skyrmions were so far only observed on hexagonal surfaces. This chapter is dedicated to the first observation of nanoscale interface-induced magnetic skyrmions on a square symmetric lattice in the sample system of one atomic layer of Mn on W(001). The key improvements in sample preparation and the magnetic ground state at zero and finite magnetic field will be explored. Parts of the results in this chapter originate from my master thesis [80] and were published in the collaborative work of Ref. [101].

3.1 Previous work on Mn/W(001)

Both, theoretical and experimental analyses of the system of Mn/W(001) were already published [102] and the goal was to extend the experimental observations with an improved experimental setup. The images labeled (a)-(c) in Fig. 3.1 were obtained in the same laboratory as those presented in this thesis. The motivation for additional investigations originates from the availability of a higher magnetic field capacity of 9 T, compared to the maximum of 2.5 T available during the measurements back in 2006 [102]. At that time, the 2.5 T field strength was insufficient to induce the phase transition to a skyrmion lattice. More recent theoretical work by Nandy $et\ al.$ [104], depicted in Fig. 3.1 (e), predicts the critical field for a phase transition from a spin spiral phase to a skyrmion lattice phase at around 20 T. In continuation of the studies referenced in [102], further, yet unpublished simulations by E. Vedmedenko, which utilize slightly different parameters and consider fewer nearest neighbors exchange constants, indicated the formation of skyrmions already at 9 T. The preparation of the sample system and the presence of skyrmions within this magnetic field range will be further discussed in the subsequent sections.

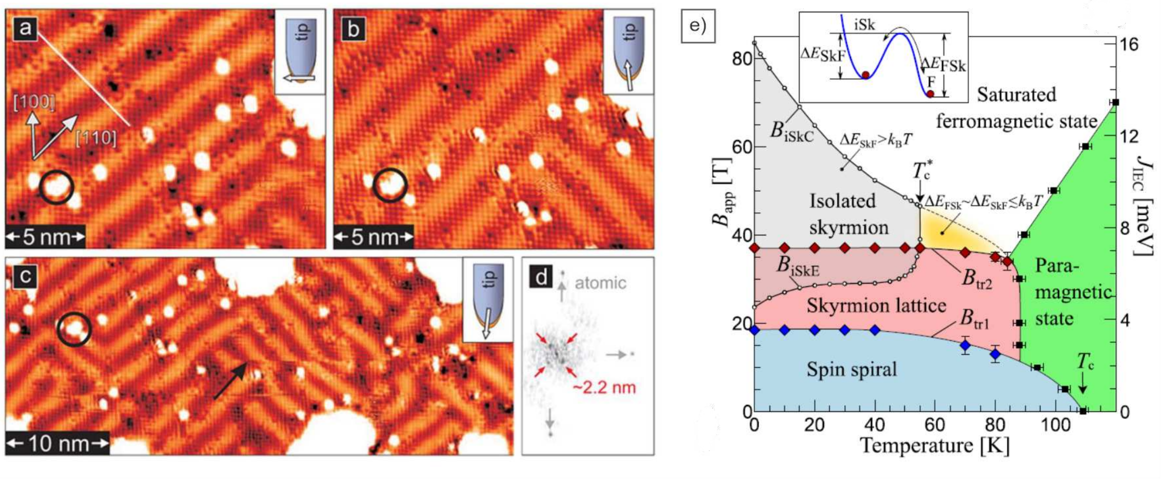

Figure 3.1: Previous SP-STM measurements and the predicted magnetic ground state of Mn/W(001). The results in (a)-(d) were extracted from [102], and the plot in (e) was extracted from [103]. In (a)-(c), spin-resolved STM measurements of one monolayer of manganese on W(001) are depicted. In panels (a) and (c), the measurements were performed at 0 T, while in (b), a magnetic field of 2 T was applied. Panel (d) shows the Fourier transformation with a resulting spin spiral period of roughly 2.2 nm. In (e), recent simulations are presented that predicted the magnetic phase diagram of Mn/W(001).

3.2 Preparation and Magnetism of Mn/W(001)

3.2.1 Preparation of clean Mn/W(001)

Contamination in a UHV chamber mainly occurs by the adsorption of residual gases on the substrate or the segregation of atoms from the bulk to the surface of the crystal. Hydrogen, along with carbon, oxygen, and their compounds, is typically found in the residual gases of the chamber. Depositing a monolayer of Mn on W(001) was particularly challenging due to the reactive nature of W(001) compared to the denser, hexagonal surfaces of established skyrmion systems [22, 105]. For W single crystals it is well known that carbon is enclosed inside the bulk of the crystal [106, 107], and this carbon might reach the surface due to annealing processes during the sample preparation, thereby inducing reconstructions. By trying several approaches to obtain a clean surface, substrate temperature control during evaporation and limiting the material to not exceed one monolayer, is crucial for achieving a clean preparation. Notably, also a dependency of the surface cleanness on the number of desorption flashes of the sample is observable, suggesting that carbon may also form compounds with the Mn layer that can be removed by HTFs. Further details of the optimized preparation procedure is presented Ref. [80]. The best

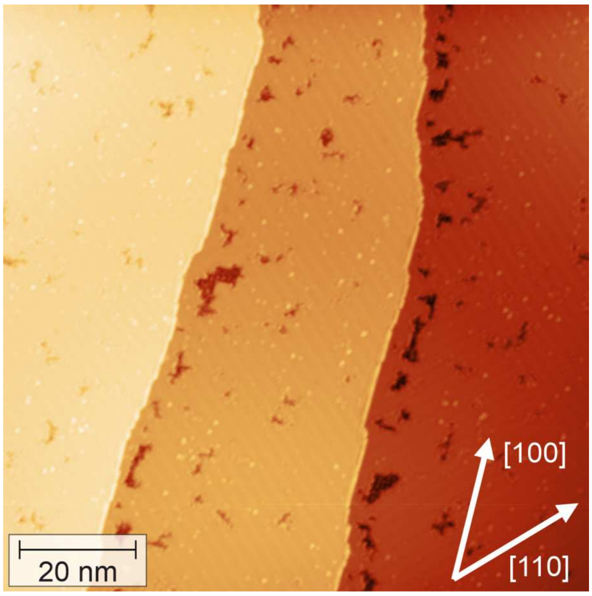

Figure 3.2: Optimized growth of the monolayer of Mn on W(001). A SP-STM constant-current image of the virgin state of the sample with large rotational domains of the spin spiral state in the Mn monolayer on W(001) at $B = 0$ T is shown, where the terraces are separated by two atomic step edges. ($T = 4.2$ K, $V = -0.05$ V, $I = 3$ nA).

sample quality achieved is shown in Fig. 3.2. The measurement shows 0.95 atomic monolayer of Mn on W(001) with a few vacancy islands inside the monolayer and some residual bright spots most likely related to residual carbon contaminations on the surface. The majority of the area shows a pseudomorphic Mn layer in which stripes are weakly visible. The stripes are originating from the magnetic ground state of the system, which will be discussed in the next section.

3.2.2 Magnetic ground state at zero field and domain walls in Mn/W(001)

In this section, the focus will be on the magnetic ground state of the pseudomorphic area in the sample system. Figure 3.3(a) displays a constant-current SP-STM image obtained at zero field, where the striped pattern along $[110]$ results from the expected magnetic spin spiral. The period of this magnetic texture is 2.2 nm, i.e., about five times the diagonal of the square atomic lattice. This observation is in agreement with the previous experimental results by Ferriani $et\ al.$ [102] and based on Density Functional Theory (DFT), the origin of the ground state was explained by the frustrated exchange interactions together with a significant DMI of strength $D = 4.6$ meV/atom plus an out-of-plane magnetocrystalline anisotropy of $K = 3.6$ meV/atom. The coupling of the wave vector of the spin spiral to the square symmetric lattice with a four-fold symmetry results in two rotational domains. Between these domains, a large

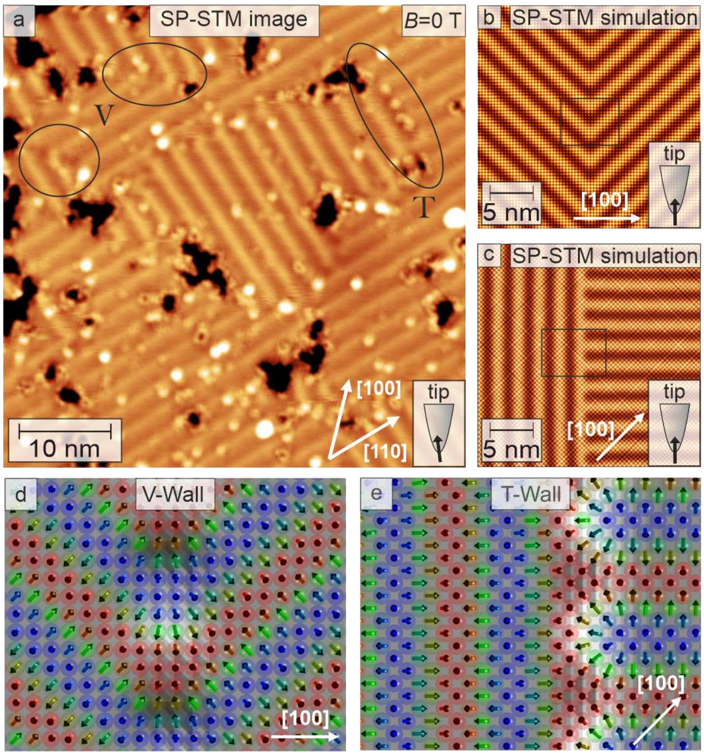

Figure 3.3: Domain boundaries of the magnetic ground state. (a) Spin-resolved constant-current STM image of 0.9 monolayer Mn/W(001) at $B = 0$ T in remanence obtained with a magnetic tip mostly sensitive to the out-of-plane component of the sample magnetization. The ellipses mark two different types of rotational domain-wall configurations of the spin spiral phase. (b),(c) SP-STM contrast simulations of a V wall and a T wall are depicted. The walls were set up and then relaxed with an atomistic spin dynamics code [64]. (d),(e) Simulated spin configurations of both types of rotational domain walls within the areas marked in (b),(c) are shown. Each arrow represents the magnetic moment of a single Mn atom, green indicates in-plane moments, whereas red and blue indicate opposite out-of-plane moments. The gray scale indicates the topological charge density. ($T = 4.2$ K, $V = -0.05$ V, $I = 3$ nA)

number of domain boundaries (also visible in the previous work, see 3.1(c)) in the remanent state of the sample system (see Fig. 3.3(a)) compared to the virgin state of the sample (see Fig. 3.2) is visible. Consequently, the formation of different types of domain walls is observable, and V and T walls are identified, which are indicated by the black ellipses and were not discussed in the previous work.

For further understanding, atomistic spin dynamic simulations with Monte Crystal [64] by solving the Landau-Lifschitz-Gilbert equation were performed. A Hamiltonian describing a system of interacting spins up to the third-nearest neighbors, including DMI as well as magnetocrystalline anisotropy, was considered. The spin spiral periodicity was reproduced with a pairwise isotropic Heisenberg exchange of

$J_1 = +18.7, J_2 = -4.4$, and $J_3 = -2.65$ meV/atom among nearest-, next-nearest, and next-next-nearest neighbors, respectively.

Several SP-STM contrast simulations were performed and a simulated V wall is depicted in Fig. 3.3(b), where the mirror symmetry of this domain wall type is visible. The magnetic moments of the spin texture within the black rectangle of 3.3(b) are sketched in 3.3(d). With 4.5 times the diagonal of the square atomic lattice, the simulated spin spiral is in good agreement with the experimental observations. The energy cost for such a domain wall boundary with respect to a perfect spin spiral is 12.7 meV/nm. In contrast to the coplanar nature of the rotational domains, the spins within the wall form a three-dimensional magnetic texture, resulting in a non-trivial topological charge Q. The nonvanishing local topological charge density is visible in Fig. 3.3(d), as indicated by the bright (high density) and dark (low density) regions. However, the net topological charge Q along the domain wall exactly cancels, making this wall topologically trivial.

Another SP-STM simulation and a corresponding spin structure for a T wall is depicted in Fig. 3.3(c) and 3.3(e). In contrast to the V wall, the spin wave vector of the T wall is either parallel or perpendicular to the domain wall orientation. With an energy cost of 15.7 meV/nm, the energy for the creation of a T wall is comparable to a V wall. Consequently, both wall types can co-exist in the sample and are found roughly equally often, which agrees with the experimental measurements for different regions of the sample. In contrast to the V wall, the end of each spin-down stripe in Fig. 3.3(e) carries a nonzero Q and in contrast to the V wall, it adds up along the domain wall direction. One can view these parts as half a skyrmion formation and indeed, the identification in the simulations that there is a Q of 0.5 per spiral period is possible, which makes the T wall topologically distinct from the V wall configuration.

3.2.3 Spin textures at high magnetic field

In this section, the properties in an applied large magnetic field are discussed. Figure 3.4 displays the virgin state of the sample in panel (a), where the striped pattern, representing the magnetic spin spiral, is clearly visible. The additional and much smaller periodicity in the image, can be attributed to atomic resolution during this measurement. The bright spots in the image are likely carbon-related contaminations, saturated in the color scale. In panel (b), the same area as in (a) is shown, but with the application of the strongest available magnetic field of 9 T. A noticeable difference is observed between the two images. The stripes break, leaving small spiral segments with a few skyrmions in between, indicated by the cyan ellipses. That means at 9 T the system is in a transition phase between the pure spiral and skyrmion lattice phase. Similar results can be observed in the first observations

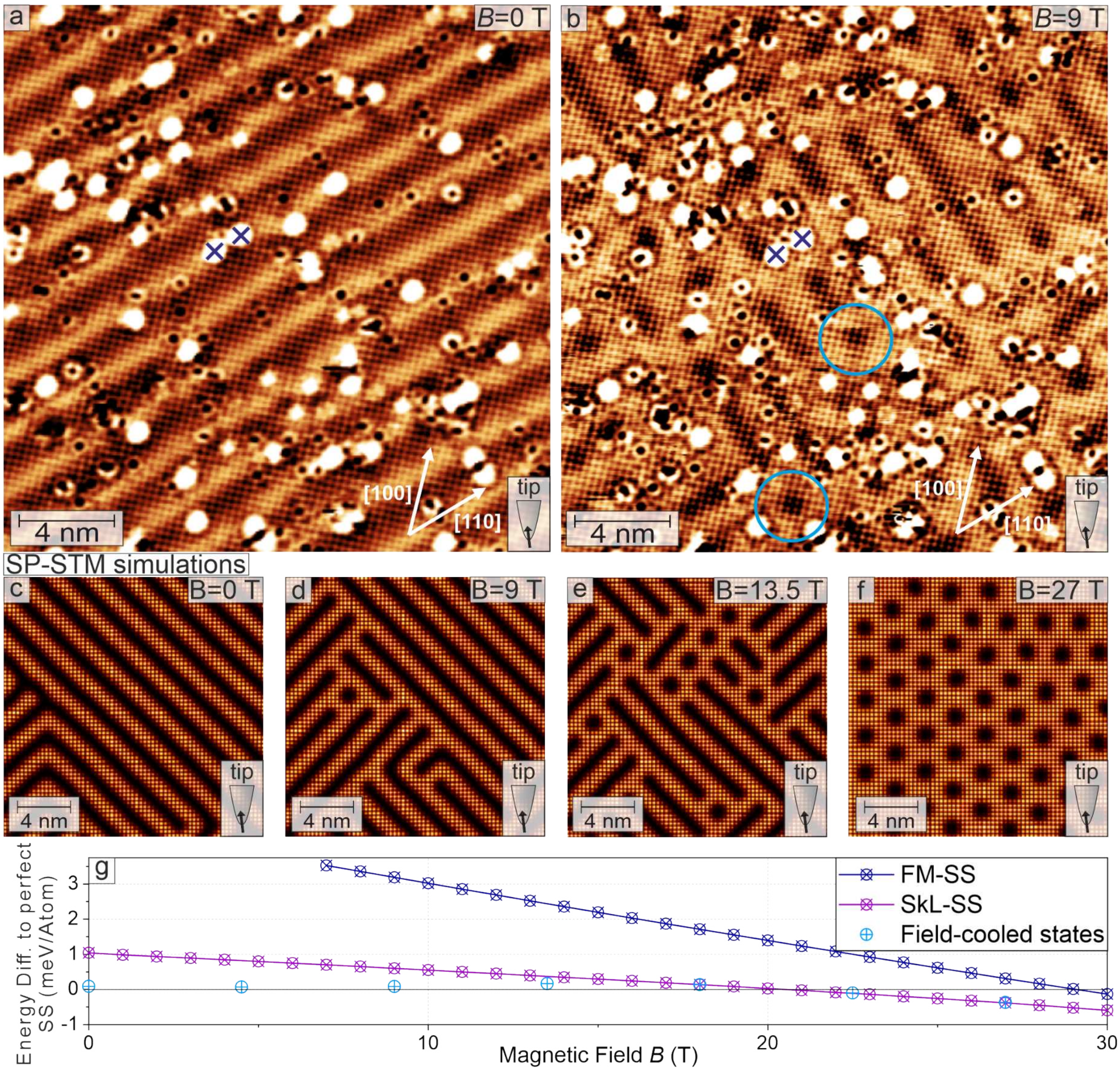

Figure 3.4: Field dependence of the magnetic ground state. (a) SP-STM constant-current image of a single-domain spin spiral state in the Mn monolayer on W(001) at $B = 2.4$ T. (b) Image of the same area at $B = 9$ T showing a mixed state of small spiral segments and skyrmions. (c)-(f) SP-STM simulations of magnetic states obtained using field cooling at different B fields as indicated. (g) Energy of the skyrmion lattice (SkL) and the FM state relative to the perfect spin spiral state at different magnetic fields as obtained from simulations using field cooling. Blue markers indicate the energies of the magnetic states displayed in (c)-(f) as well as additional, not presented data points. ((a),(b): $T = 4.2$ K, $V = -0.05$ V, $I = 3$ nA).

of skyrmion lattices [105], as well as in the first observations of interface-induced skyrmions [22]. In both works, the spin spiral also break into small segments, with either 3D skyrmion tubes or 2D skyrmions appearing in between, respectively. In contrast to the other sample systems, achieving either the pure skyrmion lattice phase or the individual skyrmion phase with a FM background was not possible due to the higher magnetic field requirements needed to exceed the phase transitions of the sample system.

To obtain a deeper understanding of the present skyrmions with spiral segments forming a mixed phase, several SP-STM simulations of magnetic states obtained by field cooling at different magnetic field strengths were performed and are shown in Figs. 3.4(c)-(f). At zero field, similar spin configurations for the simulated ground state, namely, a spin spiral state strongly coupled to the high symmetry directions of the square lattice with T and V walls, consistent with the experimental results, are observable. The simulated data with applied out-of-plane field indeed show both spin textures, i.e., spin spiral fragments and skyrmions (see Fig. 3.4(d-e)). At 9 T, the number of skyrmions does not precisely match the experimental observations but this may be attributed to the presence of defects in the Mn-layer. Since, e.g., higher-order terms are not considered in the simulations, by adding these the results might be improved too. The result acquired at 13.5 T shows a mixed state as in the experiment. At 27 T, a pure nearly hexagonal skyrmion lattice phase is identified. This skyrmion lattice appears in two differently oriented domains, which are rotated by 90° due to the lattice symmetry. The energy comparison of the simulated states (cyan data points in Fig. 3.4(g)) with those of the perfect spin spiral shows that they are very close to each other.

Consequently, the behavior of the two previously identified types of domain walls from Fig. 3.3 in applied magnetic field was investigated. The appearance

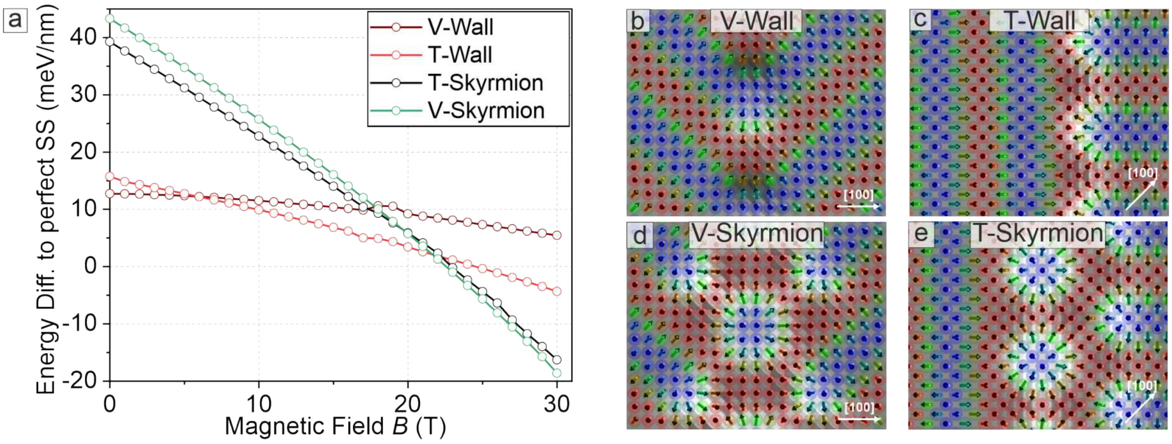

Figure 3.5: Magnetic field dependence of the energy of the rotational domain walls. (a) Energy per nanometer relative to the spin spiral for each type of rotational domain wall as presented in (b)–(e) at different magnetic fields. (b),(c) Spin structures of V and T walls. (d),(e) Spin structures of domain walls with lines of skyrmions in their centers.

of skyrmions can be understood by an extension of the model for the rotational domain walls (Figs. 3.5(b),(c)). This has been done by adding a line of skyrmions in the center of both domain wall configurations (see Figs. 3.5(d),(e)). The energy comparison in a magnetic field of the domain walls (Fig. 3.5(a)) shows that indeed, the introduction of rotational domain walls lowers the energy cost with increasing magnetic field. While the energy costs of T skyrmion walls and V skyrmion walls remain comparable across the entire range of investigated magnetic field values, the T wall configuration is favored in high magnetic fields due to the non-trivial topology of this type of wall.

For a more detailed investigation of the skyrmion properties and to identify the symmetry of the skyrmion arrangement, a different microtip was used, where the non-collinear magnetoresistance (NCMR) effect was dominant. The results of the measurement are depicted in Figs. 3.6(a),(b). The constant-current STM image displayed in Fig. 3.6(a) was obtained with a comparably small bias voltage of V=10 mV, where the NCMR effect often dominates the STM contrast. In some parts of the image, a pattern characterized by dark dots is visible. The distance between these dots is roughly 1.3-1.8 nm. Other SP-STM measurements offered a typical skyrmion-skyrmion distance of about 2.5 nm (see [101] for further details), indicating that the period of these dots is roughly half of the original distance between the skyrmions. A closer look into such a skyrmion arrangement in Fig. 3.6(b) reveals that some dots are slightly larger and darker. Furthermore, they are arranged in a hexagonal-like pattern with additional less dark dots around them. The distance between the darker dots corresponds to the expected skyrmion-skyrmion distance of 2.5 nm.

To identify the origin of the small dots, STM contrast simulations were performed, considering tunnel magnetoresistance (TMR) contrast (Fig. 3.6(c)) and NCMR contrast (Fig. 3.6(d)). Indeed, due to the short distance between the skyrmions, the NCMR effect leads to additional features appearing between skyrmions. Further simulations revealed that such an effect is not present in PdFe/Ir(111) [22], due to the larger spin spiral period of 6 nm, leading to a skyrmion-skyrmion distance which is not sufficient to create such features in between the skyrmions. In order to reproduce the experimental contrast, a mixed contrast of TMR and NCMR in a ratio of 1:45 was chosen. The result is depicted in one half of Fig. 3.6(e), with the magnetic texture used for the simulation in the background of the panel. This panel demonstrates good agreement with the measured pattern in the experiment and also suggests a hexagonal symmetry within the skyrmion lattice area.

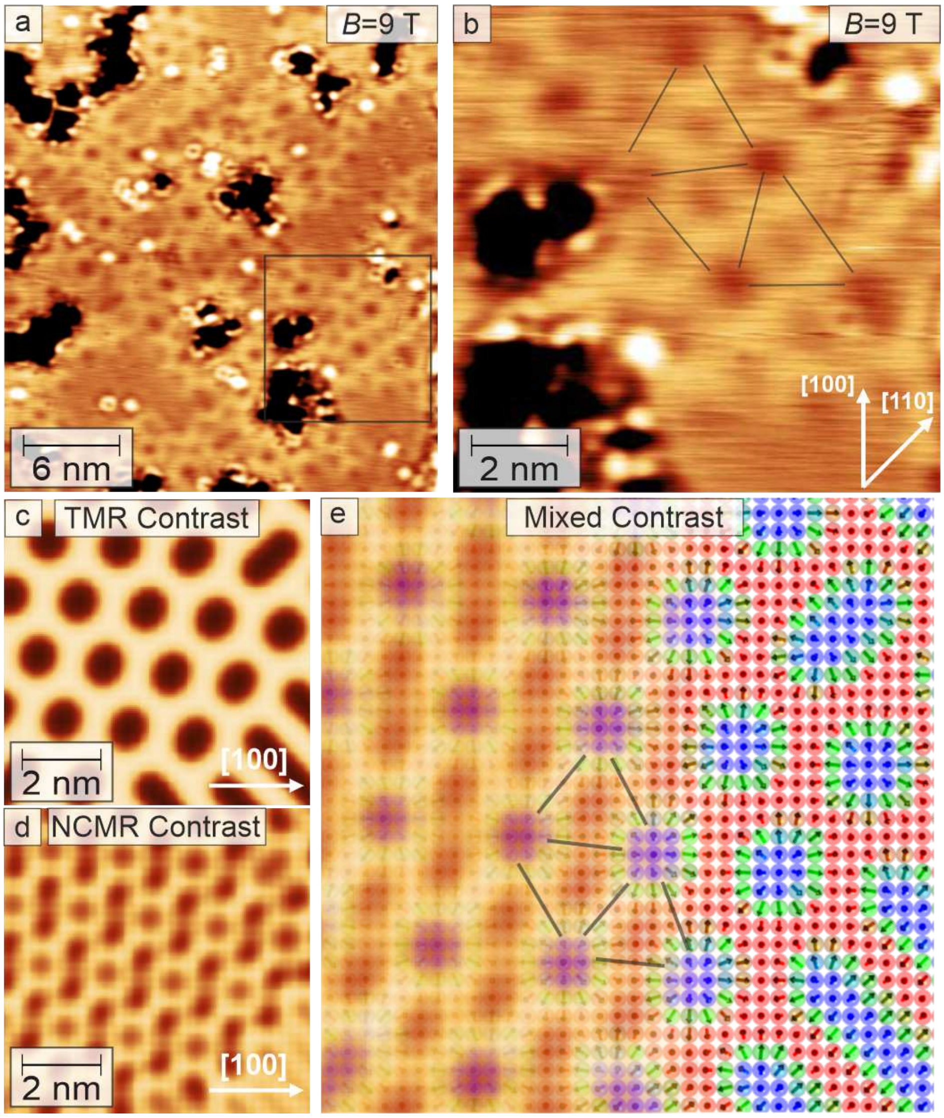

Figure 3.6: NCMR effect in skyrmion formations. (a) Constant-current STM image of the Mn monolayer on W(001) measured at $B = 9$ T and at a comparably small bias voltage of $V = 0.01$ V. (b) Closer view of the sample area indicated by the black box in (a). This region shows a roughly hexagonal pattern of dark dots. (c),(d) STM simulations using only tunnel magnetoresistance (TMR) and only non-collinear magnetoresistance (NCMR) contrast, respectively, of a magnetic state obtained by field cooling at 18 T. (e) STM simulation of the same magnetic state using both TMR and NCMR with a ratio of 1:45. In the background of the panel, a sketch of the spin configuration of the simulated state is depicted. ($T = 4.2$ K, $V = 0.01$ V, $I = 1$ nA).

Second Layer Mn on W(001)

At coverages above a monolayer, compact pseudomorphic second layer islands are observed. Figure 3.7(a) displays a spin-polarized differential conductance map with

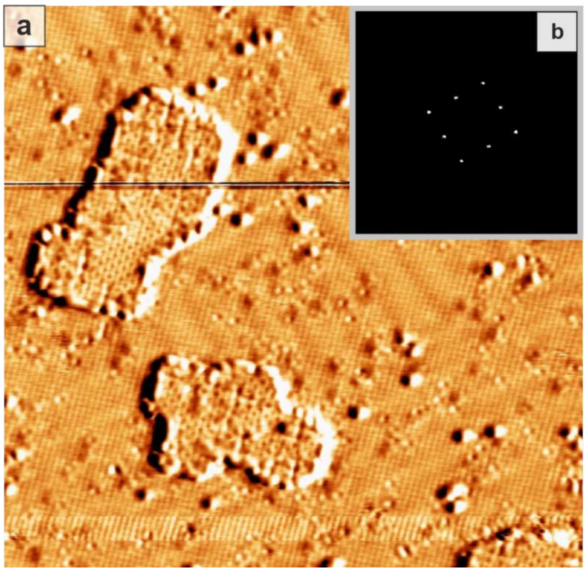

Figure 3.7: Second monolayer of Mn on W(001). Differential tunneling conductance map mixed with Fourier Transformation filtered image in (a) and the Fourier Transformation of the same scan area in (b). (constant-current STM: $V = -50$ mV, $I = 3$ nA, Cr-tip, $T = 4.2$ K).

atomic resolution and is a combination of the raw data with the FFT-filtered image of the measurement. For the FFT filtered image the Fourier Transformation (b) of the raw data was used. The monolayer exhibits the established spin spiral state, while the second monolayer is characterized by a c(2x2) AFM state, consistent with other studies of the sample system [108, 109]. The filtered maxima of the FFT are depicted in Figure 3.7(b). These features exhibit the four-fold symmetry of the AFM state, represented by four peaks, and additional four peaks corresponding to the atomic structure of the crystal lattice.

3.3 Summary and comparison to other sample systems

In summary, the first monolayer of Mn on W(001) provides a FM spin spiral with a period of roughly 2 nm, while the four-fold symmetry of the lattice leads to two rotational domains of the spin spiral. Both types of domains can either connect via a T- or V-Wall, whereas no wall type was preferred in the experimental observations. By applying a high magnetic field of 9 T, a transition of the pure spin spiral phase to a mixed phase including spin spiral segments and skyrmions is observable. The second monolayer of Mn offers a c(2x2) AFM ground state, aligning with the expected AFM nature of Mn bulk systems [110]. For comparison, another work worth mentioning is the sample system of one monolayer of Mn on W(110), where the first monolayer exhibits an AFM spin spiral ground state [111], solely by changing the lattice symmetry. Interestingly, a collinear c(2x2) AFM state can be observed by exchanging the evaporated material from Mn to Fe on the crystal surface of W(001), as shown in Ref. [112].

The prediction of the magnetic ground state of a sample system, particularly for ultrathin films where deviations in lattice constants and reductions of symmetry compared to bulk systems occur, is truly complex, as it is shown also by the following second sample system discussed in this thesis.

4 A non-collinear magnet-superconductor hybrid system in Fe/Ta(110)

Based on the understanding of non-collinear spin texture formation in magnetic layers on normal conducting metals, the next objective was to investigate such textures in proximity to a superconducting substrate. This required a change in substrate material, since the critical temperature of tungsten (≈15 mK) [113] cannot be reached by the used cryostat system. Tantalum, with its critical temperature of approximately 4.4 K, was identified as a suitable candidate for superconducting investigations in the experimental setup. Previous theoretical and experimental studies on a monolayer of Fe on Ta(110) had provided promising results, making this particular sample system a favorable choice for the desired investigations. In this chapter, the process of achieving a clean preparation of one monolayer of Fe on Ta(110) is examined. It begins by presenting the current state of related research on this sample system, and the motivation for this particular choice is further discussed. Subsequently, an introduction of an effective method for cleaning the Ta(110) surface to the desired level of cleanliness is presented. The chapter concludes with a detailed description of the optimization procedure for preparing clean Fe monolayers on the clean Ta(110) surface.

4.1 Previous work on the sample system

The combination of different experimental and theoretical techniques like DFT [114, 115] or tight-binding calculations [116], where the electronic structure and interactions are modeled, is essential for progress in condensed matter physics. In the field of non-collinear 2D-MSH-systems, highly relevant predictions were published prior to the work presented in this thesis. In the calculations by Nakosai $et\ al.$ [50], non-collinear and non-coplanar spin configurations in the vicinity to an s-wave superconductor were considered for the first time and predicted topologically non-trivial phases of superconductivity, the details will be discussed in Chapter 6.

By searching for a suitable sample system, one promising prediction using DFT calculations was published by Rózsa $et\ al.$ [117], where they investigated the potential magnetic ground states of a monolayer of Fe on Ta(110) by varying the interlayer distance. One of the predicted magnetic ground states for a certain interlayer distance is depicted in Fig. 4.1(a), namely a cycloidal spin spiral with a period of 5.98 nm and a propagation direction along $[1\bar{1}0]$. If the interlayer distance is comparable in the real system, an observation of this spin spiral texture is likely and it would be the realization of the desired sample system: a non-collinear spin texture in proximity

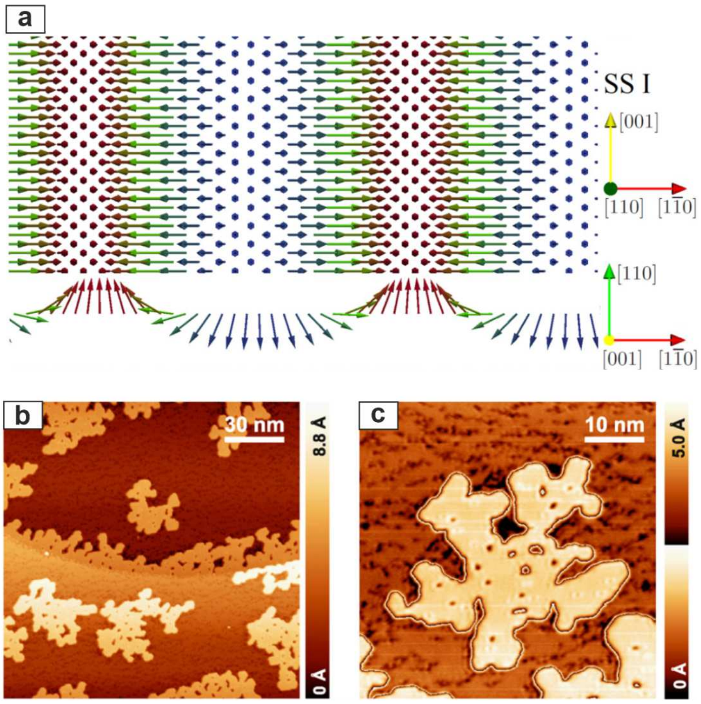

Figure 4.1: Previous works on the sample system of Fe/Ta(110). (a) DFT calculations [117] identified a cycloidal spin spiral as the magnetic ground state of one monolayer of Fe on Ta(110) for a certain interlayer distance. (b),(c) STM constant-current measurements from [118] revealed flat islands with irregular shapes as a typical growth morphology for the sample system.

to an s-wave superconductor.

Besides the theoretical predictions of the magnetic ground state of Fe/Ta(110) and the emerging physics of such a non-collinear MSH-system, a structural investigation with STM was done in [118] with an attempt to optimize the growth. The best-obtained result is shown in Figs. 4.1(b),(c). The Fe seems to prefer an island growth also mixed with step flow growth, with a lot of holes within the monolayer of Fe. The vacancies are likely related to enclosed contaminations of the Ta(110) surface. The magnetic properties of the monolayer were not discussed in that experimental work.

Since the work by [118] offered a pseudomorphic growth in Fe/Ta(110) and the theoretical prediction suggests a spin spiral as one of the possible magnetic ground states of the sample system, the monolayer of Fe was a promising candidate for realizing a non-collinear MSH-system for the investigation of the interaction between non-collinear spin textures with superconductivity.

4.2 Preparation and structural characterization of Fe/Ta(110)

The preparation of one monolayer of Fe on Ta(110) starts, as in the last chapter for W(001), with the optimization of the surface cleanness of Ta(110). Segregated oxygen from the bulk is one of the main contributions to the contaminations on the Ta surface, creating several kinds of oxygen reconstructions showing up in different patterns [118]. One established way to remove the oxygen reconstructions is applying HTFs, annealing the sample for a short period of time at high temperatures, e.g. in case of Ta above $2000°\mathrm{C}$. In Fig. 4.2(a), an initial preparation at the beginning of the optimization process is presented, where several superstructures are visible on the sample surface, resulting in numerous features in the corresponding Low-Energy Electron Diffraction (LEED) pattern (see inset). The preparation procedure involves two HTFs at $300\ \mathrm{W}$ for 30 seconds, with the surface side facing away from the e-beam filament. Since the sample plate is in between the filament and the single crystal, it leads to indirect heating of the Ta through the sample plate, meaning the sample plate always reaches the highest temperature during a HTF. The thermal connection to the crystal will determine whether the desired temperatures are reached. The result presented in Fig. 4.2(a) was obtained using the highest possible emission current of the e-beam stage. Due to this limitation, a flash of the sample with the surface facing downwards was necessary.

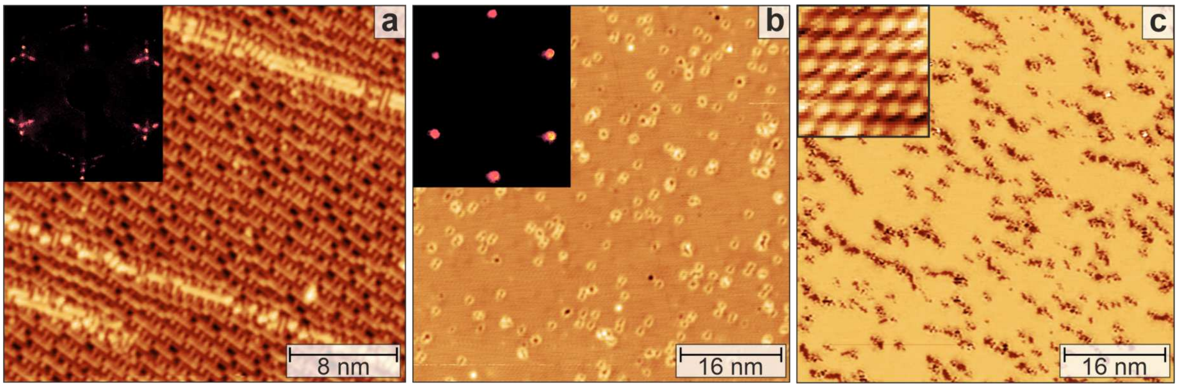

Figure 4.2: Cleaning procedure for Ta surfaces. (a) Measurement of a fully reconstructed Ta(110) surface with the corresponding LEED pattern as an inset. (b) Almost fully uncovered clean Ta(110) surface with individual defects and in the inset the corresponding LEED pattern of the sample. (c) A scan area just a few nanometers shifted from the area in (b) and measured at a comparable low bias voltage of 10 mV, with an inset showing atomic resolution of a reconstruction-free area. (STM constant-current: Cr-tip, $T = 4.2$ K, $I = 1$ nA (a) $V = 2$ mV (b) $V = 1$ V (c) $V = 10$ mV Inset: $I = 5$ nA $V = 10$ mV.

This method reduces the distance between the sample surface and the e-beam filament, leading to a reduction in the required power during the HTF. After several preparations to find the optimal power of the heater, the results shown in Figs. 4.2(b),(c) were obtained, where the oxygen reconstruction is almost fully removed, leading to the characteristic LEED pattern of clean bcc(110) crystals (see inset of Fig. 4.2(b)). The comparably low bias voltage in the STM-measurement presented in Fig. 4.2(c) leads to additional dark features following mostly the high symmetry directions of the crystal, which is characteristic of hydrogen on metallic surfaces. At higher bias voltages, as in Fig. 4.2(b), the weakly bound hydrogen gets enough energy to travel over the surface and is not visible in these measurements, with remaining defects, which are most likely oxygen-related defects. The inset in Fig. 4.2(c) shows the expected bcc(110) structure of the uncovered Ta(110) surface obtained by STM measurements with a comparably small distance between the tip and sample, resulting in atomically resolved images.

After optimizing the procedure to obtain a clean Ta(110) surface, subsequently, the deposition of Fe onto this surface is necessary. For the Fe deposition, molecular beam epitaxy [119] was used. Before achieving a clean pseudomorphic growth of the monolayer of Fe, a variety of superstructures within the monolayer were observed. In Fig. 4.3(a), a constant-current STM image is presented, highlighting the most prominent types of reconstruction encountered during the optimization process. A detailed examination of these reconstructions was performed during further preparations (see Figs. 4.3(b)-(d)). The color of the circles indicates which measurements correspond to which reconstructed region in the overview image of Fig. 4.3(a), where the gray color corresponds to the desired pseudomorphic area of Fe. These reconstructions were also observable in the sample system of one monolayer of Fe on Nb(110), for details see section 6.5. The second reconstruction is characterized by a dotted boundary at specific bias voltages and stripes within the enclosed area. All three reconstructions are strongly coupled to the twofold symmetry of the lattice, resulting in dotted or lined features along the crystallographic directions $[001]$ and $[1\bar{1}0]$. Additionally, an investigation of the structure of the second monolayer of Fe (see Figs. 4.3(e),(f)) was conducted. In (e), an island of the second layer of Fe on top of the fully reconstructed monolayer is shown. A closer at into the superstructure of the double layer is depicted in Fig. 4.3(f). A summary of the observed periods for the different types of reconstructions is presented below the STM measurements, where the periods along $[001]$ and $[1\bar{1}0]$ directions are shown. When comparing these values with the suggested structure model in [120] for the established reconstructions in Fe/Nb(110), the same conclusion follows: for the first reconstruction, the period fits the conventional rectangular unit cell, with the centered atom hidden. Regarding

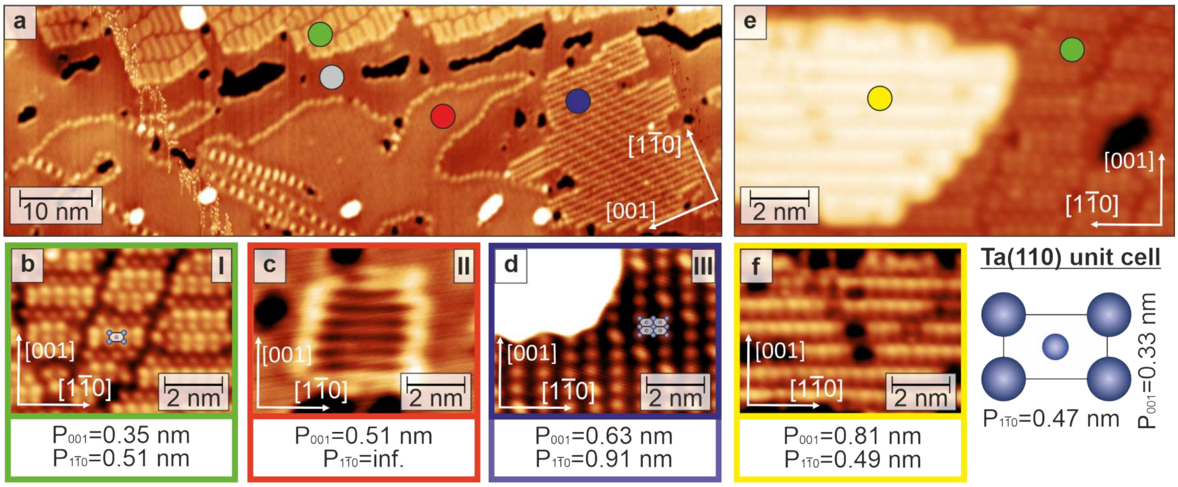

Figure 4.3: Types of reconstructions in the monolayer of Fe on Ta(110). (a) Overview image showing various types of reconstructions. (b) A detailed look at a region from panel (e), where the first reconstruction is measured with atomic resolution. (c) Another STM image of a tiny region of the second reconstruction. (d) STM image of the third type of reconstruction with atomic resolution. (e) STM image of a sample area with a second monolayer island and the first type of reconstruction in the background. (f) Zoom-in image into the second monolayer island of (e). (STM constant-current: Cr-tip (a) $T = 30$ K, $V = 20$ mV, $I = 1$ nA (b),(e),(f) $T = 4.2$ K, $V = 10$ mV, $I = 1$ nA (c) $T = 4.2$ K, $V = -30$ mV, $I = 1$ nA (d) $T = 33$ K, $V = -3$ mV, $I = 1$ nA.)

the third reconstruction, the period in both directions is twice the length of the unit cell.

After investigating the different types of reconstructions, the question remains: how can the preparation procedure be optimized to maximize the area of the pseudomorphic Fe monolayer? In Fig. 4.3, the amount of Fe deposited onto the surface always exceeds one monolayer. In Fig. 4.4(a), a dI/dV map of a constant-current measurement with a sample having a coverage lower than one monolayer is shown. This sample was obtained by using a deposition time of 2:15 minutes. The dark areas indicate the uncovered Ta substrate, while the bright areas represent the pseudomorphic Fe monolayer of the sample. The area of pseudomorphic Fe is clearly enlarged compared to the previously discussed preparations. To validate this tendency, Figs. 4.4(b),(c) show samples with deposition times of 2:30 minutes and 3:00 minutes, respectively. In (b), the dI/dV map shows areas of the first reconstruction (dark compact areas) and the second reconstruction (dark elongated regions). When the deposition time is increased as in the preparation depicted in (c), the area of both reconstructions enlarges further, and only tiny parts of pseudomorphic Fe remain. For all three preparations, the other relevant preparation parameters, such

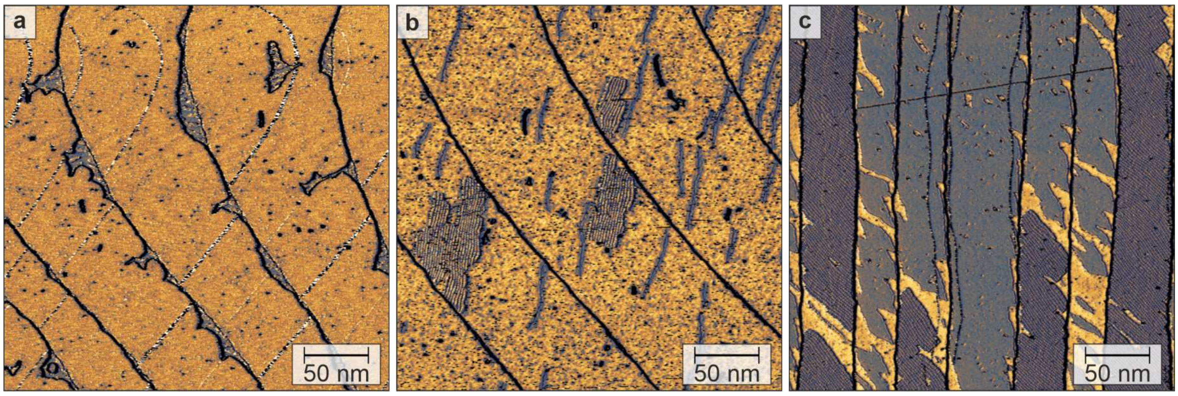

Figure 4.4: Sub-monolayer preparation in comparison to exceeding a monolayer of Fe on Ta(110). (a) dI/dV map of a sample preparation with a deposition time of 2:15 min. (b) dI/dV map of a different sample preparation with a deposition time of 2:30 min. (c) A third preparation where the deposition time was increased to 3:00 min. All the other relevant preparation parameters, i.e. substrate temperature, HTF power and deposition flux, were comparable for each preparation. In a) and b), the curved appearance of the step edges is a result of thermal drift during the scans and the dark diagonal line over a few terraces in c) is related to a bit error line caused by the Nanonis software. (STM constant-current in variable temperature STM [81]: Cr-tip, (a) $T = 34$ K, $V = 100$ mV, $I = 1$ nA (b),(c) $T = 47$ K, $V = 10$ mV, $I = 1$ nA.)

as surface temperature (transfer time between the last HTF and deposition), HTF power, and deposition flux, were comparable.

The reason for the enlarged area of reconstruction may be related to the fact that various defects are adsorbed preferably on the Ta surface. By closing the monolayer, the adsorbates enter the Fe monolayer and can create different reconstructions. A similar behavior for the previously discussed sample system of Mn/W(001) was observed, which is why in Section 3.2, only sub-monolayer preparations were chosen. For Ta and W, it is well known that the residual hydrogen inside the UHV chambers adsorbs on the surface, characterized by elongated patterns along the high symmetry directions of the sample surface, as shown in Fig. 4.2(c). This can likely lead to the formation of compounds with the remaining oxygen contaminations, resulting in the discussed superstructures.

In conclusion, to maximize the pseudomorphic growth of Fe, it is decisive to remove oxygen reconstructions on the bare Ta surface as much as possible with HTFs above $2000°\mathrm{C}$. Further, the transfer time between the last HTF and the Fe deposition is crucial in these preparation procedures. A reduction of the transfer time leads to a higher surface temperature during the Fe deposition, and it also lowers the time for potential contamination of the uncovered surface. In the used setup, a transfer time of four to six minutes resulted in sample preparations with the highest surface quality. Finally, to avoid reconstructed Fe-layers, it is necessary to ensure that the Fe coverage does not exceed one monolayer. With this recipe, a clean preparation of Fe monolayers on Ta(110) is reproducibly achievable, providing the opportunity to investigate the magnetic properties of the pseudomorphic Fe monolayer, as discussed in the next chapter.

5 Magnetic phases of Fe/Ta(110) and their behavior in magnetic field

Finding the preparation recipe that results in a clean sample surface can be time-consuming. Consequently, measurements on samples with less than optimal surface quality are inevitable. For one monolayer of Fe on Ta(110), two characteristic sample preparations lead to an interesting change in the apparent magnetic state, depending on the morphology and the coverage of the pseudomorphic Fe layer. The reasons for the change of the magnetic ground state, as well as the states themselves, will be discussed in this chapter.

As is usual for the magnetic characterization of a sample system, a magnetic field perpendicular to the sample surface was used to gain more insights into the nature of the apparent magnetic texture. During these investigations, the formation of elongated skyrmions, for the first time in a pseudomorphic layer and purely driven by the lattice symmetry, is obtained. Finally, after identifying the magnetic ground states of the samples with different morphologies, the topological charge of the different spin configurations will be examined.

5.1 Spin spiral phase of Fe/Ta(110)

In this section, the focus will be on samples with a morphology characterized by a few larger vacancy islands and multiple tiny vacancy islands (see black regions in Fig. 5.1). The magnetic ground state observed by SP-STM measurements in such a sample system is a striped pattern with a period of approximately 6 nm throughout the pseudomorphic layer of Fe, except for a few tiny reconstructed patches (see red ellipse in Fig. 5.1). The reconstruction can be assigned to the second type of the established reconstructions in the Fe monolayer on Ta(110) (see Fig. 4.3). Since one of the predicted ground states from the calculations in [117] was a spin spiral of 5.98 nm for the pseudomorphic Fe monolayer, a comparison with the experimentally observed period of the striped pattern yields good agreement. The measured period slightly varies due to confinement effects at the vacancy edges, which result in broadened features in the FFT map of the measured data (see inset in Fig. 5.1). Due to the twofold symmetry of the crystal lattice, only one rotational domain, in contrast to the two rotational domains present in the Mn/W(001) system, is observable. In the vicinity of the reconstructed patches, a clear distortion from the actual spin spiral propagation direction along $[1\bar{1}0]$ is identified. The spin spiral stripes merge in these regions, and the area of the spin component related to the bright contrast in the image is maximized around these regions. Due to the influence on the spin spi-

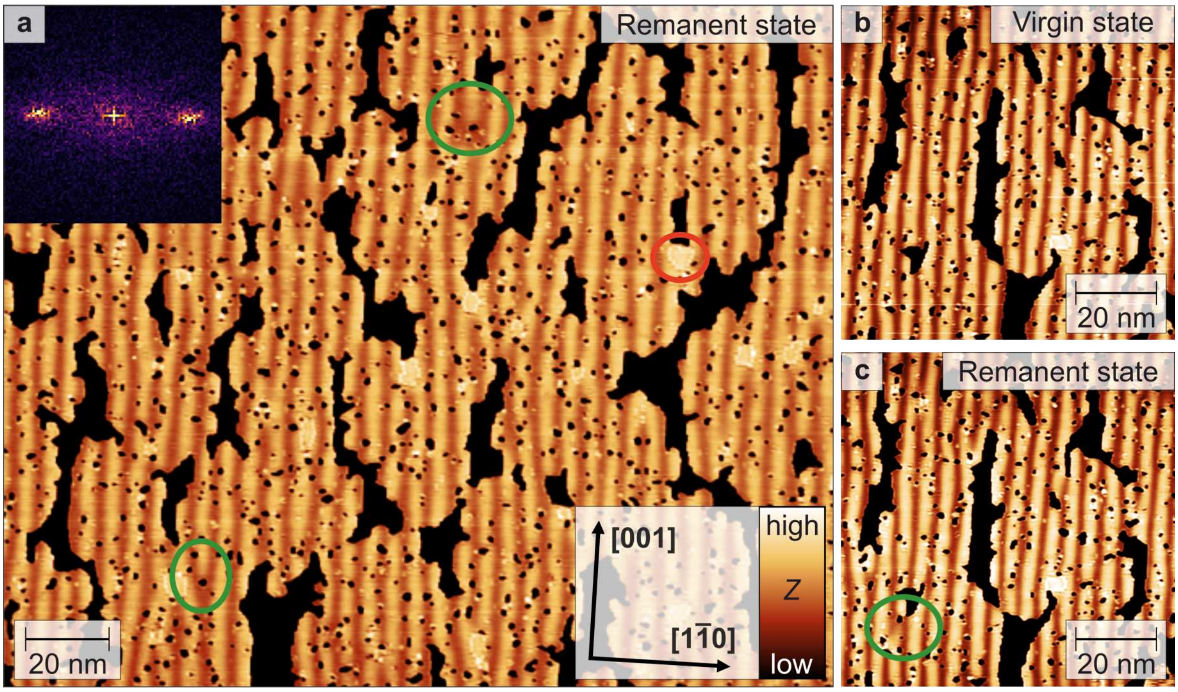

Figure 5.1: Pure spin spiral phase in virgin and remanent state. (a) 0.85 monolayers of Fe on Ta(110) with vacancy islands (black regions), small reconstructed patches (red ellipse) and spin spiral branches (green ellipses). The inset shows a Fast Fourier Transformation of the image. (b) A closer view on a different sample area in the virgin state. (c) The same scan area as in (b) with an emerged spin spiral branch marked by a green ellipse. (SP-STM constant-current: Cr-tip, $T = 4.2$ K (a) $V = -40$ mV, $I = 1$ nA (b),(c) $V = -30$ mV, $I = 1$ nA.)

ral propagation direction, a magnetic nature of these reconstructed patches is likely, and they are most probably FM because of the measured uniform signal within these regions.

Additionally, a preferred orientation of the elongated vacancy islands along the $[001]$-direction is observable in this sample preparation, which leads to more step edges along $[001]$ than in all the other directions. Since the overview image in Fig. 5.1(a) shows the remanent state at 0 T of the sample after applying an out-of-plane magnetic field of 6 T, the difference between the virgin and remanent states of the sample in Figs. 5.1(b),(c) is depicted as well. In (b) and (c), the same sample area was measured at 0 T, and in between, a magnetic field of 6 T was applied. Both images are comparable, but the emergence of some spiral branches can be observed (see green ellipses in Figs. 5.1(a),(c)). Referring to the previous chapter about the sample system of Mn/W(001), these spiral branches also appear in the established T-wall configuration, where each spiral end can be imagined as half a skyrmion carrying a topological charge of 0.5.

The STM measurements presented so far were obtained by using a magnetic tip resulting in a signal, which scales with the cosine of the angle enclosed by tip and sample magnetization, i.e., it relates directly to the magnetic periodicity (see Sec. 2.6). When a non-magnetic tip is used, the NCMR or TAMR effect can be dominant and lead to a signal that reflects the magnetic periodicity indirectly (see Sec. 2.6). As already mentioned in Chapter 2, both effects are summarized as EMR in the following.

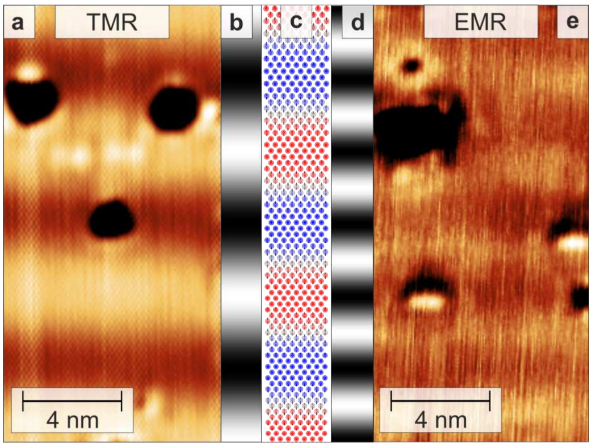

Figure 5.2: Comparison between TMR and EMR contrast of a cycloidal spin spiral. (a) SP-STM measurement obtained with a tip, where the TMR effect is dominating. (b) Expected SP-STM signal for a spin spiral due to the TMR effect. (c) Sketch of a homogeneous spin spiral; red and blue indicate up and down magnetization directions, respectively. (d) Expected signal for a spin spiral using a non-magnetic tip due to EMR effects. (e) STM image obtained using a non-magnetic tip, revealing a periodic pattern with roughly half of the spin spiral period compared to the measurement depicted in a). (Cr-tip, (a) SP-STM constant-current: $T = 4.2$ K, $V = -40$ mV, $I = 1$ nA (e) STM constant-current: $T = 1.3$ K, $V = -15$ mV, $I = 1$ nA.)

In Fig. 5.2(a) and (e), a comparison of measurements on two different spots of the sample with a magnetic (TMR) and a non-magnetic tip (EMR) is shown. In the case of the EMR effect, the period from the TMR image is roughly halved, even though the intensity is much lower than for the TMR effect. To maximize the EMR contrast, a comparatively low bias voltage ($V = 5$ mV) was used. In Fig. 5.2(c), a sketch of the established spin spiral texture is depicted with the expected contrast for a pure TMR-related signal in Fig. 5.2(b) or a pure EMR-related signal in Fig. 5.2(d), respectively.

In Fig. 5.2, the two extreme cases are shown where either the TMR or EMR is dominating, but the measured contrast can also be a mixture of both contributions.

In Fig. 5.3, a comparison of a SP-STM measurement obtained with a tip offering a symmetric contrast profile of the spin spiral is shown in (a), while a distorted spin spiral profile is shown in (b). The line profiles display the spin spiral period due to the TMR effect. As previously mentioned, the experiments cannot determine whether the NCMR or the TAMR is responsible for the observed contrast; however, both effects can be modeled as a cos^2-function in first approximation [92, 94]. Consequently, this dependency can also describe the EMR.

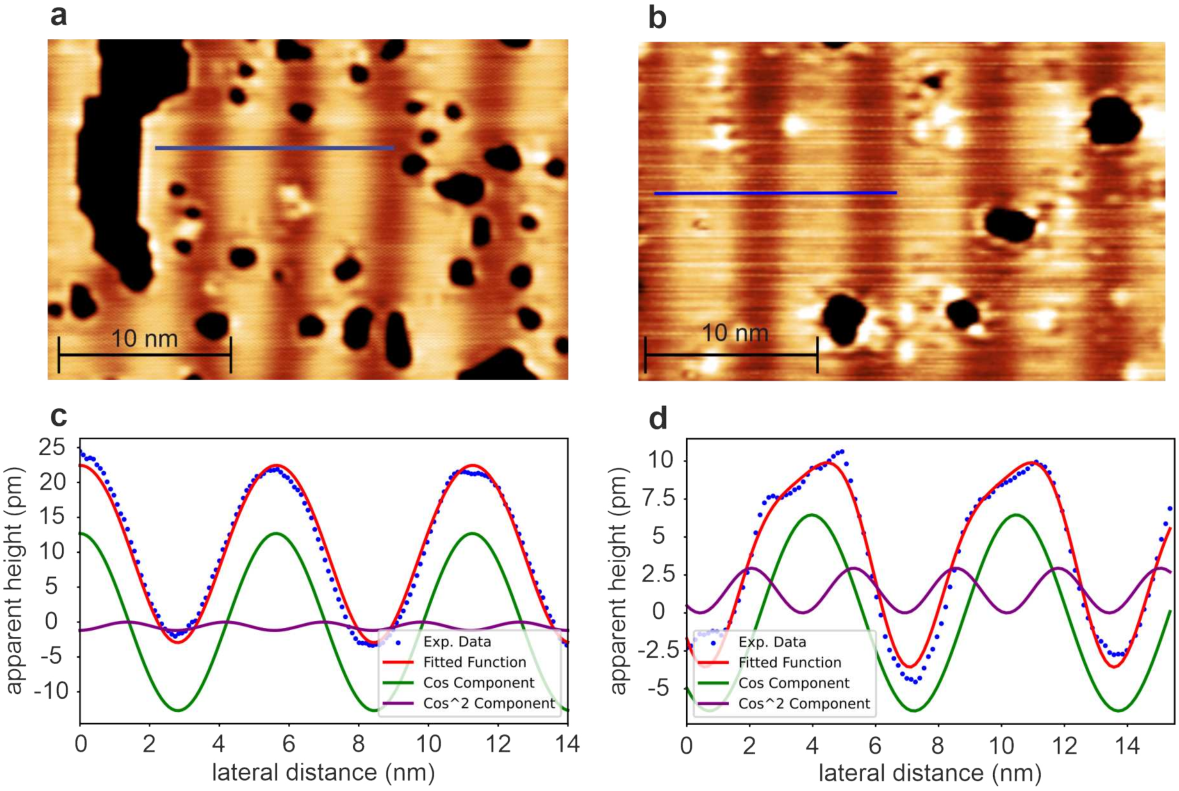

Figure 5.3: Spin spiral profiles with different ratios between TMR and EMR. (a) SP-STM constant-current image with a symmetric spin spiral contrast profile. (b) SP-STM constant-current image measured with a different tip and bias voltage compared to a). (c),(d) The blue dots represent data points corresponding to the line profile indicated by the blue line in (a) and (b), respectively. Also plotted are the fits (red line) with the single contributions of the TMR (green line) and EMR (purple line) effect represented by a cos or cos^2 function, respectively. (Cr-tip, (a) $T = 4.2$ K, $I = 1$ nA, $V = -40$ mV; (b) $T = 1.3$ K, $I = 1$ nA, $V = 4$ mV).

In Fig. 5.3(c), a symmetric peak shape in the line profile is observed, leading to the conclusion of a negligible influence of the EMR effect in this measurement. To quantify the contributions of TMR and EMR in this spin spiral profile, a fit considering a cosine contribution for the TMR (green line) and a cos^2-function for the EMR (purple line) related contributions to the signal was performed. The red curve shows the fitted function and accurately reproduces the experimentally measured profile. The individual components indicate a dominating TMR contribution in this measurement, as already speculated due to the apparent symmetric spin spiral profile.

In Fig. 5.3(d), a clear asymmetric peak shape in the line profile is present, leading to the conclusion of a non-negligible influence of the EMR effect in this measurement. The same fit to characterize the contributions of TMR and EMR was applied. The individual components of the fit still indicate a dominating TMR contribution, however, the ratio of the amplitudes between EMR and TMR has significantly changed. Furthermore, the tip magnetization appears to be canted due to the present phase shift between the EMR and TMR contributions. The resulting fitted function reproduces the experimentally measured profile and confirms a significant EMR effect in the STM data.

Since the predicted spin spiral in the monolayer of Fe on Ta(110) was confirmed, the realization of a sample system offering the opportunity to investigate the interaction between non-collinear spin textures on an s-wave superconductor has been demonstrated. Before discussing the superconducting properties of the sample system, a sample with a slightly different morphology, resulting in a distinguishable magnetic ground state, will be addressed in the following.

5.2 Coexistent magnetic phases of Fe/Ta(110)

A monolayer of Fe on Ta(110) can be magnetically more complex than the last section suggests. The focus will now be on samples with a slightly different morphology as the previously discussed samples. In Fig. 5.4(a), a constant-current SP-STM image of 0.85 monolayers of Fe on Ta(110) is shown. The Fe monolayer still exhibits vacancies, however, the areas of vacancy-free regions are larger compared to the sample discussed in Sec. 5.1. A comparison between both morphologies (I),(II) is shown in the center of Fig. 5.4, where the upper panel corresponds to the sample discussed in the previous section and the lower panel corresponds to the area marked by a black rectangle in Fig. 5.4(a). In contrast to the morphology (I), narrow atomic step edges of the Ta sample are observable in this location of the sample. The differential tunneling conductance map measured together with the topography of Fig. 5.4(a) is presented in Fig. 5.4(b). Areas with a stripe pattern corresponding to the established spin spiral state and, interestingly, regions exhibiting a uniform signal with two distinct contrast levels are observable. Two uniform contrast levels are a characteristic feature of ferromagnetically polarized areas with anti-parallel magnetized domains. The spin spiral state acts as a domain wall either between

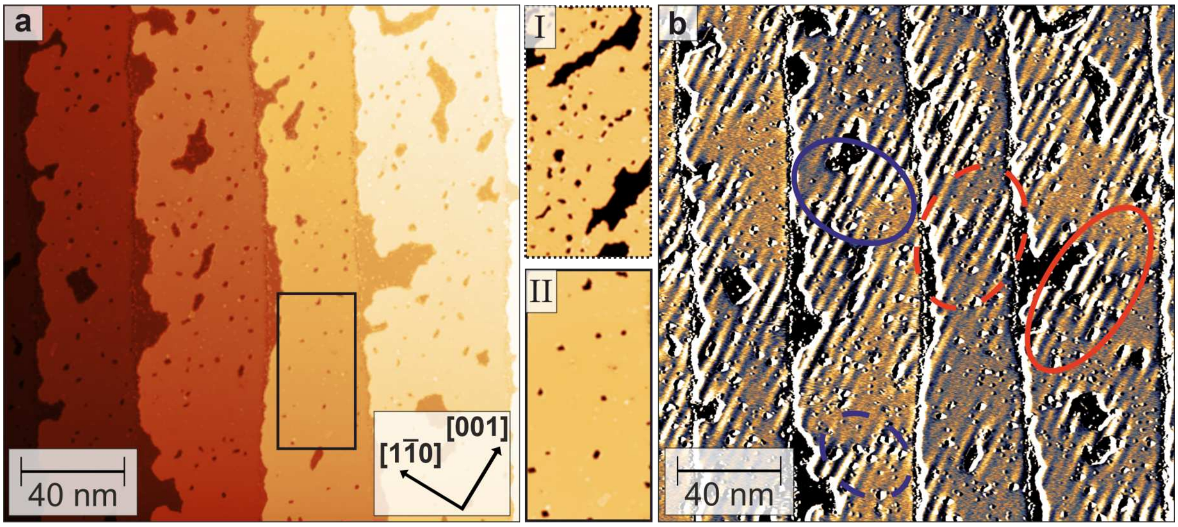

Figure 5.4: Second type of morphology with a magnetic ground state exhibiting additional contrast levels. (a) Topography STM-image of a second type of morphology with larger extended areas of Fe and narrow atomic step edges. (I),(II) A comparison between the two morphologies discussed in this chapter, where I is an additional measurement of a characteristic sample area of the sample preparation presented in Fig. 5.1 and II is the area within the black rectangle from (a). (b) Differential tunneling conductance map corresponding to the topography in (a) with two uniform signal levels and spin spirals as boundaries between these areas. Red ellipses mark the first identified orientation of domain walls and the blue ellipses mark the second one, where the dashed line or continuous line represents a trivial domain wall configuration or a non-trivial domain wall configuration, respectively. (SP-STM constant-current: Cr-tip, $T = 4.2$ K, $I = 1$ nA (a),(b),(II) $V = -500$ mV (I) $V = -100$ mV.)

areas with the same (dashed ellipses) or two distinguishable (continuous ellipses) uniform contrast levels. Additionally, there are at least two different domain wall orientations: one where the FM stripes along $[001]$ are parallel to the domain wall orientation (blue ellipses), and a second type where the orientation is perpendicular to $[001]$ (red ellipses).

The spin spiral regions prefer to nucleate in the vicinity of the vacancy islands of the Fe film. The orientation of vacancy edges seems to play a role in how effectively the spin spiral can be stabilized. In the area without a significant number of Fe step edges, the uniform signal extends the most. Notably, the elongated vacancy islands with long edges along the $[001]$-direction might be one of the main reasons why, in morphology (I), exclusively the spin spiral state is observable. In the vicinity of the vacancy islands, the coordination number of the Fe atoms at the edge is reduced, which leads to a different energy landscape. For example, the magnetic anisotropy can be changed, and the dipole interaction is reduced, as observed in the case of a Fe double layer on W(110) [121], where in more extended Fe films, the dipole interaction reduces the effect of the out-of-plane magnetic anisotropy below a critical value, allowing an inhomogeneous spin spiral to develop. In Fe/Ta(110), a similar effect may occur; when the monolayer of Fe is interrupted, the dipole interaction is reduced, and this can initiate a tilt of the spins away from the easy axis. A detailed discussion about this magnetic state will be part of the next section, where the magnetic properties of both types of sample morphology are analyzed further.

5.3 Magnetic field dependency

Pure spin spiral state

After introducing the different magnetic states for the distinguishable morphologies of the sample system at zero field, the field dependence data is used to gain more insights into both types of sample morphology. The focus will first be placed on the morphology, where the pure spin spiral state is the magnetic ground state.

In Fig. 5.5(a), the identical measurement from Fig. 5.1 is presented again, together with a zoom-in (b) into the area marked by a white square. The same areas were measured again at 2.4 T applied perpendicular to the sample surface, and the results are depicted in Figs. 5.5(c),(d). As in one monolayer of Mn on W(001), the spin spiral stripes break into small fragments. However, this time, a uniform signal remains, which would be expected for skyrmion formation within a ferromagnetic background with magnetization in the skyrmion core antiparallel to the applied magnetic field. The bright features favor appearing in the vicinity of the vacancy islands, a behavior also observed in Ref. [22], where the skyrmions pin to defect sites and are robust even in remanence. One experiment to validate that these features are skyrmions is to measure at both magnetic field polarities. In the case of a hard magnetized tip, meaning a tip that is not sensitive to an external magnetic field, the expected behavior would be a switch in contrast between the skyrmions and the ferromagnetic background at different polarities.

A series realizing this kind of experiment is presented in Fig. 5.6, where a constant spin polarization of the tip during the measurements is assumed. The color scale used for all measurements is the same for better comparability. The spin spiral contrast is clearly visible in the zero-field data in Fig. 5.6(a), albeit with a slightly worse signal-to-noise ratio compared to the previous measurement series. The reason for this change was the modification of the tip apex to obtain a magnetically hard tip, which led to a slightly less stable junction and a reduced spin polarization of the tip apex. By applying a magnetic field of 2.4 T, the same elongated, bright features ap-

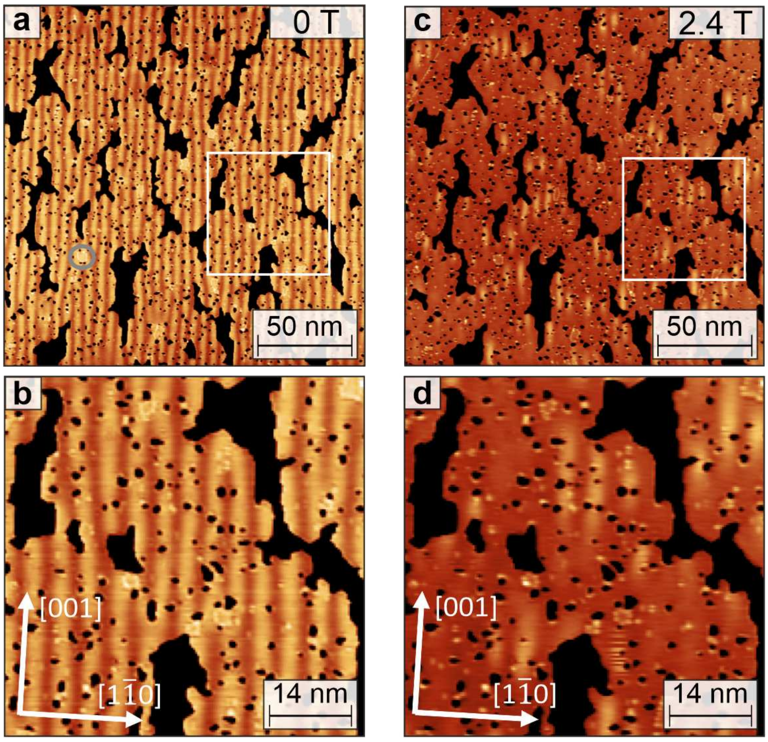

Figure 5.5: Field dependence of the pure spin spiral phase. (a) The same SP-STM measurement as in Fig. 5.1(a). (b) A zoomed-in view of the area within the white square in the SP-STM image from (a). (c) The scanned area from (a) under an applied out-of-plane magnetic field of 2.4 T. (d) A zoomed-in view of the area within the white square in the SP-STM image from (c). (SP-STM constant-current: Cr-tip, (a),(b) $T = 4.2$ K, $V = -40$ mV, $I = 1$ nA.)

pear (see Figs. 5.6(b),(c)). When the polarity is changed, the bright features switch to dark elongated features (see Figs. 5.6(d),(e)), as expected for skyrmions measured with a magnetically hard tip. Furthermore, the FM background also switches from dark in positive fields to bright in negative fields. Back at 0 T, the spin spiral stripes reappear at similar locations as before (see Fig. 5.6(f)), which is another indication that confinement effects are playing a role in stabilizing a certain phase of the spin spiral. Furthermore, this observation supports the assumption of a constant spin polarization of the tip during these measurements.

The noticeable feature of the individual skyrmions here is their distorted shape compared to most other works on interface-induced skyrmions. In another study, the shape of the individual skyrmions has been influenced by uniaxial strain, leading to their distortion [122]. In the Fe monolayer on Ta(110), the two-fold symmetry of the crystal lattice stabilizes the elongated skyrmions along the $[001]$-direction. Notably, the form of these elongated skyrmions means that the topological charge is split, with each end of the skyrmion exhibiting a topological charge of $Q = 0.5$, which

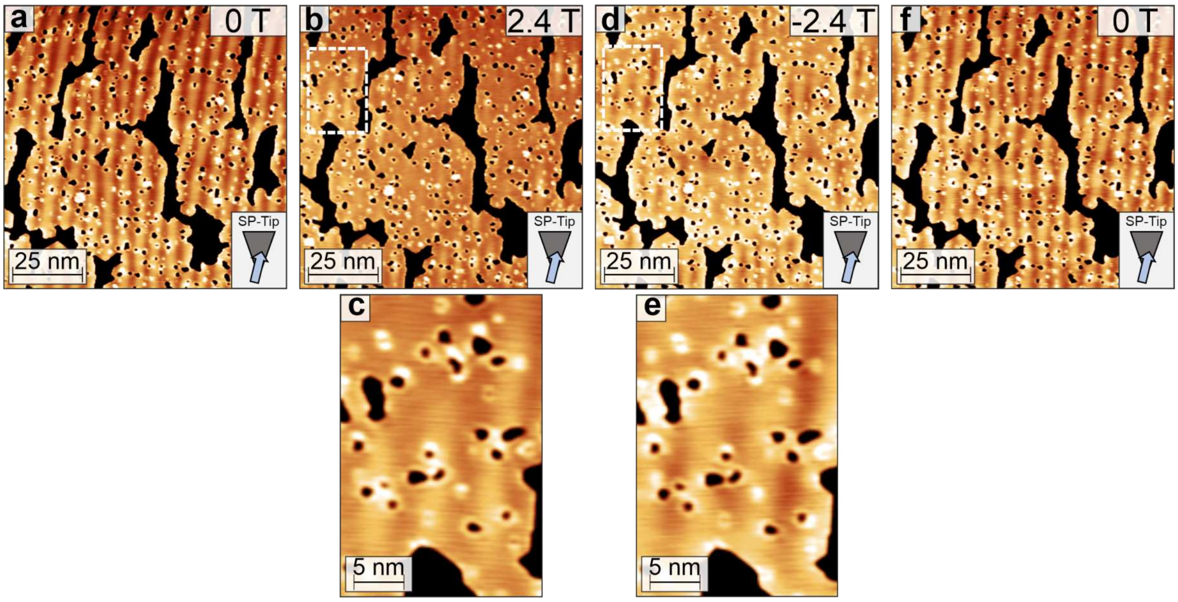

Figure 5.6: Field inversion measurements of the pure spin spiral state with a hard magnetized tip. (a) Initial SP-STM measurement of the unaffected spin spiral state. (b) Measurement of the scan area in (a) shifted by a few nm with an applied field of $+2.4$ T. (c) Zoom-in of the area within the white rectangle in (b) shows three elongated bright features. (d) The same location measured at -2.4 T. (e) Zoom-in of the same region depicted in (c) showing three elongated dark features. (f) Measurement of the identical scan area as before after removing the field, resulting in the pure spin spiral state again. (SP-STM constant-current: Cr-tip, $T = 4.2$ K, $V = 100$ mV, $I = 1$ nA).

could be utilized in the field of spintronics.

Mixed ferromagnet and spin spiral state

After presenting the field dependence results of morphology (I), the focus shifts to the magnetic ground state of morphology (II). Since a FM state is expected for the regions with uniform signal in Fig. 5.4, an out-of-plane field should be sufficient to identify which type of FM alignment the regions provide. In the case of out-of-plane magnetism, one domain is already aligned with the external magnetic field and the resulting contrast remains constant if the texture is measured with a magnetically hard tip. The oppositely magnetized domains in zero field will change and align with the magnetic field leading to a contrast change in the measurement. If the domains are magnetized in the plane of the sample surface, both contrasts are changing by increasing the magnetic field.

In Fig. 5.7(a), a series of SP-STM measurements at different magnetic field values, performed at the same sample position with the same magnetic tip, are pre-

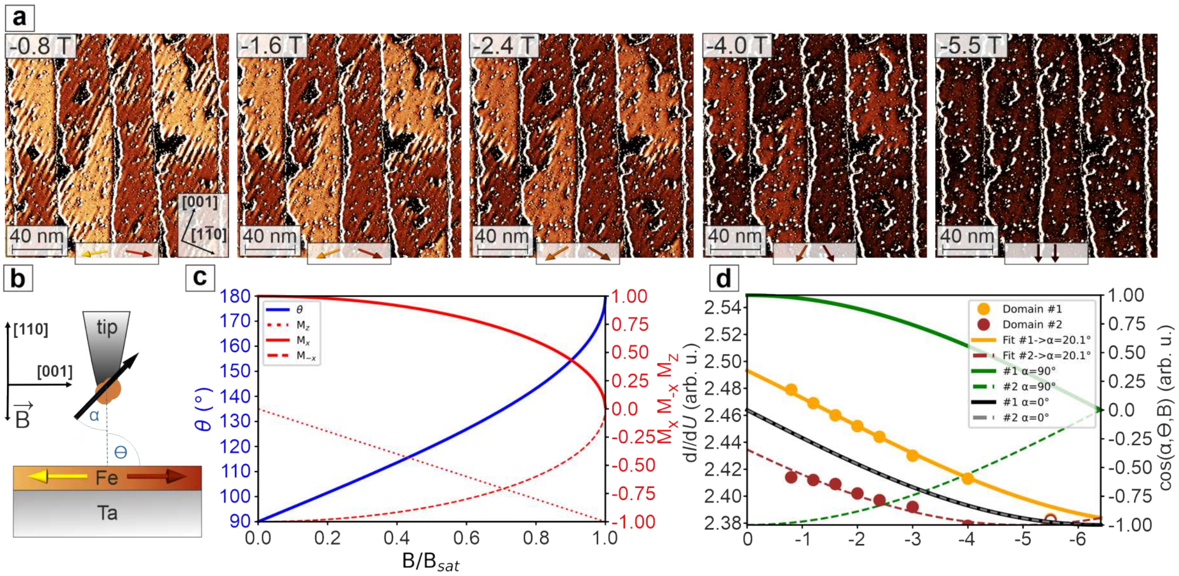

Figure 5.7: Out-of-plane field dependence of ferromagnetic in-plane domains. (a) The dI/dV-channel of SP-STM measurements exhibiting bright and dark domains with flat corrugation, as well as regions with spin spiral between them, measured at several magnetic field values, ranging from -0.8 T to -5.5 T. (b) Schematic representation of the presumed observations, depicting the angle α between the out-of-plane direction and the magnetization direction of the tip, along with an atomic layer of Fe with an angle θ between the domains and the out-of-plane direction. (c) The plot shows the analytical description of the out-of-plane field dependence of an in-plane domain for the different components θ, M_z (cos(θ)) and $M_{\pm x}$, where θ is ranging from $90°$ to $180°$, with $90°$ indicating an upward direction. (d) The data points of the averaged dI/dV-signal of a flat area on both in-plane domains are fitted with a+b*cos(90+c$*B\pm\alpha$). This formula represents the projection of θ, which varies with the magnetic field B, onto the optimized angle α of the SP-tip, assumed to be constant with increasing magnetic field. In addition to the optimized case, hypothetical cases for $\alpha = 0°$ and $\alpha = 90°$ are also depicted. (SP-STM constant-current: Cr-tip, $T = 4.2$ K, $I = 1$ nA, $V = -0.5$ V).

sented. The color code in (a) represents the spatially-resolved differential tunneling conductance, and the color scale is identical in all images. Areas with spin spiral stripes and two different uniform contrast levels at $B = -0.8$ T normal to the surface can be identified. As the magnetic field increases, the area of spin spiral stripes decreases and minimizes at roughly -2.4 T, where the width of the area between the two domains in the center of the image is separated only by a single dark stripe. The amplitude of the spin spiral contrast remains constant with the applied magnetic field, indicating that the tip magnetization $\mathbf{m}_{\mathrm{T}}$ is not influenced by the applied magnetic field. The intensity of all homogeneous areas decreases by increasing the magnetic field and saturates at roughly $B = -5.5$ T. It can be concluded that the extended areas are fully aligned with the out-of-plane magnetic field, as sketched with two downward-pointing arrows in the inset of the last panel in Fig. 5.7(a). Summarizing, the observed behavior in an external out-of-plane magnetic field can be attributed to oppositely magnetized in-plane domains at zero field, likely magnetized along the easy axis $[001]$ as predicted by DFT calculations in Ref. [117].

A sketch of the experimental setup with a canted tip and in-plane sample magnetization is depicted in Fig. 5.7(b). The expected behavior of in-plane domains in an out-of-plane magnetic field is shown in Fig. 5.7(c). The polar angle Θ changes from in-plane $(90°)$ to out-of-plane $(180°)$ at B_{sat}. The m_z component changes linearly from 0 to -1, and the opposite in-plane components $m_{\pm x}$ approach 0. To further understand the experimental observations, the projection on different tip magnetizations together with the dI/dV-signal measured on both domains are presented in Fig. 5.7(d). The calculated data for an in-plane (green curves) or an out-of-plane (gray and black curves) magnetized tip on oppositely magnetized in-plane domains deviates from the experimental magnetic field-dependent dI/dV data (brown and yellow data points). According to this model, a tip magnetization direction with $\Theta = 20°$ is obtained, which shows good agreement with the experiment. Consequently, this model confirms the presence of FM in-plane domains in one monolayer of Fe on Ta(110) as the magnetic ground state for samples with morphology (II).

After the analysis of the areas with uniform SP-STM signal, the focus now shifts to the boundaries between the in-plane domains, namely the spin spiral domain walls. For better visualization of the spin textures, a color code is defined to include each spin orientation (see Fig. 5.8(a)), where the in-plane components are colorized and the out-of-plane components are represented by black and white. Additionally, an arrow representing a possible spin orientation of the tip with $\Theta = 20°$, as suggested in Fig. 5.7, is shown. In Fig. 5.4, the types of domain walls observed in the experiment were already introduced, but it was a simplified image only allowing two orientations of domain walls along $[001]$ and $[1\bar{1}0]$. In fact, the domain walls can occur in all orientations possible when connecting two in-plane domains, not just in two discrete directions. One possible way to illustrate this is to think of it as a circular domain wall around one in-plane domain surrounded by an oppositely magnetized in-plane domain, or in short, a bubble domain (see Fig. 5.8(b)). Here, all different orientations that are possible for the connection between both in-plane domains can be realized.

Analyzing the domain walls more closely in Figs. 5.8(c)-(e), a mixture of different domain wall orientations resulting in irregularly shaped domain walls with varying widths can be seen. To visualize the spin directions of the FM domains and the spin spiral, a tentative model is introduced in the sketches close to each SP-STM image,

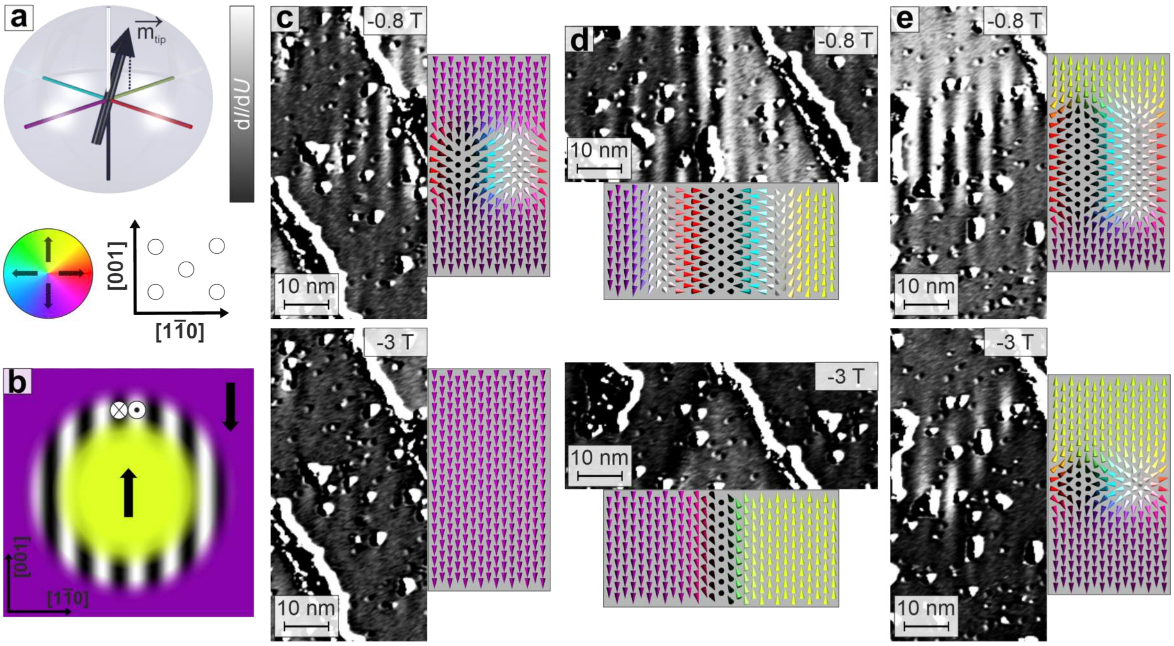

Figure 5.8: A spin spiral as a domain wall between ferromagnetic in-plane domains. (a) A sketch of the chosen color coding for each magnetization direction with an arrow representing a possible tip magnetization with $\Theta = 20°$, as suggested in Fig. 5.7. (b) A simplified visualization of all possible domain wall orientations by connecting two FM in-plane areas via a round spin spiral domain wall. (c) Zoom-in into a region from Fig. 5.7(a) in an area where the wall has two domains with the same magnetization direction around it. The lower panel shows the same area measured at $B = -3$ T. (d) Another zoom-in into a region from Fig. 5.7(a) with a spin spiral area between two oppositely magnetized domains, where the propagation direction of the spin spiral is mostly orthogonal to the domain wall direction. The lower panel shows the same area as in the upper panel measured at $B = -3$ T. (e) Shows another zoom-in of the image in Fig. 5.7(a) into a type of domain wall, where the propagation direction of the spin spiral is mostly parallel to the domain wall direction. The lower panel shows the same area as in the upper panel measured at $B = -3$ T. Each panel of the figure has an illustration that depicts the spin configuration of a certain domain wall with colorized in-plane directions and a gray color scale for the out-of-plane spin components. (SP-STM constant-current: Cr-tip, $T = 4.2$ K, $I = 1$ nA, $V = -0.5$ V).

presenting a possible spin configuration of the measured domain wall. By increasing the magnetic field, the domain wall, where the spin spiral appears between the same magnetized domains, vanishes at $B = 3$ T (see Fig. 5.8(c)). Analyzing the spin spiral wall close to the $[001]$-direction (Fig. 5.8(d)) from left to right, it can be seen that the spins propagate in a helical rotation to connect smoothly to the cycloidal spin spiral. This also occurs on the other side of the wall to connect the oppositely magnetized domain. In a higher out-of-plane magnetic field, the number of spin spiral periods is reduced, and in the limit of a large magnetic field, the wall is expected to be a helical 180° domain wall, as shown in the bottom panel of Fig. 5.8(d).

A different behavior occurs in the spin spiral wall roughly along $[1\bar{1}0]$, as shown in Fig. 5.8(e). There, the magnetization within the wall can be described by a conical rotation with a conical angle changing from 0° (first in-plane domain) via 90° (center of the domain wall), i.e., a perfect cycloidal spin spiral, to 180° (second in-plane domain). In total, this domain wall consists of meron-antimeron pairs connected by a shared in-plane area in between, allowing for a smooth transition in the $[1\bar{1}0]$-direction.

Since a meron is topologically non-trivial and has a topological charge of 0.5 and the polarity is changing from meron to antimeron along the domain wall direction, a finite Q for this type of domain wall is expected. To identify the topological properties of the domain walls, Q was calculated following the described method from Ref. [69, 70] and the resulting topological charge density was plotted in the background of the different spin configurations (see Fig. 5.9).

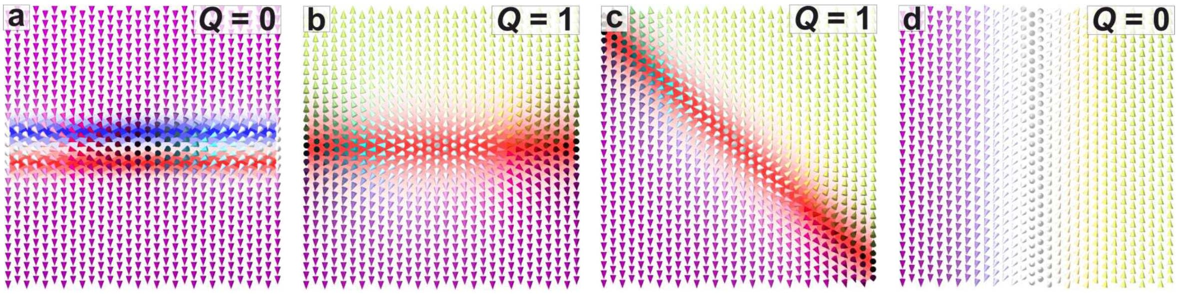

Figure 5.9: Topological charge of the spin spiral domain walls. The types of domain walls are depicted together with the calculated normalized topological charge density in the background, shown in (a) for the trivial domain wall formation, in (b) for the non-trivial configuration of the domain wall along the $[1\bar{1}0]$-direction. In (c), a mixture of both directions with the resulting topological charge is visible and in (d), the domain wall along the $[001]$-direction is presented. The color scale represents the topological charge density, ranging from red (highest topological charge density) to blue (lowest topological charge density) with white indicating zero topological charge. For all the presented topological charge density maps, the color scale values are constant.

Considering both cases, where the domain wall along $[1\bar{1}0]$ is either between magnetized domains of the same orientation or anti-parallel magnetized domains, two different results for Q are obtained. In the trivial case (Fig. 5.9(a)), where the spins undergo a 90° rotation followed by a rotation back, a finite Q with different signs results in a vanishing net Q, making this wall topologically trivial. This observation aligns with the lower required magnetic field to unwind this type of domain wall (see Fig. 5.8(c)).

The second case (see Fig. 5.9(b)) exhibits a topological charge density with only one sign in the center of the domain wall, contributing to a net Q of 1 per meron-antimeron pair. In contrast to the trivial domain wall configuration, this net Q enhances the stability in an applied magnetic field (Fig. 5.8(e)), albeit, the robustness of the domain wall configuration is not solely determined by the topological charge. The domain wall configuration that is off the high symmetry directions (see Fig. 5.9(c)) offers again a finite topological charge of $Q = 1$ per meron-antimeron pair. Since the color scale is the same in each image, it can be concluded that the solid angle of the spins involved in each wall structure is well comparable between the different wall types, as the red tone is well comparable in all images.

Finally, for the domain walls oriented along $[001]$, a net topological charge of $Q = 0$ is obtained, as for the trivial domain walls. However, this Bloch-like rotation is also stable against an out-of-plane magnetic field (see Fig. 5.8(d)). This stability could be attributed to the alignment of the dark stripe, which is likely parallel to the applied magnetic field, with both domains approaching this orientation to gain Zeeman energy. In that case, the domain wall has already reached the energetically favorable orientation parallel to the applied magnetic field and with a minimized domain wall width.

As previously suggested, the illustration of all possible domain wall orientations can be realized in the view of a bubble domain surrounded by a circular domain wall characterized by a cycloidal spin spiral. Although such a domain configuration was not found in the experiments, the topological charge of such a spin configuration was analyzed. To set up such a spin configuration, the Monte Crystal software by J. Hagemeister [64] was used, combined with a Mathematica code [69], which was also used for the calculation of the topological charge. The results are presented in Fig. 5.10 and suggest that the net topological charge is indeed zero by adding up the oppositely charged domain wall regions at the top and at the bottom of the bubble domain. For the side areas of the bubble the topological charge is zero as expected from the previous results of the domain walls oriented along $[001]$. In the transition between both areas the topological charge density fades out for a smooth transition from zero charge density to a finite topological charge density.

Analogy to cross-tie walls

The meron-antimeron domain wall shows, besides its topological properties, an interesting similarity to one of the most famous and best known domain wall structures

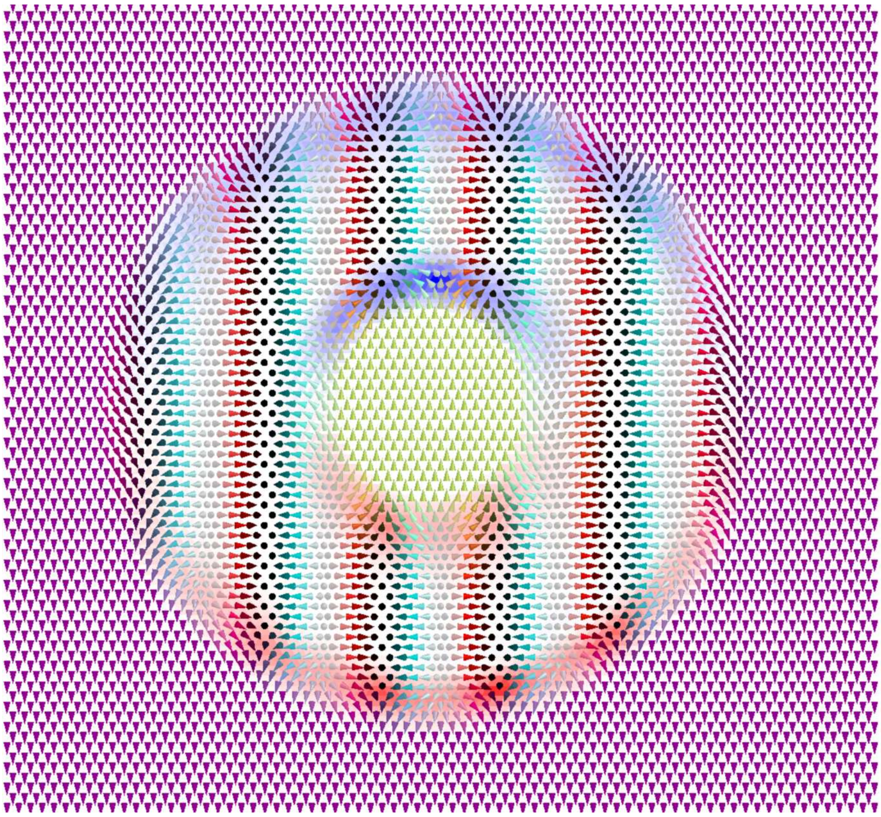

Figure 5.10: Topological charge of a bubble domain. A bubble domain wall configured with the Monte Crystal software by J. Hagemeister [64] and a Mathematica code by A. Kubetzka [69]. The spin configuration was also a few simulation steps relaxed with the converger function of Monte Crystal by choosing arbitrary parameters to obtain smoother transitions between the fixed in-plane domains and the relaxed spin spiral configuration.

in solid-state physics, namely the cross-tie domain walls in thin films. The first observation of this kind of wall was made by Huber $et\ al.$ [123] back in 1958, where they investigated thin films of Permalloy. This was followed by countless other works, e. g., by Middelhoek [124] and Wiese $et\ al.$ [125].

In contrast to a Néel or Bloch wall, the cross-tie domain wall is a two-dimensional spin rotation with an alternating vortex and antivortex structure. It mostly acts as an intermediate state between Néel-like domain walls in ultrathin films and Bloch-like domain walls in thin films or bulk systems. The energy landscape is changed by increasing the film thickness so that the cross-tie wall becomes energetically favorable by minimizing the emerging dipole energy of the wall [126]. In Figs. 5.11(a),(b), the same panels from Fig. 5.8 are shown, and in Fig. 5.11(c), a sketch where the spin orientations of the measured domain wall orientation are presented. Clear similarities to the wall configuration of the cross-tie walls from Wiese $et\ al.$ pre-

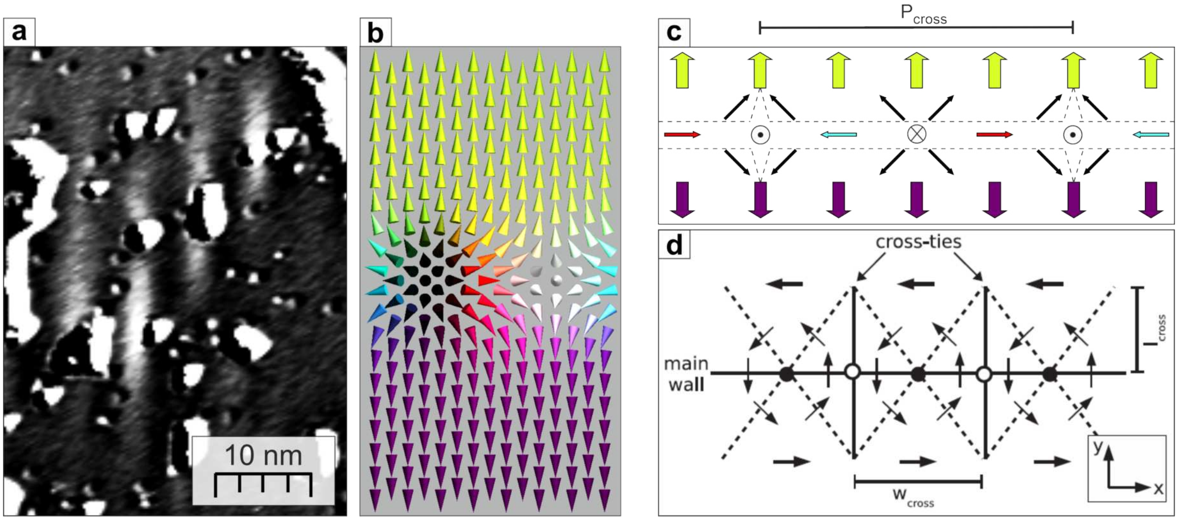

Figure 5.11: Analogy to cross tie domain walls. (a),(b) Same panels from Fig. 5.8. (c) A rough sketch of the domain wall with orientation along $[1\bar{1}0]$ with hypothetical cross-ties. (d) A drawing of the published data from [125], where the measured cross-tie wall is presented.

sented in Fig. 5.11(d) [125] can be seen. The major difference is a 90° rotation of all spins around the z-axis, which connects the Néel-like meron-antimeron wall to the Bloch-like nature for the domain wall configuration in the work of Wiese $et\ al.$. Since the dipole energy is expected to be much smaller compared to thin films or bulk systems, the characteristic cross ties are not visible in the measurements of the meron-antimeron domain wall configuration. Further, the present DMI inside the meron-antimeron domain wall might avoid the formation of the typical asymmetry between the vortex and antivortex in the cross-tie walls.

5.4 Conclusion and Outlook

A monolayer of Fe on Ta(110) offers a variety of interesting magnetic configurations and a transition in the magnetic ground state by a change of the present morphology of the Fe monolayer. In the first type observed in the experiments, a comparable magnetic state to that of a monolayer of Mn on W(001) occurs, where a spin spiral is the magnetic ground state at zero field. At finite magnetic fields, the spin spiral breaks, and fragments of the spin spirals remain, resulting in elongated skyrmions at higher magnetic fields. In contrast to the previous sample system, here a magnetic field of roughly 5 T is sufficient to reach the FM state. Both the elongation of the skyrmions and the appearance of only one rotational domain demonstrate the strong coupling of the magnetism on the surface to the crystal lattice symmetry, as observed in Mn/W(001).

A more homogeneous morphology of the sample system leads to a distinguishable magnetism, where uniform signals, related to ferromagnetically in-plane polarized domains, with two contrast levels occur, and areas of spin spiral remain in between. It turns out that the spin spiral acts as a domain wall to provide a smooth connection for the transition from one in-plane domain to another. Different domain wall orientations can be identified without any sign of energetic preference at zero field. At finite magnetic fields, domain walls with a net topological charge of $Q = 0$ between the identical domains disappear. Domain walls with a finite Q or a Bloch-like rotation are robust up to a magnetic field normal to the surface of roughly 5 T.

Since, to the best of current knowledge, a meron-antimeron domain wall with finite topological charge was experimentally identified for the first time, the question arises how such a domain wall configuration could be used. A well-known example of a possible application is the work on domain wall racetrack memories by Parkin $et\ al.$ [79]. In that work, they showed how domain walls can be moved by an external magnetic field or via an applied current, allowing a readout mechanism to identify it as a zero or one for the presence or absence of a domain wall, respectively.

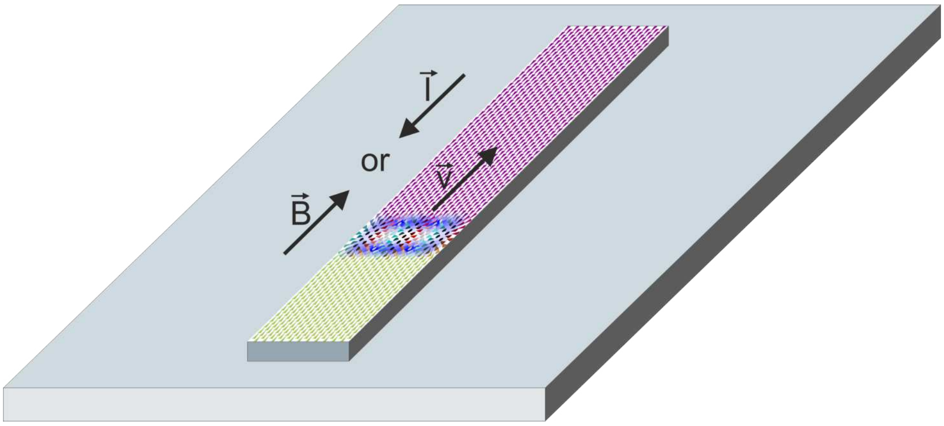

Figure 5.12: Meron-antimeron domain wall on a racetrack. A sketch of the established meron-antimeron domain wall configuration between two oppositely magnetized in-plane domains with possible magnetic field $\mathbf{B}$ or spin-polarized current $\mathbf{I}$ flow direction resulting in a movement of the domain wall along $\mathbf{v}$.

In Fig. 5.12, a racetrack schematic of the realized domain wall configuration is shown. Since the domain wall velocity is limited by the so-called Walker breakdown [127, 128], where the domain wall exhibits internal dynamics after exceeding a certain threshold of applied magnetic field or current density, the dynamics of reading and writing processes are also limited. These internal dynamics can lower the velocity or even cause the domain wall to move backward. This can be avoided by using domain walls of AFM layers, which are more stable and offer switching frequencies up to the THz regime [129], which is three orders of magnitude higher than for the FM domain wall. However, for this type of domain wall, the movement is more complex due to the compensated magnetic stray field in an AFM sample.

The presented meron-antimeron domain wall might act as an intermediate case where a magnetic field or a spin-polarized current can still be used to move the domain wall. Further, since the period of the spin spiral along the center of the domain wall is in the range of a few nanometers, the switching frequencies might be closer to the THz regime (antiferromagnet) than to the GHz regime (ferromagnet). In summary, the meron-antimeron domain wall could combine the advantages of both considered domain wall configurations and offer a fruitful platform for further investigation of the domain wall dynamics, either by STM studies or by calculations.

6 Non-collinear spin textures in interaction with superconductivity

All the presented results so far were obtained at temperatures where the Ta is in the normal conducting phase. This chapter is dedicated to the superconducting properties in interplay with the established non-collinear spin texture, namely, a cycloidal spin spiral.

In the field of superconductivity, the sub-field of topological superconductivity in bulk as well as in low-dimensional hybrid systems has become an active area of research in recent years [5, 23]. One approach involves establishing a 2D-MSH-system with a FM spin-lattice in the vicinity of an s-wave superconductor, as realized in Refs. [29, 120, 130, 131]. Such a system, combined with significant SOC at the surface, is expected to offer a topological non-trivial phase with chiral edge modes. Another approach involves AFM spin alignment in contact with a conventional superconductor, as realized in several works [34, 36, 38, 132, 133]. All these systems provide a fruitful platform for realizing novel topological phases of matter.

Since FM and AFM spin textures represent only a small subgroup of possible spin configurations, numerous other spin lattices, which were not covered in the mentioned works, exist. Several theoretical predictions regarding non-collinear [50, 134, 135] and non-coplanar [117, 136–138] spin textures in proximity to a superconductor have been discussed. However, the experimental investigation of these predictions has been lacking so far.

In this chapter, the experimental discovery of a non-collinear 2D-MSH-system of one monolayer of Fe on Ta(110) is described. The characterization of the properties of this non-collinear MSH-system is addressed, representing the first experimental investigation of the superconducting properties of non-collinear spin textures in a magnetic layer in proximity to an s-wave superconductor. A sketch of the realized non-collinear MSH-system is given in Fig. 6.1.

The experimental work is supported by tight binding calculations by Jasmin Bedow from the theory group of Prof. Dr. Dirk K. Morr from Chicago [68], which are presented in the following.

6.1 Characterization of Fe/Ta(110) in the superconducting state

This section introduces the superconducting properties of the clean Ta(110) substrate at 1.3 K. Further, the spectra of the tips mostly used for the measurements on Fe/Ta(110) in the superconducting phase are introduced.

So far, the results presented in this thesis were obtained at 4.2 K, which is close

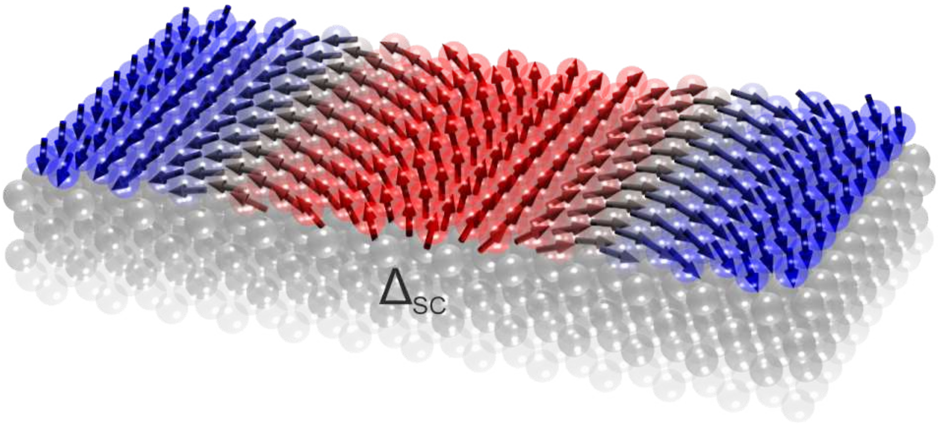

Figure 6.1: Sketch of the realized MSH model system. A perspective view on a schematic of the established cycloidal spin spiral in the vicinity of a superconductor with a superconducting gap of Δ_{SC}.

to the critical temperature of $T_{\text{C}} = 4.4$ K, but not sufficient to investigate the superconducting properties of the sample system. By cooling down the system further utilizing the Joule-Thomson effect, the temperature of the sample can be lowered to 1.3 K (see Sec. 2.2). An ideal tool to characterize the superconducting properties of Ta is STS, where spectroscopic measurements with high spatial resolution are obtained. Tunneling with a normal conducting Cr-tip leads to a gap in the dI/dV-signal around E_F (Fig. 6.2 *microtip 1*). This superconducting gap can be described by the Dynes function (see Sec. 1.2), which is based on BCS theory. The fitting curve (red line) in Fig. 6.2 is in good agreement with the experimentally obtained spectrum and offers a $\Delta_{\text{Sample}} = 0.62$ meV, which is close to the common value of $\Delta_{\text{Ta}} = 0.69$ meV as established in the literature. The additional spectra in Fig. 6.2 (*microtip 2* and *microtip 3*) deviate from the previously discussed curve. The coherence peaks are shifted to higher negative or positive energies for the coherence peaks at negative or positive bias voltages, respectively. This indicates that the tip is not in a normal conducting state. In the case of a Ta bulk tip on the Ta(110) surface, the coherence peaks would appear at energies $\pm 2\Delta_{\text{Ta}}$. Since the coherence peaks are at energies between $\pm\Delta_{\text{Ta}}$ and $\pm 2\Delta_{\text{Ta}}$, it can be assumed that a small cluster of Ta at the apex of the Cr-tip leads to such superconducting spectra.

By further modifying the tip apex in the areas of clean Ta, large Ta clusters can be picked up, resulting in superconducting gaps where the coherence peaks shift to an energy of approximately $\pm 2\Delta_{\text{Ta}}$ (see Fig. 6.3). Applying a magnetic field B_{Z} perpendicular to the sample surface suppresses the superconductivity in both the tip and the sample. Above a critical field B_{C}, the sample transitions to the normal conducting phase. For tantalum, this critical field is approximately $B_{\text{C,Ta}} = 84$ mT

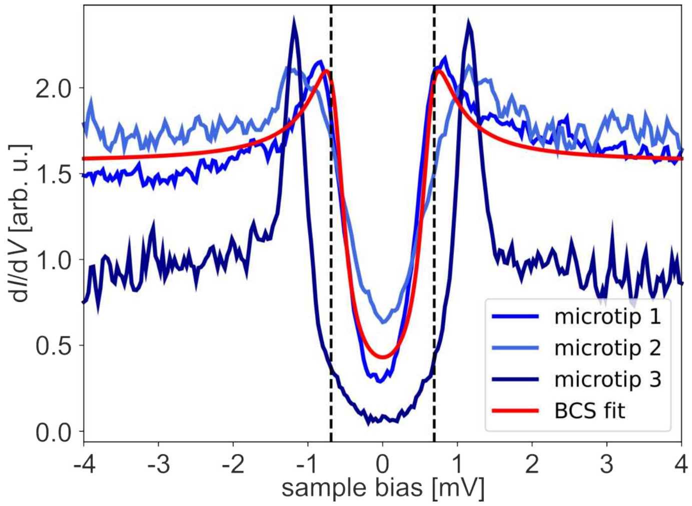

Figure 6.2: Scanning tunneling spectroscopy on Ta with different microtips. dI/dV spectra obtained on clean Ta(110) with three different microtips. The red curve is a fitted BCS gap (see Eq. 1.12) to the superconducting spectrum measured with *microtip 1* offering a $\Delta_{\text{Sample}} = 0.62$ meV and a broadening parameter $\Gamma = 0.18$ meV. The other two blueish curves have coherence peaks at clearly higher energies indicating a superconducting tip. (Cr-tip, $T = 1.3$ K, $I_{\mathrm{stab}} = 1$ nA, $V_{\mathrm{stab}} = 0.004$ V)

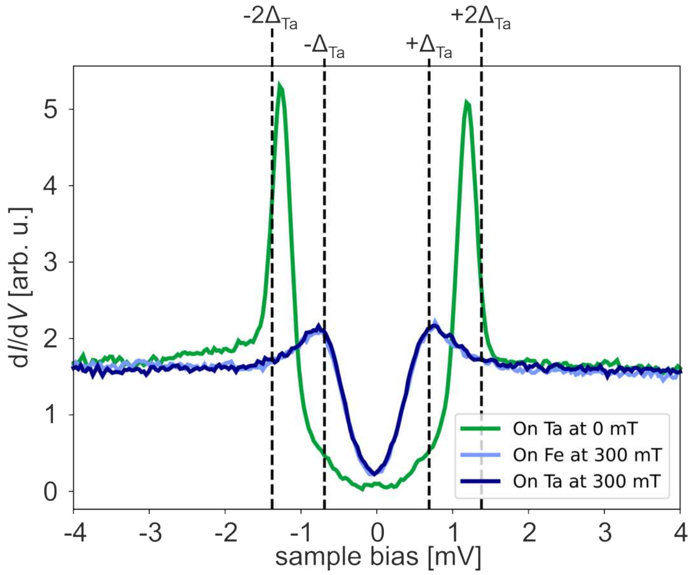

Figure 6.3: Tunneling with a superconducting tip above the critical field of Ta. An STS spectrum obtained at $B = 0$ mT (green curve) with a superconducting tip offering coherence peaks at an energy close to $\pm 2\Delta_{\text{Ta}}$. After applying a field of $B = 300$ mT two additional STS spectra on the bare Ta and on the monolayer of Fe were obtained with the same superconducting tip. (STS: Cr-tip, $T = 1.3$ K, $I_{\mathrm{stab}} = 1$ nA, $V_{\mathrm{stab}} = 0.004$ V.)

[139]. In Fig. 6.3, in addition to the zero-field spectrum, two additional spectra obtained at 300 mT on the clean Ta surface and the Fe monolayer, respectively, are depicted. The superconducting gap in the tip remains developed, while the sample is in the normal conducting state, and the superconducting spectra appear similar for both the bare Ta and the Fe monolayer. The fact that a superconducting gap is still measurable at 300 mT suggests the existence of a critical magnetic field $B_{\text{C,Tip}}$ for the superconducting tip, which must be higher than that of the sample. This phenomenon can be attributed to finite-size effects at the tip apex.

6.2 In-gap oscillations of the local density of states in the Fe-bulk areas

The spatial resolution of STS allows the observation of possible LDOS changes originating from the non-collinearity of the spin texture of the Fe monolayer. In the case of a proximitized Fe monolayer, the expected features inside the superconducting gap of the non-collinear MSH-system are in-gap bands formed by the magnetic atoms of the Fe monolayer. These bands should appear as an increased LDOS inside the superconducting gap. In Fig. 6.4, a filling of the empty states from the unaffected superconducting gap with $\Delta \approx 0.62$ mV of the bare Ta (green curve) is visible

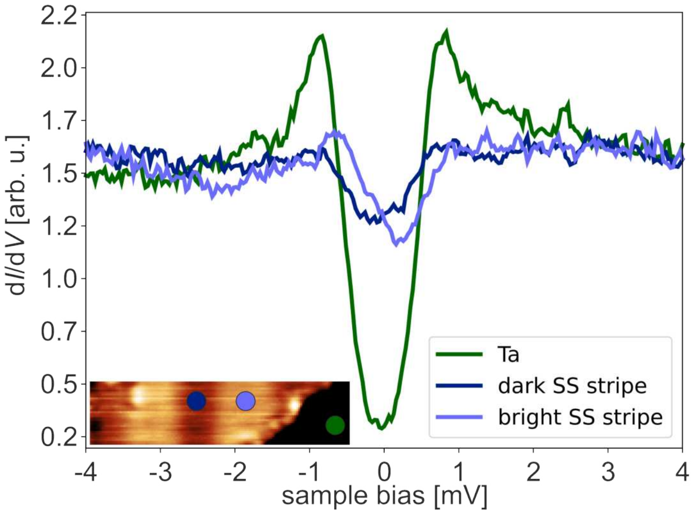

Figure 6.4: Spectral analysis of bare Ta(110) surface and Fe/Ta(110). STS measurements on bare Ta(110) surface (green cure) and on the monolayer of Fe on Ta(110) (dark and bright blue curve), at locations as indicated in the SP-STM topography image in the inset of the graph. (SP-STM: Cr-tip, *microtip 1*, $T = 1.3$ K, $I = 1$ nA, $V = 4$ mV; STS: Cr-tip, *microtip 1*, $T = 1.3$ K, $I_{\text{stab}} = 1$ nA, $V_{\text{stab}} = 0.004$ V).

in the STS measurement on the first monolayer of Fe (blue curves). While the superconductivity is notably suppressed within the monolayer of Fe, a residual reduction of the LDOS around the Fermi level remains observable. A comparison between the STS measurement on a bright stripe (parallel/anti-parallel alignment of sample and tip magnetization) of the spin spiral and on a dark stripe (anti-parallel/parallel alignment of sample and tip magnetization) of the spin spiral reveals a significant difference in the respective spectra.

To investigate the interplay between the residual superconductivity inside the monolayer of Fe and the apparent spin spiral, the focus now shifts to spectroscopic measurements with more detailed spatial resolution through the non-collinear spin texture. A suitable measurement providing more insights into the interplay is presented in Fig. 6.5. Two line STS measurements were obtained along the propagation direction of the spin spiral, namely $[1\bar{1}0]$, using both a magnetic tip (see Fig. 6.5 upper panels) and a superconducting tip (see Fig. 6.5 lower panels). In (a) and (f), the locations used for the experiments are presented in two topography STM images, where the spectroscopy locations follow the blue arrows. In panel (b), a sketch of the magnetic spin texture with the expected signal due to TMR or EMR effects is displayed. The obtained dI/dV intensity is presented as a function of location and energy in panel (c) and (g). The purple dashed lines indicate the energies related to the coherence peaks of the sample in (c) or the energy window of the convoluted superconducting gap of the tip and sample in (g).

In the case of a magnetic tip, intensity modulations are observed around the Fermi level, near the coherence peaks, and outside the superconducting gap, as visible in Fig. 6.5(c). The origin of the modulations outside the superconducting gap at negative energies is the TMR, i.e., magnetic contrast is obtained because of the spin polarization of the tip. Usually, at certain bias energies, this sensitivity can be lost, and a more uniform signal appears, as seen at positive energies outside the superconducting gap in panels (c). Panel (d) shows the dI/dV intensity averaged over a narrow energy window around zero bias, as indicated by the green dashed lines in (c), along with a cosine curve as a guide for the eye. Consequently, the spin spiral periodicity inside the superconducting gap can also be identified, indicating spin-polarized in-gap bands. The two data points with the lowest (blue) and highest (red) dI/dV intensity have been selected, and the corresponding spectra are presented in Fig. 6.5(e). Notably, in addition to the already mentioned differences at negative energies and around the Fermi level, an anti-phase between the intensities of both coherence peaks is observed, which is a sign for spin-polarized coherence peaks.

To further investigate the nature of the in-gap electronic states, the experiment is repeated with a superconducting tip, which is not sensitive to the spin spiral texture,

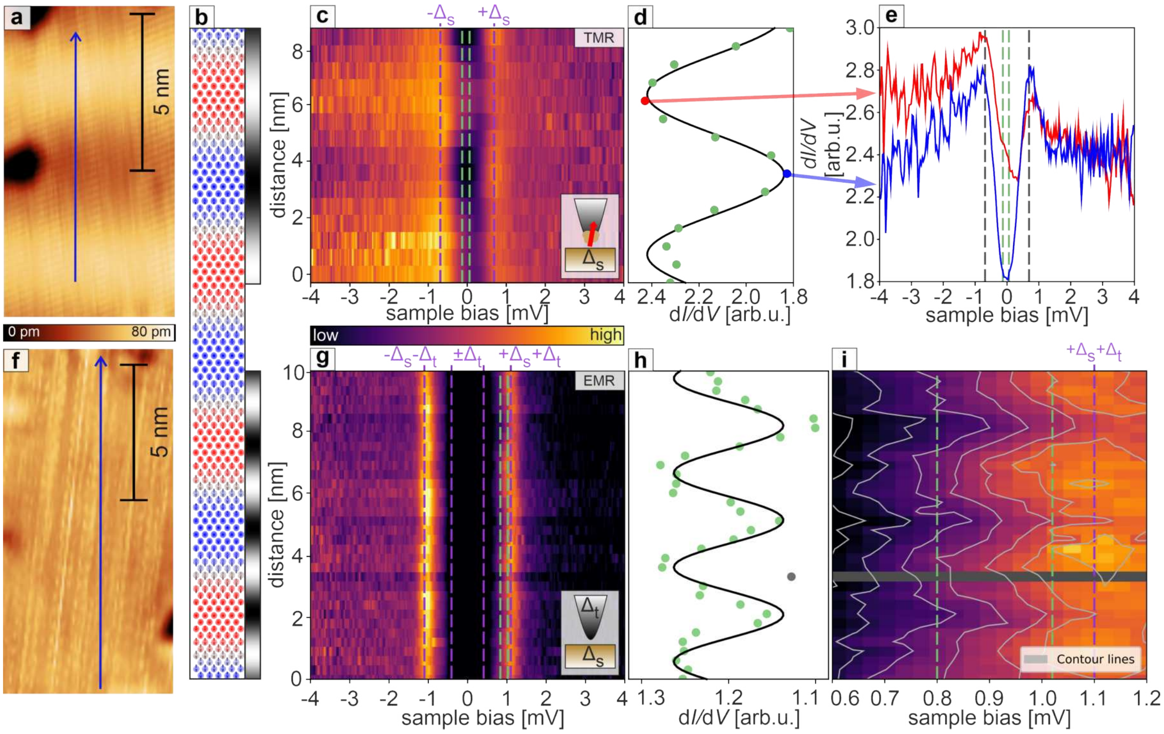

Figure 6.5: Spectroscopic characterization of the bulk areas of the Fe monolayer. (a) Topography SP-STM image including the chosen location for the line spectroscopy indicated by the blue arrow. (b) Spin configuration of the magnetic spin spiral and the expected imaging contrast due to the TMR or EMR effects. (c) Spin-resolved dI/dV spectroscopy measurements obtained with a spin-polarized tip along the spin spiral propagation direction. (d) Averaged energy slices from (c) within the range of -0.13 mV to $+0.06$ mV, as indicated by the green lines in (c); the cosine with the spin spiral period serves as a guide to the eye. (e) Comparison between two single dI/dV spectra from (c) at locations where the in-gap modulation is minimal or maximal. (f) Topography STM image illustrates the chosen location for the line spectroscopy measurement, with a superconducting tip indicated by the blue arrow. (g) dI/dV spectroscopy measurements obtained with a superconducting tip along the spin spiral as in (c). (h) dI/dV intensities along the spin spiral averaged over an energy range of $+0.80$ mV to $+1.02$ mV, as indicated by the green lines in (g); the cosine function with half the spin spiral period serves as guide to the eye. (i) Enlarged view of the dI/dV signal of (g) close to the coherence peak at positive bias voltage; the gray lines represent contour lines and highlight the periodicity of the EMR. The horizontal gray line indicates one spectrum that was not considered for the contour line plot due to momentary instability of the junction during data acquisition. ($T = 1.3$ K; (a),(c): spin-polarized tip, (c): $V = +5$ mV, $I = 5$ nA; (f),(g): superconducting tip, (g): $V = +4$ mV ,$I = 1$ nA).

as seen by the uniform signal in the topography image of Fig. 6.5(f). The superconductivity of the tip originates from a small superconducting Ta cluster attached to the apex of the Cr bulk tip. When measuring a superconducting sample with a superconducting tip, the convolution of both superconducting gaps is present, and the coherence peaks are shifted to an energy $\Delta_s + \Delta_t$ (outer purple dashed lines; the inner purple dashed lines indicate the tip gap Δ_t). The modulation of the $\mathrm{d}I/\mathrm{d}V$ signal in Fig. 6.5(g) is less visible than for the magnetic tip, however, an intensity variation with a period of half the magnetic period is apparent in the averaged $\mathrm{d}I/\mathrm{d}V$ signal over a small energy window in Fig. 6.5(h). The green dashed lines again indicate the chosen energy range used for averaging. A different presentation of the results from (g) is displayed in (i), where only a small energy range is shown, and contour lines are added to highlight the apparent modulation more clearly. The observed modulation with roughly half the magnetic period is reminiscent of the established EMR effect.

As stated above, in the topography image in Fig. 6.5(f), the contrast related to the spin spiral texture is not present compared to the measurement with a magnetic tip in (a). To ensure that the larger intensity modulations are not related to any stabilization effects of the used measurement method, additional experiments were performed in the bulk region of the Fe monolayer. The measurements were obtained on the maximum and minimum of the spin spiral contrast by compensating the corrugation, the absolute height difference at a constant bias voltage, to identify any stabilization effects. The tip was stabilized on the maximum of the spin spiral contrast. Afterwards, the feedback loop was turned off, and the tip was shifted in Z towards the sample by a distance equal to the corrugation between the spin spiral minimum and the spin spiral maximum, to perform a spectrum at this new Z-position. Additionally, a typical spectrum on the minimum of the contrast of the spin spiral without a Z-shift was performed. When a similar trend is observed between these spectra, it can be assumed that there is no significant influence of stabilization effects in the STS measurements with spin-polarized tips. The results are displayed in Fig. 6.6 and show that even with a compensated difference in the stabilization heights, a change in the DOS around the Fermi level is observed. Also, the tendency towards larger changes in the LDOS at negative bias voltages is consistent with the previous result. The measurements were obtained using a tip with different magnetization compared to the measurements presented in Fig. 6.5(e), which might explain the slight changes in the spectra.

Another way to measure this effect is by acquiring differential tunneling conductance maps at a desired bias voltage. In contrast to line or grid spectroscopy measurements, focusing on single bias voltages is possible, making the experiment much less time-consuming. Further, the measurement method might lead to a

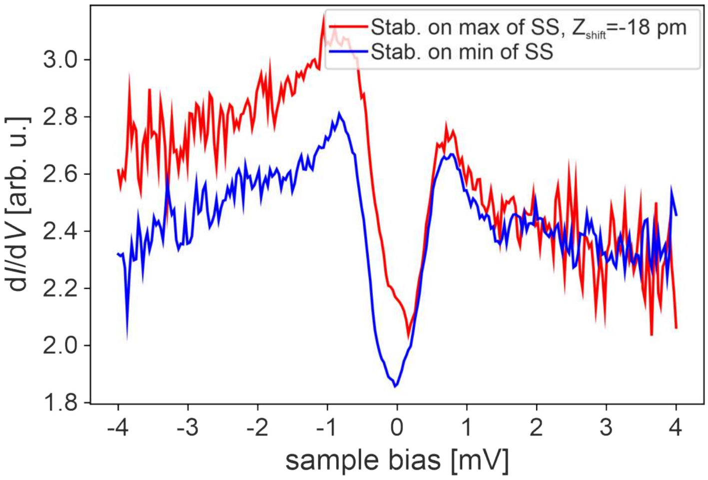

Figure 6.6: Check for stabilization effects in the superconducting spectra providing the intensity modulations. Comparison between a spectrum acquired on top of the minimum of the spin spiral and on top of the maximum of the spin spiral contrast with a Z-shift corresponding to the height difference between maximum and minimum of the spin spiral stabilized at $V = +5$ mV. (STS: Cr-tip, $T = 1.3$ K, $I_{\mathrm{stab}} = 5$ nA, $V_{\mathrm{stab}} = 0.005$ V)

higher spatial resolution of the in-gap state modulations. To realize such a measurement, the multipass mode implemented in the Nanonis software was used. The mode measures each line in constant-current mode (at V and I) first and then replays each line with the feedback off at a different tip-sample distance (by adding z_{offset}) and a different value for the sample bias V_{meas}. To gain insights into the physics of the interplay of the in-gap states with the spin spiral texture, a bias voltage close to $V_{\mathrm{meas}} = 0$ V was chosen to be as deep as possible inside the superconducting gap. In Fig. 6.7(a), such a measurement is presented, where a tip change from a spin-polarized tip (upper part) and a non-magnetic tip (lower part) occurred. Two changes of the tip apex are present, resulting in the apparent contrast changes. A switching spin polarization of the tip apex leads to frequent contrast inversions repeating after a few scan lines for the spin-polarized microtip.

The analysis of the periods by line profiles (see Fig. 6.7(b)) leads to the following conclusion: although the signal variation is weaker in the case of a non-magnetic tip compared to the spin-polarized case, both periods are recognized and separated by a transition area between the tip changes without a clear corrugation pattern related to the magnetic texture. Consequently, it allows the conclusion that the local spin-averaged in-gap states are also affected by the presence of the non-collinear spin texture, leading to an EMR-related contrast in the STM measurements using a non-magnetic tip.

To gain more insights into the underlying mechanisms, the results obtained by

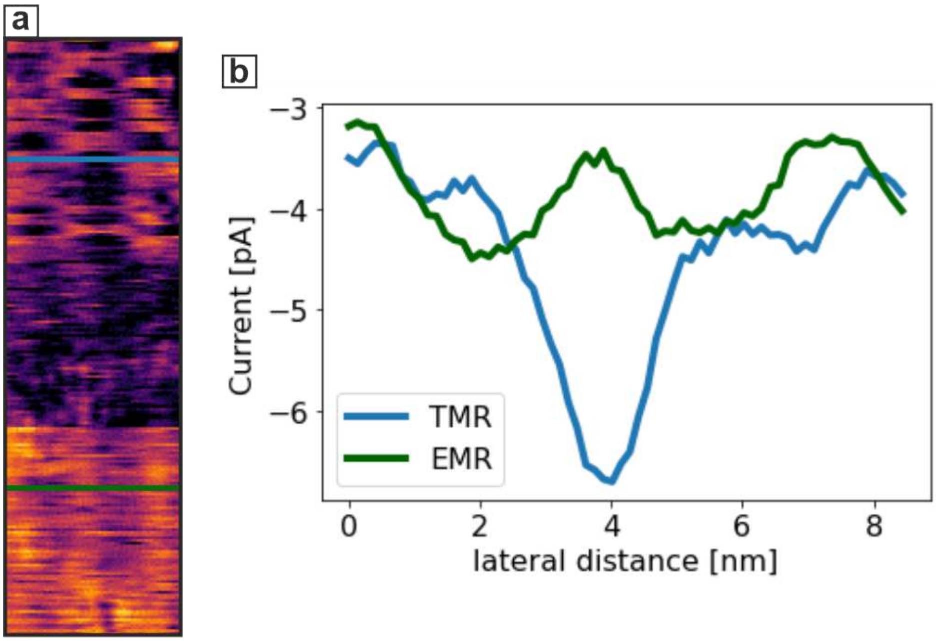

Figure 6.7: Spatially resolved intensity modulations. (a) Spin-resolved and Spin-averaged in-gap real-space current maps exhibiting the spin spiral period or half the magnetic period, respectively, separated by an intermediate area enclosed by two tip changes. (Multipass mode: $V_{\text{stab}} = -50$ mV, $I_{\text{stab}} = 1$ nA, $z_{\text{offset}} = -150$ pm, $V_{\text{meas}} = +0.1$ mV).

collaborative work with the group of Prof. Dr. Dirk K. Morr, particularly Jasmin Bedow, a PhD student within the group, are incorporated in the following. A minimal Hamiltonian is used that incorporates the interplay of an s-wave SC, Rashba SOC, and a magnetic spin spiral with a period of 7 nm (for details, see Ref. [68]). The first step in the calculations of the sample system was to identify a parameter set that adequately describes the observed physics. In contrast to Ref. [50], Rashba SOC is added to the calculations, and the effects of this term will help to identify the desired parameter choice.

The calculations considered all cases, a homogeneous spin spiral texture with and without a finite Rashba SOC and an inhomogeneous spin spiral with and without Rashba SOC to possibly conclude which kind of spin texture better describes the experimental results. In Fig. 6.8(a), the first case for a homogeneous spin spiral (sinusoidal) without Rashba SOC describes the scenario considered in [50] and exhibits no LDOS modulation in the spin-averaged LDOS (EMR case). For the other two cases, where either a finite Rashba SOC (representing TAMR-related effects) is added to a homogeneous spin spiral or an inhomogeneous spin spiral (leading to NCMR-related effects) with $\alpha = 0$ is assumed, both result in an oscillation in the spin-averaged LDOS as observed in the experiments. The oscillations also exhibit half the period of the magnetic texture, consistent with the dI/dV modulation observed

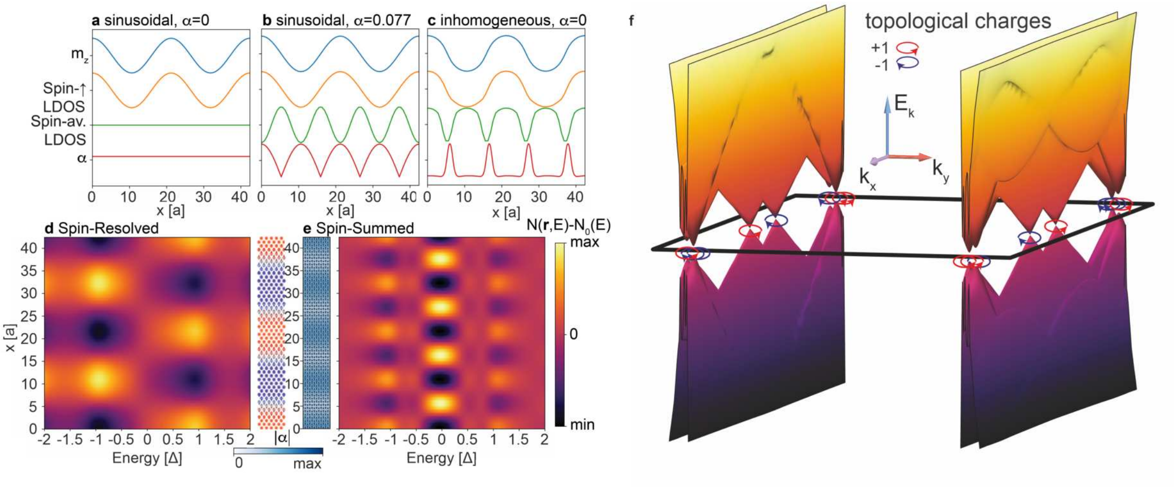

Figure 6.8: Microscopic origin of the TMR and EMR signal. Linecut of the out-of-plane magnetization (blue), spin-↑ LDOS (orange), spin-summed LDOS (green) and total Rashba SOC for a sinusoidal spin spiral with (a) $\alpha = 0$ and (b) $\alpha = 0.077\Delta$, and **c** an inhomogeneous spin-spiral with $\alpha = 0$. For the case shown in (b), the energy- and position-dependent (d) spin-resolved and (e) spin-summed LDOS for a linecut along the spiral direction, together with the spatial dependence of m_z and the total Rashba SOC. (f) Electronic structure in the magnetic Brillouin zone exhibiting nodal points with non-zero topological charge.

in the experiment.

To identify the optimal choice of Rashba SOC or inhomogeneity of the spin spiral in the system, several ratios were considered. In the following the focus is on the case of a homogeneous spin spiral with $\alpha = 0.077$ (see Fig. 6.8(b)), noting that qualitatively similar results were obtained for an inhomogeneous spin spiral (see Fig. 6.8(c)). For this parameter set, the LDOS as a function of energy and distance is plotted for the spin-resolved case in Fig. 6.8(d) and the spin-averaged case in Fig. 6.8(e). In the spin-resolved case, the highest modulation of the LDOS signal is at $-\Delta$, corresponding to the coherence peak at negative energy, where the highest variation of the signal also occurs in the experiment. For the spin-averaged case, the highest modulation appears near the Fermi level and not close to the coherence peaks as in the experiment, however, a modulation is clearly visible. In Fig. 6.8(f), the calculated band structure of the system is presented and shows that the system is a nodal point superconductor, with the nodal points offering different topological charges as sketched with blue and red arrows. Consequently, the parameters that describe the experiment well are inside a topologically non-trivial phase in the parameter space.

Summarizing, a parameter set used in a minimal Hamiltonian following the tight-binding model effectively describes the experimental observations of the bulk properties of the Fe monolayer on Ta(110). The LDOS intensity modulations of the electronic in-gap states along the spin spiral propagation direction align with the periodicity or half the periodicity of the magnetic texture, assuming a spin-polarized tip (TMR) or a non-magnetic tip (EMR), respectively. Since similar results can be obtained by assuming an inhomogeneous spin spiral with $\alpha = 0$, the outcomes of the tight-binding calculations are inconclusive in determining whether the system offers a homogeneous or inhomogeneous spin spiral. However, it can be concluded that the simplified case of a homogeneous spin spiral without external Rashba SOC, as described in [50], is not sufficient to describe the observed physics measured in the model system. Since the system is assumed to be a topological nodal-point superconductor, low energy modes at the boundaries of the Fe islands, where the topology changes instantly, are expected. These topological boundary modes will be discussed in the following section.

6.3 Topological boundary modes at Fe edges

After presenting the bulk properties of the Fe monolayer, the question remains: is it possible to experimentally show that the system is in a topologically non-trivial phase consistent with theoretical predictions? A characteristic signature of topological superconductivity is the presence of dispersing chiral edge modes providing unidirectional edge currents. The existence of a topological edge mode should result in an increase in the dI/dV intensity near the edges of the Fe monolayer islands. Therefore, the focus will now shift to these boundaries. Fig. 6.9(a) offers a constant-current STM image of an island of the Fe monolayer (bright) on the Ta(110) surface (black). The island has two main edge orientations, namely along $[001]$ and $[1\bar{1}1]$. Additional and not included measurements show that the system avoids straight edges along $[1\bar{1}0]$. In Fig. 6.9(b), a line spectroscopy, located as indicated by the blue arrow in (a), shows a bright feature at the boundary between the Ta and Fe-bulk region, highlighting the increased number of in-gap states due to the presence of an edge state. The inset within Fig. 6.9(b) displays both the topography- and dI/dV-channel at $V = 0$ V during the line spectroscopy. The position of the peak in the dI/dV-channel overlaps with the region where the signal of the Z(m)-channel decays to the Ta area, meaning the tip measures also a higher signal located next to the edge atom by approaching the Ta terrace. In Fig. 6.9(c), three single-point spectra from the line spectroscopy, located as indicated by the colored circles in (b), are displayed and visualize an enhanced signal around the Fermi level in the spectrum at the $[001]$-edge, as expected for a topological edge state.

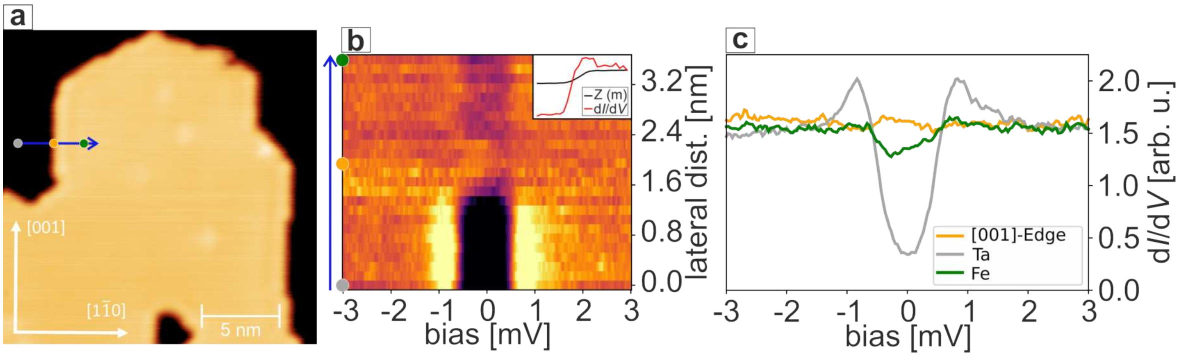

Figure 6.9: Line spectroscopy across a topological edge state. (a) A constant-current STM image of an irregularly shaped island of the Fe monolayer on Ta(110). (b) Line spectroscopic measurement that was performed above a $[001]$-edge at the location marked by the blue arrow in a). (c) Three single-point spectra from the measurement in b) on bare Ta, the $[001]$-edge and the Fe bulk area, located as indicated by the colorized circles in b), are presented. (superconducting tip, $T = 1.3$ K. (a) $I = 1$ nA, $V = 10$ mV; (b,c) $I_{\text{stab}} = 1$ nA, $V_{\text{stab}} = 4$ mV, $V_{mod} = 50$ µV).

As for the bulk properties, one can supplement the measurements by multipass experiments above an island with straight edges to resolve the evolution of the edge state in two dimensions. In Fig. 6.10(a), a multipass experiment is presented, re-

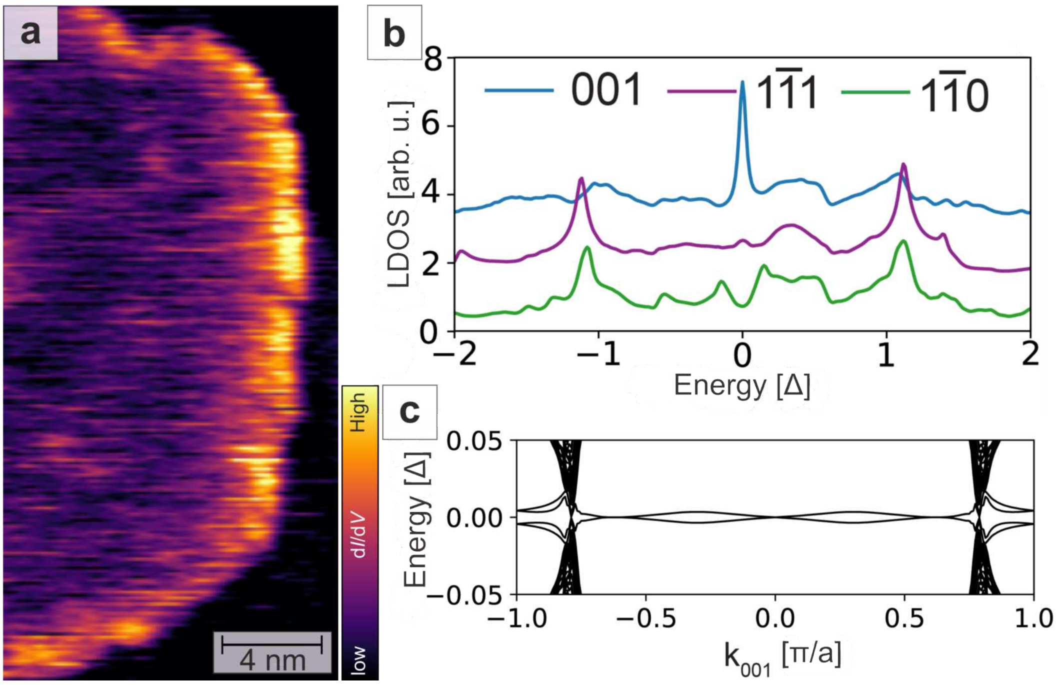

Figure 6.10: Chiral edge mode in Fe/Ta(110). (a) A multipass experiment of a Fe monolayer island offering straight edges along $[001]$ measured at a bias voltage close to the Fermi level. (b) Calculated LDOS at a $[001]$-edge (blue), $[1\bar{1}0]$-edge (purple) or $[1\bar{1}0]$-edge (green). (c) Electronic band structure as a function of momentum along the $[001]$-edges of a ribbon system. The assumed spin spiral texture terminates with spiral termination angle $\Theta = 0°$. (Multipass dI/dV, $T = 1.3$ K, $V = -50$ mV, $I = 1$ nA, $z_{\text{offset}} = -150$ pm, $V_{\text{meas}} = +0.1$ mV, $V_{mod} = 50$ µV).

vealing an increased dI/dV signal along the edges of the Fe monolayer island (purple) on top of the clean Ta (black). Additionally, a variation of the dI/dV signal along the different edge orientations is identified. While the signal is very strong along $[001]$-edges, a clear weakening of the signal along $[1\bar{1}1]$-edges is present. A comparison of the calculated LDOS for three edge orientations of the system (see Fig. 6.10(b)) reveals a clear peak around the Fermi level, but exclusively for the $[001]$-edge. This peak originates from a low-energy, weakly dispersing chiral edge mode, that connects nodal points of opposite topological charge, as shown in the plot of the electronic band structure of a ribbon system with edges along $[001]$ (see Fig. 6.10(c)). The weak dispersion provides a low group velocity and topological protection of these boundary modes. The results manifest that the enhanced dI/dV signal in Fig. 6.10(a) reflects the existence of a chiral edge mode. The weaker signal intensity along different edge orientations is consistent with previously investigated topological nodal-point superconductors [34, 36, 38].

6.4 Effect of the non-collinearity on chiral edge states

Since the system of one monolayer of Fe on Ta(110) exhibits a non-collinear spin texture, an arbitrary angle θ between the spin direction at the edge and the surface normal for edges along $[001]$ can occur, resulting in FM edges with different spin polarizations. One monolayer of Fe on Ta(110) offers the first platform to experimentally investigate the dependency of the chiral edge mode on the spin orientation along the boundary. If the observed edge states offer a change in dispersion or spin polarization, differences in signal intensity should be detectable at arbitrary magnetized FM edges along $[001]$. To discuss the different spin spiral termination angles at $[001]$-edges, calculations will first be presented to gain deeper insights into the expected changes of the edge state by changing the apparent spin polarization at the edge. In Fig. 6.11(a) and Fig. 6.11(b), two sketches of different spin termination of the spin spiral and the corresponding dispersion of the edge state are depicted. Interestingly, the dispersion of both spiral terminations drastically differs from each other. While the dispersion of the edge state with out-of-plane termination at the edge appears almost flat (exhibiting high LDOS at zero energy), the edge state with in-plane magnetization shows a comparably large dispersing behavior (small LDOS at zero energy). Since the chosen termination angles are close to out-of-plane or in-plane magnetization for the considered cases in (a) or (b), respectively, it can be concluded that for out-of-plane spiral termination, a higher LDOS is expected than for in-plane spiral termination at edges along $[001]$. In Fig. 6.11(c), the calculated low-energy LDOS as a function of the termination angle θ is presented. The expected change in intensity for different spiral terminations is observed, and again, the change in the dispersion of the edge state between in-plane and out-of-plane spiral termination is noticeable.

An experimental zero-bias dI/dV map obtained with multipass mode is depicted in Fig. 6.12(a), where the edges along $[001]$ display the most pronounced intensity compared to other edge orientations. Along a particular step edge with $[001]$ orientation, the intensity is almost constant, as expected for this kind of edge due to its ferromagnetic spin orientation along the boundary. Furthermore, different edges along $[001]$ show several contrast levels, suggesting a change in the dispersion of the edge state due to the expected variation of spin orientation between different step edges along the $[001]$-direction. The inset of Fig. 6.12(a) presents a SP-STM measurement of the same island, providing a rough insight into the different spiral terminations along the boundary of the island. The calculated LDOS in Fig. 6.12(b) for an island with the same size and shape as the one investigated in the experiment appears to be in good agreement with the experimental results. Furthermore, a sketch of the m_z component of the considered spin spiral (white line at the top

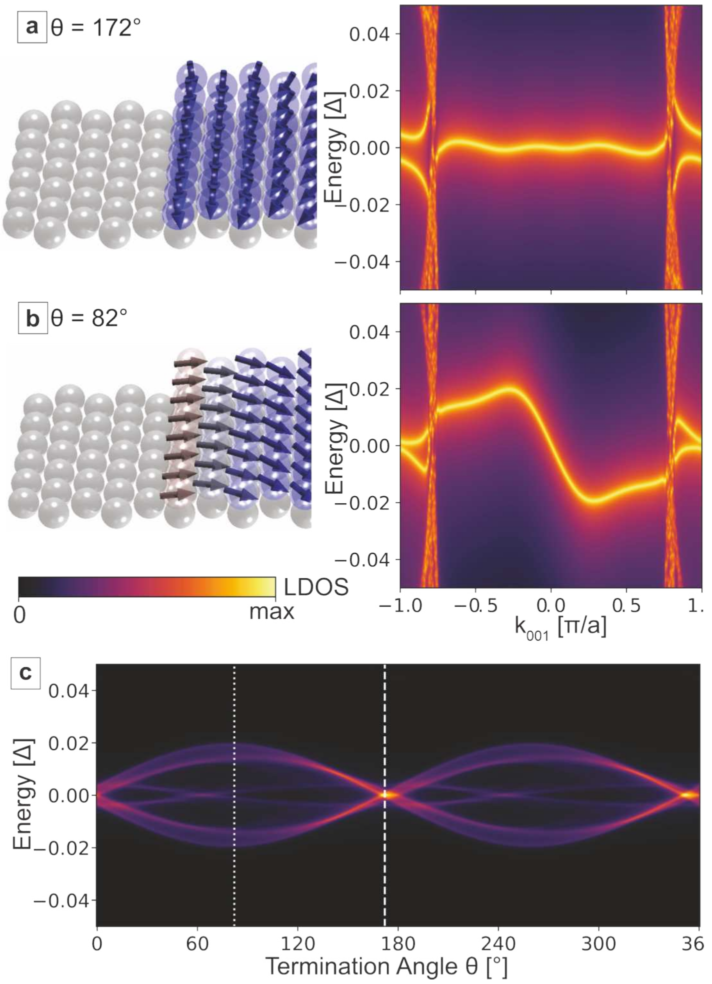

Figure 6.11: Termination angle dependency of the chiral edge state dispersion. Spectral function as a function of momentum along a ribbon with two $[001]$-edges and a termination angle of the spin spiral of $\theta = 172°$ in (a) and $\theta = 82°$ in (b). (c) Low-energy LDOS at an $[001]$-edge as a function of the termination angle θ. The white dashed and dotted lines represent the $\theta = 172°$ and $\theta = 82°$ terminations, respectively.

of the image) visualizes the varying phase of the spin spiral along the boundary of the island resulting in the different LDOS intensities. In conclusion, the chiral edge modes expected for a topological nodal-point superconductor were revealed experimentally and are in good agreement with tight-binding calculations by Jasmin Bedow [68]. These observations verify the topological nature of the sample system and provide the opportunity to discover the dependency of the chiral edge mode dispersion on the apparent spin orientation. The calculations predict an almost non-dispersive chiral edge mode for out-of-plane spin terminations and strongly dispersive chiral edge modes for edges with in-plane spin termination.

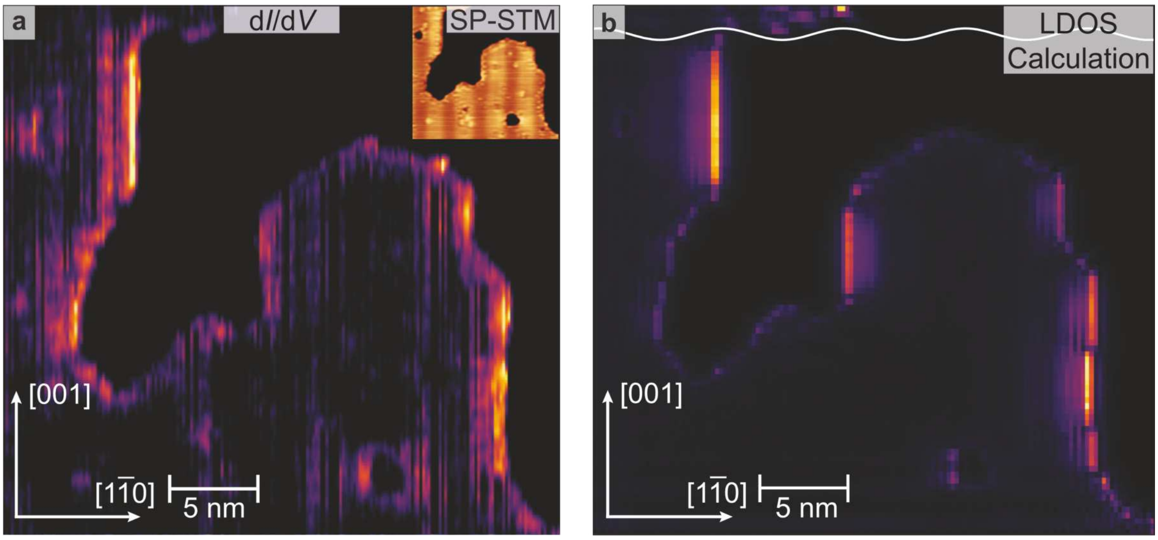

Figure 6.12: Comparison of chiral edge state intensity with the calculated LDOS of a modeled island. (a) A multipass spin-averaged zero-bias dI/dV map with fast scan direction along $[001]$-edges of an irregularly shaped Fe island; the inset shows a SP-STM constant-current image of the same area. (b) Calculated spin-averaged zero-energy LDOS for a Fe island of the same size and shape as that presented in a). The white line reflects the m_z-component of the spin spiral along the $[1\bar{1}0]$-direction. (Multipass dI/dV, $T = 1.3$ K, $V = -50$ mV, $I = 1$ nA, $z_{\text{offset}} = -150$ pm, $V_{\text{meas}} = 0$ mV, $V_{mod} = 50$ µV; inset constant-current SP-STM: $T = 4.2$ K, $I = 1$ nA, $V = 4$ mV).

6.5 Comparison to related sample systems

Finally, for better classification of the obtained results, this section will provide a brief overview of related sample systems and highlight the new aspects of Fe/Ta(110).

The established non-collinear spin texture realized on an s-wave superconductor offers the opportunity to investigate the interaction of magnetic non-collinearity with superconductivity. Several works have investigated similar systems, particularly those involving the elemental superconductor Nb. The critical temperature of Nb ($T_C = 9.2$ K) allows for better energy resolution during the spectroscopic analysis of sample systems. This higher energy resolution has motivated several studies with Nb substrates, leading to reproducible recipes for obtaining the desired surface cleanness and preparing homogeneous magnetic monolayers on top. These recipes were lacking for Ta samples prior to this thesis. In the following, two works focusing on magnetic monolayers on the superconductor Nb are discussed.

In the structural analysis of the samples with inhomogeneous growth of Fe (see Sec. 4.2), many similarities can be identified in the Fe reconstructions on the surfaces of Nb(110) and Ta(110). In Fig. 6.13, an overview of the different types of

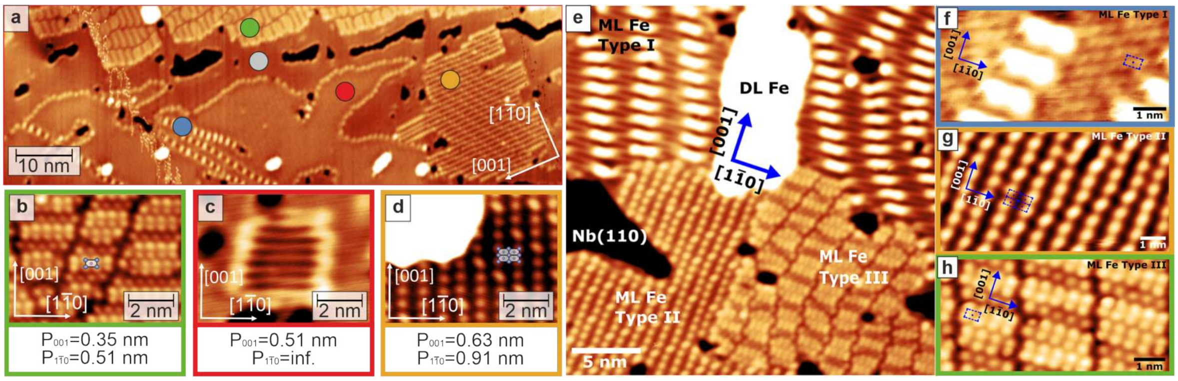

Figure 6.13: Comparison of the surface reconstructions system Fe/Nb(110). (a),(e) Overview image of one monolayer Fe on the surface of Ta(110) or Nb(110), respectively. In (b),(c),(d) and (f),(g),(h), a closer look at the observed reconstructions in Fe/Ta(110) or Fe/Nb(110), respectively, is presented. The images of the sample system of Fe/Nb(110) were taken from [120].

reconstructions observed in both sample systems is depicted, with Fe/Ta(110) on the left and Fe/Nb(110) [120] on the right side. The similar types of reconstructions of both sample systems are marked with the same color. Further, the reconstruction marked with a blue dot in the STM image in Fig. 6.13(a) appears similar to the type-I reconstruction for Fe/Nb(110), albeit, an additional zoomed-in image was not acquired. Some similarities are expected for both systems due to the almost identical lattice constants of Ta (331 pm) and Nb (330 pm). Only one reconstruction in Fe/Ta(110), marked with a red rectangle and dot, cannot be identified in Fe/Nb(110). Interestingly, this reconstruction type remains in comparably clean sample preparations of Fe/Ta(110) (see small reconstructed patches in Sec. 5.1).

In contrast to Fe/Ta(110), Fe/Nb(110) always exhibits a FM ground state in the reconstructed layer of Fe, with no indications of topological superconductivity, such as edge states at the boundary of Fe islands.

A rather similar sample system is one monolayer of Mn on Nb(110) [34]. It offers nodal-point superconductivity similar to the sample system presented in this thesis. A comparison of the calculated electronic band structures of the Brillouin zones is shown in Figs. 6.14(c),(d). In the calculations of both systems, a topological charge for each nodal point was observed, making the nodal-point superconductors topologically non-trivial. As an indication of topological superconductivity in the experiments, both systems offer edge states with enhanced signal intensity along certain edge orientations.

The difference lies in the observed magnetic ground state. In Mn/Nb(110), a collinear antiferromagnetic state (see Fig. 6.14(b)) was identified [34], whereas the

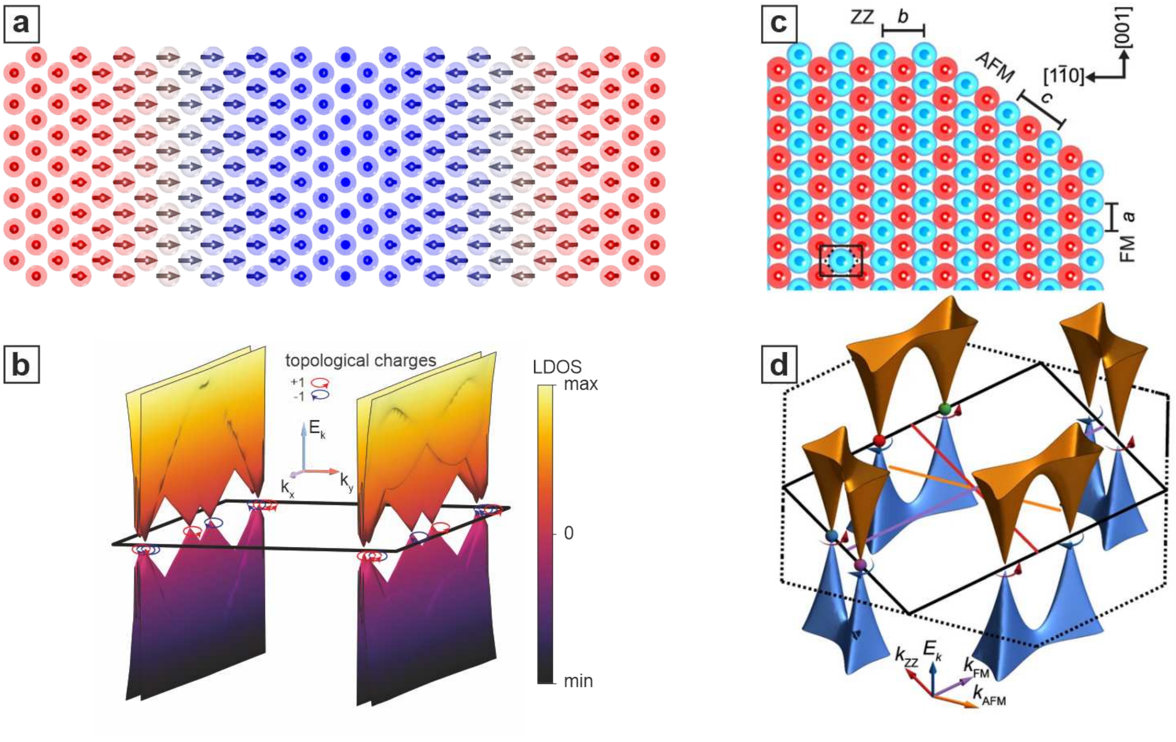

Figure 6.14: Comparison of the magnetic ground state and Brillouin zone between Fe/Ta(110) and Mn/Nb(110). (a) The spin spiral ground state for Fe/Ta(110) sample preparations, exhibiting a not entirely closed Fe monolayer, with the calculated electronic band structure for the entire Brillouin zone of the system in (b). (c) A sketch of the magnetic ground state of one monolayer of Mn on Nb(110), together with the calculated electronic band structure for the entire Brillouin zone of the system in (d). Both results were taken from [34].

established spin spiral (see Fig. 6.14(a)) in the presented system of Fe/Ta(110) offers the opportunity to investigate the influence of different spin alignments in the bulk areas and at the boundaries of the islands on the in-gap state distribution.

6.6 Conclusion and Outlook

The superconducting phase of Fe/Ta(110) provides insights into the interaction of a non-collinear spin texture with an s-wave superconductor, marking the first experimental realization of such a non-collinear MSH-system. In the bulk area of the Fe islands, intensity modulation of the LDOS at energies around the coherence peaks and inside the superconducting gap can be identified. This modulation follows the period of the magnetic texture when measured with a magnetic tip (TMR) and half of the period of the magnetic texture when measured with a non-magnetic tip, which is attributed to EMR-related effects. In tight-binding calculations, the calculated spatially resolved LDOS of the bulk areas of the sample system shows oppositely spin-polarized coherence peaks which might be related to the observed anti-phase observation of the coherence peaks in the experiment. The calculations also show LDOS intensity modulations inside the superconducting gap following the magnetic period (spin-polarized) or half the magnetic period (spin-averaged), which explains the experimentally observed intensity modulations.

At the boundaries of the Fe islands, a signal enhancement with the highest intensities along the $[001]$-edges is observable, indicating a topologically non-trivial phase of the MSH-system. The calculations conclude that the system is a topological nodal-point superconductor with chiral edge mode dispersion dependency on the spin spiral termination angle at the edge, a phenomenon that has not been discussed before in any of the established MSH-systems.

To discuss a possible application of the observed phenomena, the proposal already discussed in the previous chapter, where a racetrack with a meron-antimeron domain wall was considered, will be referred to. For a possible racetrack realization, adding further domain walls in the racetrack is necessary. In Fig. 6.15(a), two meron-antimeron domain walls are sketched and the discovered edge mode along $[001]$ is added by yellow clouds. A movement of the domain wall by a spin-polarized current $\vec{I}$ or a magnetic field $\vec{B}$ would be the simultaneous transport of the chiral

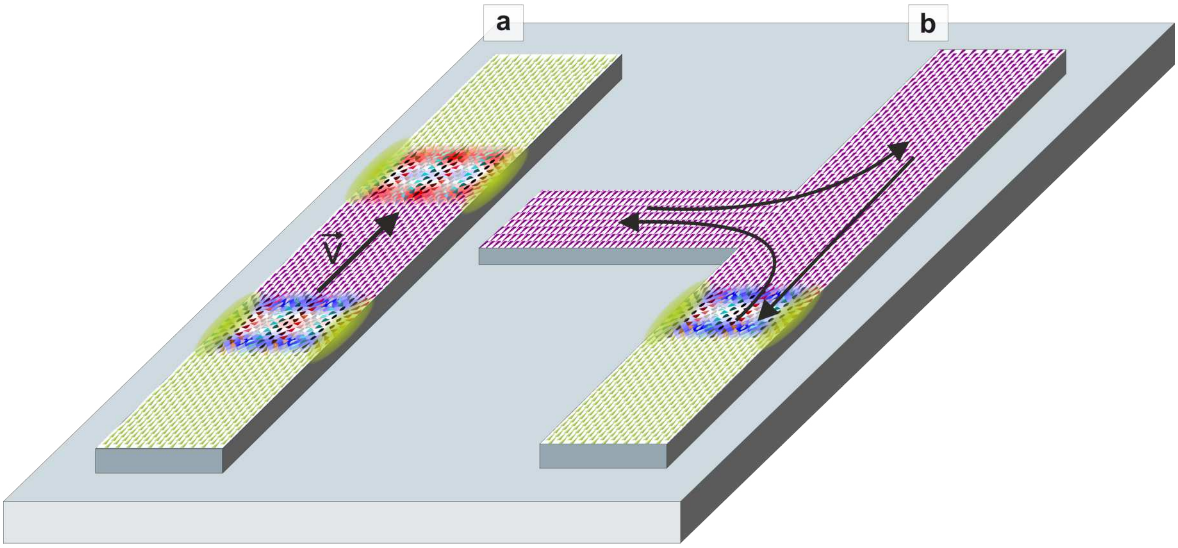

Figure 6.15: Meron-antimeron domain wall with a chiral edge mode on a racetrack. (a) The same sketch of a racetrack as in the previous chapter with added edge modes (yellow clouds) along the ferromagnetically polarized edges. In (b), two non-trivial meron-antimeron domain walls on a racetrack.

edge mode and the topological charge of the spin texture.

Further simulations could provide more insights into these ideas. The controlled creation of similar spin textures in racetracks was already demonstrated in the work of Schäffer $et\ al.$ [140]. A similar approach could create the discussed domain wall configurations and offer the opportunity to investigate the dynamics of these domain walls and their topological properties.

An additional aspect of this proposal is the realization of computational operations in such a racetrack device, e.g. braiding [141–143] of this kind of domain wall with a chiral edge mode. Usually the chemical potential is used to manipulate anyons in a T-junction [144], however, in reality the chemical potential is not a parameter that can be changed directly. In the case of a meron-antimeron domain wall racetrack, the manipulation is comparable easy with already established ways like the magnetic field or spin-polarized current manipulation. In Fig. 6.15(b), a sketch of the meron-antimeron domain wall in a T-junction is presented and illustrates a possible way to exchange the position of both edge modes (following the black arrows in Fig. 6.15(b)), which needs to validate whether this can be used for a computational operation similar to the braiding of anyons.

Another open question is how the LDOS changes across such a domain wall configuration, transitioning from one in-plane domain to another. A chiral edge state along the FM edges of the wall texture is expected, however, the transitioning from the in-plane domains across the meron-antimeron domain wall might offer another edge state with a different dispersion.

Ultimately, the field dependence data of the system shows that the wall texture can be compromised by applying an out-of-plane magnetic field. This results in tiny domain wall configurations where potentially a transfer of the more delocalized edge state to a Majorana bound state might be observable if a system can be found that has a higher critical field and also has such a meron-antimeron domain wall configuration like in the monolayer of Fe on Ta(110).

Bibliography

[1] *Global data storage supply and demand 2009-2020*, Statista, `https://www.statista.com/statistics/751749/worldwide-data-storage-capacity-and-demand/` (visited on 07/15/2024).

[2] S. Sagiroglu and D. Sinanc, “Big data: A review”, in 2013 International Conference on Collaboration Technologies and Systems (CTS) (May 2013), pp. 42–47.

[3] R. P. Feynman, “Simulating physics with computers”, Int J Theor Phys **21**, 467–488 (1982).

[4] P. Shor, “Algorithms for quantum computation: discrete logarithms and factoring”, in Proceedings 35th Annual Symposium on Foundations of Computer Science (Nov. 1994), pp. 124–134.

[5] Y. Ando and L. Fu, “Topological Crystalline Insulators and Topological Superconductors: From Concepts to Materials”, Annual Review of Condensed Matter Physics **6**, 361–381 (2015).

[6] A. Y. Kitaev, “Unpaired Majorana fermions in quantum wires”, Phys.-Usp. **44**, 131 (2001).

[7] L. Fu and C. L. Kane, “Superconducting Proximity Effect and Majorana Fermions at the Surface of a Topological Insulator”, Phys. Rev. Lett. **100**, 096407 (2008).

[8] V. Mourik, K. Zuo, S. M. Frolov, S. R. Plissard, E. P. A. M. Bakkers, and L. P. Kouwenhoven, “Signatures of Majorana Fermions in Hybrid Superconductor-Semiconductor Nanowire Devices”, Science **336**, 1003–1007 (2012).

[9] I. Žutić, J. Fabian, and S. Das Sarma, “Spintronics: Fundamentals and applications”, Rev. Mod. Phys. **76**, 323–410 (2004).

[10] A. Hirohata, K. Yamada, Y. Nakatani, I.-L. Prejbeanu, B. Diény, P. Pirro, and B. Hillebrands, “Review on spintronics: Principles and device applications”, Journal of Magnetism and Magnetic Materials **509**, 166711 (2020).

[11] V. Baltz, A. Manchon, M. Tsoi, T. Moriyama, T. Ono, and Y. Tserkovnyak, “Antiferromagnetic spintronics”, Rev. Mod. Phys. **90**, 015005 (2018).

[12] J. Xia, X. Zhang, X. Liu, Y. Zhou, and M. Ezawa, “Qubits based on merons in magnetic nanodisks”, Commun Mater **3**, 1–9 (2022).

[13] K. v. Klitzing, G. Dorda, and M. Pepper, “New Method for High-Accuracy Determination of the Fine-Structure Constant Based on Quantized Hall Resistance”, Phys. Rev. Lett. **45**, 494–497 (1980).

[14]M. Kohmoto, “Topological invariant and the quantization of the Hall conductance”, Annals of Physics **160**, 343–354 (1985).

[15]K. von Klitzing, “The quantized Hall effect”, Rev. Mod. Phys. **58**, 519–531 (1986).

[16]D. J. Thouless, M. Kohmoto, M. P. Nightingale, and M. den Nijs, “Quantized Hall Conductance in a Two-Dimensional Periodic Potential”, Phys. Rev. Lett. **49**, 405–408 (1982).

[17]L. Fu, C. L. Kane, and E. J. Mele, “Topological Insulators in Three Dimensions”, Phys. Rev. Lett. **98**, 106803 (2007).

[18]M. König, S. Wiedmann, C. Brüne, A. Roth, H. Buhmann, L. W. Molenkamp, X.-L. Qi, and S.-C. Zhang, “Quantum Spin Hall Insulator State in HgTe Quantum Wells”, Science **318**, 766–770 (2007).

[19]D. Hsieh, D. Qian, L. Wray, Y. Xia, Y. S. Hor, R. J. Cava, and M. Z. Hasan, “A topological Dirac insulator in a quantum spin Hall phase”, Nature **452**, 970–974 (2008).

[20]D. Hsieh, Y. Xia, D. Qian, L. Wray, J. H. Dil, F. Meier, J. Osterwalder, L. Patthey, J. G. Checkelsky, N. P. Ong, A. V. Fedorov, H. Lin, A. Bansil, D. Grauer, Y. S. Hor, R. J. Cava, and M. Z. Hasan, “A tunable topological insulator in the spin helical Dirac transport regime”, Nature **460**, 1101–1105 (2009).

[21]S.-Y. Xu, I. Belopolski, N. Alidoust, M. Neupane, G. Bian, C. Zhang, R. Sankar, G. Chang, Z. Yuan, C.-C. Lee, S.-M. Huang, H. Zheng, J. Ma, D. S. Sanchez, B. Wang, A. Bansil, F. Chou, P. P. Shibayev, H. Lin, S. Jia, and M. Z. Hasan, “Discovery of a Weyl fermion semimetal and topological Fermi arcs”, Science **349**, 613–617 (2015).

[22]N. Romming, C. Hanneken, M. Menzel, J. E. Bickel, B. Wolter, K. von Bergmann, A. Kubetzka, and R. Wiesendanger, “Writing and deleting single magnetic skyrmions”, Science **341**, 636–639 (2013).

[23]M. Sato and Y. Ando, “Topological superconductors: a review”, Rep. Prog. Phys. **80**, 076501 (2017).

[24]B. A. Bernevig, *Topological Insulators and Topological Superconductors* (Princeton University Press, Apr. 7, 2013).

[25]A. Kitaev, “Periodic table for topological insulators and superconductors”, AIP Conference Proceedings **1134**, 22–30 (2009).

[26]S.-S. Chern, “Characteristic Classes of Hermitian Manifolds”, Annals of Mathematics **47**, 85–121 (1946).

[27] M. Z. Hasan and C. L. Kane, “Colloquium: Topological insulators”, Rev. Mod. Phys. **82**, 3045–3067 (2010).

[28] S. Nadj-Perge, I. K. Drozdov, B. A. Bernevig, and A. Yazdani, “Proposal for realizing Majorana fermions in chains of magnetic atoms on a superconductor”, Phys. Rev. B **88**, 020407 (2013).

[29] A. Palacio-Morales, E. Mascot, S. Cocklin, H. Kim, S. Rachel, D. K. Morr, and R. Wiesendanger, “Atomic-scale interface engineering of Majorana edge modes in a 2D magnet-superconductor hybrid system”, Science Advances, `10.1126/sciadv.aav6600` (2019).

[30] M. Tinkham, *Introduction to Superconductivity* (McGraw Hill, 1996), 488 pp.

[31] *The Nobel Prize in Physics 1913*, NobelPrize.org, `https://www.nobelprize.org/prizes/physics/1913/summary/` (visited on 06/27/2024).

[32] W. Meissner and R. Ochsenfeld, “Ein neuer Effekt bei Eintritt der Supraleitfähigkeit”, Naturwissenschaften **21**, 787–788 (1933).

[33] J. Auer and H. Ullmaier, “Magnetic Behavior of Type-II Superconductors with Small Ginzburg-Landau Parameters”, Phys. Rev. B **7**, 136–145 (1973).

[34] M. Bazarnik, R. Lo Conte, E. Mascot, K. von Bergmann, D. K. Morr, and R. Wiesendanger, “Antiferromagnetism-driven two-dimensional topological nodal-point superconductivity”, Nat Commun **14**, 614 (2023).

[35] A. P. Schnyder and P. M. R. Brydon, “Topological surface states in nodal superconductors”, J. Phys.: Condens. Matter **27**, 243201 (2015).

[36] T. Kieu, E. Mascot, J. Bedow, R. Wiesendanger, and D. K. Morr, “Topological nodal point superconductivity in checkerboard magnet-superconductor hybrid systems”, Phys. Rev. B **108**, L060509 (2023).

[37] J. K. Dong, S. Y. Zhou, T. Y. Guan, H. Zhang, Y. F. Dai, X. Qiu, X. F. Wang, Y. He, X. H. Chen, and S. Y. Li, “Quantum Criticality and Nodal Superconductivity in the FeAs-Based Superconductor ${\mathrm{KFe}}_{2}{\mathrm{As}}_{2}$”, Phys. Rev. Lett. **104**, 087005 (2010).

[38] R.-X. Zhang, W. S. Cole, X. Wu, and S. Das Sarma, “Higher-Order Topology and Nodal Topological Superconductivity in Fe(Se,Te) Heterostructures”, Phys. Rev. Lett. **123**, 167001 (2019).

[39] A. K. Nayak, A. Steinbok, Y. Roet, J. Koo, G. Margalit, I. Feldman, A. Almoalem, A. Kanigel, G. A. Fiete, B. Yan, Y. Oreg, N. Avraham, and H. Beidenkopf, “Evidence of topological boundary modes with topological nodal-point superconductivity”, Nat. Phys. **17**, 1413–1419 (2021).

[40] I. Pletikosić, M. Kralj, P. Pervan, R. Brako, J. Coraux, A. T. N'Diaye, C. Busse, and T. Michely, "Dirac Cones and Minigaps for Graphene on Ir(111)", Phys. Rev. Lett. **102**, 056808 (2009).

[41] D. C. Elias, R. V. Gorbachev, A. S. Mayorov, S. V. Morozov, A. A. Zhukov, P. Blake, L. A. Ponomarenko, I. V. Grigorieva, K. S. Novoselov, F. Guinea, and A. K. Geim, "Dirac cones reshaped by interaction effects in suspended graphene", Nature Phys **7**, 701–704 (2011).

[42] A. A. Soluyanov, D. Gresch, Z. Wang, Q. Wu, M. Troyer, X. Dai, and B. A. Bernevig, "Type-II Weyl semimetals", Nature **527**, 495–498 (2015).

[43] B. Yan and C. Felser, "Topological Materials: Weyl Semimetals", Annual Review of Condensed Matter Physics **8**, 337–354 (2017).

[44] B. Q. Lv, H. M. Weng, B. B. Fu, X. P. Wang, H. Miao, J. Ma, P. Richard, X. C. Huang, L. X. Zhao, G. F. Chen, Z. Fang, X. Dai, T. Qian, and H. Ding, "Experimental Discovery of Weyl Semimetal TaAs", Phys. Rev. X **5**, 031013 (2015).

[45] H. Hopf, "Über die Abbildungen der dreidimensionalen Sphäre auf die Kugelfläche", Math. Ann. **104**, 637–665 (1931).

[46] A. I. Buzdin, "Proximity effects in superconductor-ferromagnet heterostructures", Rev. Mod. Phys. **77**, 935–976 (2005).

[47] G. R. Stewart, "Unconventional superconductivity", Advances in Physics **66**, 75–196 (2017).

[48] H. Wang, X. Li, G. Gao, Y. Li, and Y. Ma, "Hydrogen-rich superconductors at high pressures", WIREs Computational Molecular Science **8**, e1330 (2018).

[49] N. W. Ashcroft, "Metallic Hydrogen: A High-Temperature Superconductor?", Phys. Rev. Lett. **21**, 1748–1749 (1968).

[50] S. Nakosai, Y. Tanaka, and N. Nagaosa, "Two-dimensional p-wave superconducting states with magnetic moments on a conventional s-wave superconductor", Phys. Rev. B **88**, 180503 (2013).

[51] W. Meissner and B. Voigt, "Messungen mit Hilfe von flüssigem Helium XI Widerstand der reinen Metalle in tiefen Temperaturen", Annalen der Physik **399**, 892–936 (1930).

[52] W. J. de Haas, J. de Boer, and G. J. van dën Berg, "The electrical resistance of gold, copper and lead at low temperatures", Physica **1**, 1115–1124 (1934).

[53] J. Kondo, "Resistance Minimum in Dilute Magnetic Alloys", Progress of Theoretical Physics **32**, 37–49 (1964).

[54] J. Li, W.-D. Schneider, R. Berndt, and B. Delley, “Kondo Scattering Observed at a Single Magnetic Impurity”, Phys. Rev. Lett. **80**, 2893–2896 (1998).

[55] V. Madhavan, W. Chen, T. Jamneala, M. F. Crommie, and N. S. Wingreen, “Tunneling into a single magnetic atom: spectroscopic evidence of the kondo resonance”, Science **280**, 567–569 (1998).

[56] H. C. Manoharan, C. P. Lutz, and D. M. Eigler, “Quantum mirages formed by coherent projection of electronic structure”, Nature **403**, 512–515 (2000).

[57] N. Knorr, M. A. Schneider, L. Diekhöner, P. Wahl, and K. Kern, “Kondo Effect of Single Co Adatoms on Cu Surfaces”, Phys. Rev. Lett. **88**, 096804 (2002).

[58] M. A. Schneider, L. Vitali, N. Knorr, and K. Kern, “Observing the scattering phase shift of isolated Kondo impurities at surfaces”, Phys. Rev. B **65**, 121406 (2002).

[59] H. O. Frota and L. N. Oliveira, “Photoemission spectroscopy for the spin-degenerate Anderson model”, Phys. Rev. B **33**, 7871–7874 (1986).

[60] H. O. Frota, “Shape of the Kondo resonance”, Phys. Rev. B **45**, 1096–1099 (1992).

[61] Yu Luh, “BOUND STATE IN SUPERCONDUCTORS WITH PARAMAGNETIC IMPURITIES”, wlxb **21**, 75 (1965).

[62] A. I. Rusinov, “SUPERCONDUCTIVITY NEAR A PARAMAGNETIC IMPURITY.”, JETP Lett. (USSR) (Engl. Transl.), 9: 85-7(Jan. 20, 1969). (1969).

[63] S. Blundell, *Magnetism in condensed matter* (Oxford University Press, 2001).

[64] J. Hagemeister, *Monte Crystal Software*, https://github.com/JHagemeister/MonteCrystal.

[65] M. Getzlaff, *Fundamentals of Magnetism* (Springer-Verlag, Berlin Heidelberg, 2008).

[66] I. Dzyaloshinskii, “A thermodynamic theory of "Weak" ferromagnetism of antiferromagnetics”, Journal of Physics and Chemistry of Solids **4**, 241–255 (1958).

[67] T. Moriya, “Anisotropic superexchange interaction and weak ferromagnetism”, Phys. Rev. **120**, 91–98 (1960).

[68] R. Brüning, J. Bedow, R. L. Conte, K. von Bergmann, D. K. Morr, and R. Wiesendanger, *The Non-collinear Path to Topological Superconductivity*, (May 23, 2024) `http://arxiv.org/abs/2405.14673` (visited on 06/15/2024), prepublished.

[69] A. Kubetzka and R. Brüning, *Mathematica code for the calculation of the topological charge density* (2024).

[70] S. D. Yi, S. Onoda, N. Nagaosa, and J. H. Han, “Skyrmions and anomalous Hall effect in a Dzyaloshinskii-Moriya spiral magnet”, Phys. Rev. B **80**, 054416 (2009).

[71] B. Berg and M. Luscher, “Definition and Statistical Distributions of a Topological Number in the Lattice O(3) Sigma Model”, Nucl. Phys. B **190**, 412–424 (1981).

[72] T. H. R. Skyrme, “A unified field theory of mesons and baryons”, Nuclear Physics **31**, 556–569 (1962).

[73] T. H. R. Skyrme, “A non-linear theory of strong interactions”, Proceedings of the Royal Society of London. Series A. Mathematical and Physical Sciences **247**, 260–278 (1958).

[74] M. Hoffmann, B. Zimmermann, G. P. Müller, D. Schürhoff, N. S. Kiselev, C. Melcher, and S. Blügel, “Antiskyrmions stabilized at interfaces by anisotropic Dzyaloshinskii-Moriya interactions”, Nat Commun **8**, `10.1038/s41467-017-00313-0` (2017).

[75] A. N. Bogdanov and D. A. Yablonskii, “Thermodynamically stable "Vortices" in magnetically ordered crystals. The mixed state of magnets”, Soviet Physics Journal of Experimental and Theoretical Physics **95**, 178 (1989).

[76] A. Bogdanov and A. Hubert, “Thermodynamically stable magnetic vortex states in magnetic crystals”, Journal of Magnetism and Magnetic Materials **138**, 255–269 (1994).

[77] S. Heinze, K. von Bergmann, M. Menzel, J. Brede, A. Kubetzka, R. Wiesendanger, G. Bihlmayer, and S. Blügel, “Spontaneous atomic-scale magnetic skyrmion lattice in two dimensions”, Nature Phys. **7**, 713–718 (2011).

[78] R. Tomasello, E. Martinez, R. Zivieri, L. Torres, M. Carpentieri, and G. Finocchio, “A strategy for the design of skyrmion racetrack memories”, Sci Rep **4**, 6784 (2014).

[79] S. S. P. Parkin, M. Hayashi, and L. Thomas, “Magnetic Domain-Wall Racetrack Memory”, Science **320**, 190–194 (2008).

[80] R. Brüning, *Emergence of magnetic skyrmions in ultrathin films of manganese on clean W(001) at high magnetic fields* (University of Hamburg, Hamburg, 2021).

[81] T. Hänke, “A new variable-temperature scanning tunneling microscope and temperature-dependent spin-polarized scanning tunneling spectroscopy on the Cr(001) surface”, doctoralThesis (Staats- und Universitätsbibliothek Hamburg Carl von Ossietzky, 2005).

[82] O. Pietzsch, “Aufbau eines Rastertunnelmikroskops: für den Einsatz im Ultrahochvakuum, bei tiefen Temperaturen und in hohen Magnetfeldern” (Uinversity of Hamburg, 1997).

[83] A. Kubetzka, “Optimierung eines Rastertunnelmikroskops für die Durchführung spinpolarisierter Rastertunnelmikroskopie” (University of Hamburg, 1999).

[84] O. Pietzsch, A. Kubetzka, D. Haude, M. Bode, and R. Wiesendanger, “A low-temperature ultrahigh vacuum scanning tunneling microscope with a split-coil magnet and a rotary motion stepper motor for high spatial resolution studies of surface magnetism”, Review of Scientific Instruments **71**, 424–430 (2000).

[85] J. H. Perry, “The Joule-Thomson Effect for Helium”, J. Phys. Chem. **28**, 1108–1112 (1924).

[86] G. Binnig and H. Rohrer, “Scanning tunneling microscopy”, Helvetica Physica Acta **55**, 726 (1982).

[87] R. Wiesendanger, H.-J. Güntherodt, G. Güntherodt, R. J. Gambino, and R. Ruf, “Observation of vacuum tunneling of spin-polarized electrons with the scanning tunneling microscope”, Phys. Rev. Lett. **65**, 247–250 (1990).

[88] J. Tersoff and D. R. Hamann, “Theory and application for the scanning tunneling microscope”, Physical Review Letters **50**, 1998–2001 (1983).

[89] S. Heinze, “Simulation of spin-polarized scanning tunneling microscopy images of nanoscale non-collinear magnetic structures”, Appl. Phys. A **85**, 407–414 (2006).

[90] D. Wortmann, S. Heinze, Ph. Kurz, G. Bihlmayer, and S. Blügel, “Resolving complex atomic-scale spin structures by spin-polarized scanning tunneling microscopy”, Phys. Rev. Lett. **86**, 4132–4135 (2001).

[91] K. Palotás, “Prediction of the bias voltage dependent magnetic contrast in spin-polarized scanning tunneling microscopy”, Phys. Rev. B **87**, 024417 (2013).

[92] K. von Bergmann, M. Menzel, D. Serrate, Y. Yoshida, S. Schröder, P. Ferriani, A. Kubetzka, R. Wiesendanger, and S. Heinze, “Tunneling anisotropic magnetoresistance on the atomic scale”, Phys. Rev. B **86**, 134422 (2012).

[93] M. Hervé, B. Dupé, R. Lopes, M. Böttcher, M. D. Martins, T. Balashov, L. Gerhard, J. Sinova, and W. Wulfhekel, “Stabilizing spin spirals and isolated skyrmions at low magnetic field exploiting vanishing magnetic anisotropy”, Nat Commun **9**, 1015 (2018).

[94] C. Hanneken, F. Otte, A. Kubetzka, B. Dupé, N. Romming, K. von Bergmann, R. Wiesendanger, and S. Heinze, “Electrical detection of magnetic skyrmions by tunnelling non-collinear magnetoresistance”, Nature Nanotechnology **10**, 1039–1042 (2015).

[95] M. Perini, S. Meyer, A. Kubetzka, R. Wiesendanger, S. Heinze, and K. von Bergmann, “Electrical Detection of Domain Walls and Skyrmions in Co Films Using Noncollinear Magnetoresistance”, Phys. Rev. Lett. **123**, 237205 (2019).

[96] D. M. Crum, M. Bouhassoune, J. Bouaziz, B. Schweflinghaus, S. Blügel, and S. Lounis, “Perpendicular reading of single confined magnetic skyrmions”, Nat Commun **6**, 8541 (2015).

[97] S. Mühlbauer, B. Binz, F. Jonietz, C. Pfleiderer, A. Rosch, A. Neubauer, R. Georgii, and P. Boni, “Skyrmion lattice in a chiral magnet”, Science **323**, 915–919 (2009).

[98] S. Zhang, J. Wang, Q. Zheng, Q. Zhu, X. Liu, S. Chen, C. Jin, Q. Liu, C. Jia, and D. Xue, “Current-induced magnetic skyrmions oscillator”, New J. Phys. **17**, 023061 (2015).

[99] S. Luo, M. Song, X. Li, Y. Zhang, J. Hong, X. Yang, X. Zou, N. Xu, and L. You, “Reconfigurable Skyrmion Logic Gates”, Nano Lett. **18**, 1180–1184 (2018).

[100] M. Song, M. G. Park, S. Ko, S. K. Jang, M. Je, and K.-J. Kim, “Logic Device Based on Skyrmion Annihilation”, IEEE Transactions on Electron Devices **68**, 1939–1943 (2021).

[101] R. Brüning, A. Kubetzka, K. von Bergmann, E. Y. Vedmedenko, and R. Wiesendanger, “Nanoscale skyrmions on a square atomic lattice”, Phys. Rev. B **105**, L241401 (2022).

[102] P. Ferriani, K. von Bergmann, E. Y. Vedmedenko, S. Heinze, M. Bode, M. Heide, G. Bihlmayer, S. Blügel, and R. Wiesendanger, “Atomic-scale spin spiral with a unique rotational sense: Mn monolayer on W(001)”, Phys. Rev. Lett. **101**, 027201 (2008).

[103] A. K. Nandy, N. S. Kiselev, and S. Blugel, “Supplemental Material for ”Interlayer exchange coupling – a general scheme turning chiral magnets into magnetic multilayers carrying atomic-scale skyrmions”, Phys. Rev. Lett. **116**, 177202 (2016).

[104] A. K. Nandy, N. S. Kiselev, and S. Blügel, “Interlayer Exchange Coupling: A General Scheme Turning Chiral Magnets into Magnetic Multilayers Carrying Atomic-Scale Skyrmions”, Phys. Rev. Lett. **116**, 177202 (2016).

[105] X. Z. Yu, Y. Onose, N. Kanazawa, J. H. Park, J. H. Han, Y. Matsui, N. Nagaosa, and Y. Tokura, “Real-space observation of a two-dimensional skyrmion crystal”, Nature **465**, 901–904 (2010).

[106] S. D. Foulias, K. J. Rawlings, and B. J. Hopkins, “A reversible phase transition in carbon segregation to W(110)”, J. Phys. C: Solid State Phys. **14**, 5403 (1981).

[107] H. .-. Fink and G. Ehrlich, “Direct observation of overlayer structures on W(110)”, Surface Science **110**, L611–L614 (1981).

[108] S. Meyer, M. Schmitt, M. Vogt, M. Bode, and S. Heinze, “Dead magnetic layers at the interface: Moment quenching through hybridization and frustration”, Phys. Rev. Res. **2**, 012075 (2020).

[109] P. M. Weber, T. Drevelow, J. Qi, M. Bode, and S. Heinze, “Evidence for a conical spin spiral state in the Mn triple layer on W(001): Spin-polarized scanning tunneling microscopy and first-principles calculations”, Phys. Rev. B **108**, 134419 (2023).

[110] J. S. Kasper and B. W. Roberts, “Antiferromagnetic Structure of alpha-Manganese and a Magnetic Structure Study of beta-Manganese”, Phys. Rev. **101**, 537–544 (1956).

[111] M. Bode, M. Heide, K. von Bergmann, P. Ferriani, S. Heinze, G. Bihlmayer, A. Kubetzka, O. Pietzsch, S. Blügel, and R. Wiesendanger, “Chiral magnetic order at surfaces driven by inversion asymmetry”, Nature **447**, 190–193 (2007).

[112] A. Kubetzka, P. Ferriani, M. Bode, S. Heinze, G. Bihlmayer, K. Von Bergmann, O. Pietzsch, S. Blügel, and R. Wiesendanger, “Revealing Antiferromagnetic Order of the Fe Monolayer on W(001): Spin-Polarized Scanning Tunneling Microscopy and First-Principles Calculations”, Phys. Rev. Lett. **94**, 087204 (2005).

[113] A. Lita, D. Rosenberg, S. Nam, A. Miller, D. Balzar, L. Kaatz, and R. Schwall, “Tuning of tungsten thin film superconducting transition temperature for fabrication of photon number resolving detectors”, IEEE Transactions on Applied Superconductivity **15**, 3528–3531 (2005).

[114] P. Hohenberg and W. Kohn, “Inhomogeneous Electron Gas”, Phys. Rev. **136**, B864–B871 (1964).

[115] W. Kohn and L. J. Sham, “Self-Consistent Equations Including Exchange and Correlation Effects”, Phys. Rev. **140**, A1133–A1138 (1965).

[116] J. C. Slater and G. F. Koster, “Simplified LCAO Method for the Periodic Potential Problem”, Phys. Rev. **94**, 1498–1524 (1954).

[117] L. Rózsa, L. Udvardi, L. Szunyogh, and I. A. Szabó, “Magnetic phase diagram of an Fe monolayer on W(110) and Ta(110) surfaces based on ab initio calculations”, Phys. Rev. B **91**, 144424 (2015).

[118] T. Eelbo, V. I. Zdravkov, and R. Wiesendanger, “STM study of the preparation of clean Ta(110) and the subsequent growth of two-dimensional Fe islands”, Surface Science **653**, 113–117 (2016).

[119] A. Y. Cho and J. R. Arthur, “Molecular beam epitaxy”, Progress in Solid State Chemistry **10**, 157–191 (1975).

[120] J. J. Goedecke, L. Schneider, Y. Ma, K. T. That, D. Wang, J. Wiebe, and R. Wiesendanger, *Correlation of Magnetism and Disordered Shiba Bands in Fe Monolayer Islands on Nb(110)* (arXiv, May 5, 2022).

[121] A. Kubetzka, M. Bode, O. Pietzsch, and R. Wiesendanger, “Spin-Polarized Scanning Tunneling Microscopy with Antiferromagnetic Probe Tips”, Phys. Rev. Lett. **88**, 057201 (2002).

[122] P.-J. Hsu, A. Kubetzka, A. Finco, N. Romming, K. von Bergmann, and R. Wiesendanger, “Electric-field-driven switching of individual magnetic skyrmions”, Nature Nanotech **12**, 123–126 (2017).

[123] E. E. Huber Jr., D. O. Smith, and J. B. Goodenough, “Domain-Wall Structure in Permalloy Films”, Journal of Applied Physics **29**, 294–295 (1958).

[124] S. Middelhoek, “Domain Walls in Thin Ni–Fe Films”, Journal of Applied Physics **34**, 1054–1059 (1963).

[125] N. Wiese, S. Mcvitie, J. Chapman, A. Capella, and F. Otto, “On the scaling behaviour of cross-tie domain wall structures in patterned NiFe elements”, EPL (Europhysics Letters) **80**, `10.1209/0295-5075/80/57003` (2007).

[126] K. L. Metlov, “Simple analytical description for the cross-tie domain wall structure”, Applied Physics Letters **79**, 2609–2611 (2001).

[127] N. L. Schryer and L. R. Walker, “The motion of 180° domain walls in uniform dc magnetic fields”, Journal of Applied Physics **45**, 5406–5421 (1974).

[128] G. S. D. Beach, C. Nistor, C. Knutson, M. Tsoi, and J. L. Erskine, “Dynamics of field-driven domain-wall propagation in ferromagnetic nanowires”, Nature Mater **4**, 741–744 (2005).

[129] K. Olejník, T. Seifert, Z. Kašpar, V. Novák, P. Wadley, R. P. Campion, M. Baumgartner, P. Gambardella, P. Němec, J. Wunderlich, J. Sinova, P. Kužel, M. Müller, T. Kampfrath, and T. Jungwirth, “Terahertz electrical writing speed in an antiferromagnetic memory”, Science Advances **4**, eaar3566 (2018).

[130] G. C. Ménard, S. Guissart, C. Brun, R. T. Leriche, M. Trif, F. Debontridder, D. Demaille, D. Roditchev, P. Simon, and T. Cren, “Two-dimensional topological superconductivity in Pb/Co/Si(111)”, Nat Commun **8**, 2040 (2017).

[131] S. Kezilebieke, M. N. Huda, V. Vaňo, M. Aapro, S. C. Ganguli, O. J. Silveira, S. Głodzik, A. S. Foster, T. Ojanen, and P. Liljeroth, “Topological superconductivity in a van der Waals heterostructure”, Nature **588**, 424–428 (2020).

[132] R. Lo Conte, M. Bazarnik, K. Palotás, L. Rózsa, L. Szunyogh, A. Kubetzka, K. von Bergmann, and R. Wiesendanger, "Coexistence of antiferromagnetism and superconductivity in Mn/Nb(110)", Phys. Rev. B **105**, L100406 (2022).

[133] M. O. Soldini, F. Küster, G. Wagner, S. Das, A. Aldarawsheh, R. Thomale, S. Lounis, S. S. P. Parkin, P. Sessi, and T. Neupert, "Two-dimensional Shiba lattices as a possible platform for crystalline topological superconductivity", Nat. Phys. **19**, 1848–1854 (2023).

[134] P. Chatterjee, S. Banik, S. Bera, A. K. Ghosh, S. Pradhan, A. Saha, and A. K. Nandy, "Topological superconductivity by engineering noncollinear magnetism in magnet/superconductor heterostructures: A realistic prescription for the two-dimensional Kitaev model", Phys. Rev. B **109**, L121301 (2024).

[135] P. Chatterjee, A. K. Ghosh, A. K. Nandy, and A. Saha, "Second-order topological superconductor via noncollinear magnetic texture", Phys. Rev. B **109**, L041409 (2024).

[136] J. Bedow, E. Mascot, T. Posske, G. S. Uhrig, R. Wiesendanger, S. Rachel, and D. K. Morr, "Topological superconductivity induced by a triple-q magnetic structure", Phys. Rev. B **102**, 180504 (2020).

[137] E. Mascot, J. Bedow, M. Graham, S. Rachel, and D. K. Morr, "Topological superconductivity in skyrmion lattices", npj Quantum Mater. **6**, 1–6 (2021).

[138] D. Steffensen, M. H. Christensen, B. M. Andersen, and P. Kotetes, "Topological superconductivity induced by magnetic texture crystals", Phys. Rev. Res. **4**, 013225 (2022).

[139] P. Beck, "Tuning the Spin-Orbit Coupling and the Spin Dynamics of Atomic Chains on Superconductors", doctoralThesis (Staats- und Universitätsbibliothek Hamburg Carl von Ossietzky, 2022).

[140] A. F. Schäffer, P. Siegl, M. Stier, T. Posske, J. Berakdar, M. Thorwart, R. Wiesendanger, and E. Y. Vedmedenko, "Rotating edge-field driven processing of chiral spin textures in racetrack devices", Sci Rep **10**, 20400 (2020).

[141] A. Yu. Kitaev, "Fault-tolerant quantum computation by anyons", Annals of Physics **303**, 2–30 (2003).

[142] M. H. Freedman, "Quantum Computation and the Localization of Modular Functors", Found. Comput. Math. **1**, 183–204 (2001).

[143] J. Nakamura, S. Liang, G. C. Gardner, and M. J. Manfra, "Direct observation of anyonic braiding statistics", Nat. Phys. **16**, 931–936 (2020).

[144] S. D. Sarma, M. Freedman, and C. Nayak, “Majorana zero modes and topological quantum computation”, npj Quantum Inf **1**, 1–13 (2015).

Danksagung

Zum Abschluss meiner Arbeit möchte ich all denen danken, die mich in der Zeit meiner Doktorarbeit unterstützt und begleitet haben.

- Prof. Dr. Roland Wiesendanger danke ich dafür, dass ich die Möglichkeit bekommen habe, in der Gruppe R wissenschaftlich auf höchstem Niveau arbeiten zu können.
- Dr. Kirsten von Bergmann und Dr. André Kubetzka danke ich für die exzellente Betreuung während meiner Zeit im Lab 013. Insbesondere für die Unterstützung bei den unzähligen Präparationen, die für eine erfolgreiche Präparation des Probensystems notwendig waren. Ebenso bedanke ich mich für die zahlreichen Diskussionen und Vorschläge zur Verbesserung der Experimente und das Einbringen von neuen Blickweisen auf bestimmte Problemstellungen.
- Jonas Spethmann danke ich besonders für die herzliche Aufnahme in das Lab 013-Team und die unzähligen Gespräche und Diskussionen, ob nun über Physik oder andere Themen. Es hat immer sehr viel Spaß gemacht gemeinsam im Labor oder im Büro zu arbeiten.
- Roberto Lo Conte danke ich für eine inspirierende Zeit im Labor mit sehr vielen anregenden Gesprächen über Physik und das Leben, vor allem die gemeinsame Zeit in Mailand war ein absolutes Highlight.
- Außerdem bedanke ich mich bei der gesamten Gruppe R für die tolle Atmosphäre in der Arbeitsgruppe.
- Des Weiteren gilt mein Dank meiner Familie und meinen Freunden, die mich im Studium immer wieder auf eine andere Art und Weise unterstützt haben. Dafür, dass ihr mir immer Vertrauen entgegengebracht habt, auch wenn ich mit meinem Studium in für euch nicht so vertrauten Gebieten gelandet bin und meistens viele Fragezeichen im Raum standen, wenn ich erklärt habe, was ich eigentlich mache. Ohne eure Unterstützung wäre das Studium nicht möglich gewesen.

  Zuletzt gilt mein Dank meiner Verlobten Mona, die mich über die gesamte Promotionszeit begleitet hat und wohl am Besten nachvollziehen kann, wie es mir in dieser Zeit ergangen ist. Danke für deine Geduld, deine aufmunternden Worte und dein Verständnis besonders in den anstrengenden Wochen vor der Abgabe.

Eidesstattliche Erklärung

Hiermit versichere ich an Eides statt, die vorliegende Dissertationsschrift selbst verfasst und keine anderen als die angegebenen Hilfsmittel und Quellen benutzt zu haben.

Sofern im Zuge der Erstellung der vorliegenden Dissertationsschrift generative Künstliche Intelligenz (gKI) basierte elektronische Hilfsmittel verwendet wurden, versichere ich, dass meine eigene Leistung im Vordergrund stand und dass eine vollständige Dokumentation aller verwendeten Hilfsmittel gemäß der Guten wissenschaftlichen Praxis vorliegt. Ich trage die Verantwortung für eventuell durch die gKI generierte fehlerhafte oder verzerrte Inhalte, fehlerhafte Referenzen, Verstöße gegen das Datenschutz- und Urheberrecht oder Plagiate.

Hamburg, den 31.07.2024

Reiner Brüning